Università degli Studi di Milano - Bicocca
Facoltà di Scienze Matematiche, Fisiche e Naturali
Corso di dottorato di Ricerca in Fisica e Astronomia

XXIV Ciclo, A.A. 2008 – 2011

A Thesis submitted for the degree of
Dottore di Ricerca in Fisica

An experiment for the direct calorimetric measurement of the neutrino mass

Elena Ferri
Matricola 049087

Advisor
Dr. Angelo Nucciotti

School Coordinator
Prof. Giuseppe Chirico

To my father

Contents

Introduction

The oscillation experiments have clearly shown that neutrino are massive particle. Nowadays the experiments based on kinematic analysis of electrons emitted in nuclear β-decay are the most sensitive for a direct electron-neutrino mass determination. The method consists in searching for a tiny deformation caused by a non-zero neutrino mass to the spectrum of the charged particles emitted near the end point. A possible approach is the calorimetric one. In a calorimetric measurement the source is embedded in the detector and all the energy is measured, except for the one taken away by the neutrino. A drawback of this approach is that the full spectrum is acquired, while only the decays very close to the end-point are useful for measuring the neutrino mass. Therefore, the source activity has to be limited to avoid pile-up which would deform the shape of beta spectrum. As a consequence the statistics near the end-point is limited as well. This limitation may be then partially balanced by using isotopes with an end-point energy as low as possible. In this scenario an international collaboration has grown around the project of Microcalorimeter Arrays for a Rhenium Experiment (MARE) for a direct calorimetric measurement of the neutrino mass with sub-electronvolt sensitivity. Although the baseline of the MARE project consists in a large array of rhenium based thermal detectors, a different option for the isotope is also being considered. The two competing isotopes are ^{187}Re and ^{163}Ho. While the first beta decays, the latter decays via electron capture, and both have a Q value around 2.5 keV. The MARE project has a staged approach. The first phase of the project (MARE-1) is a collection of activities with the aim of sorting out both the best isotope and the most suited detector technology to be used for the final experiment. The goal of the last phase (MARE-2) is to achieve a sub-eV sensitivity on the neutrino mass. It will deploy several arrays of thermal microcalorimeters.

During my Ph.D I have focused only on the rhenium isotope, neglecting the holmium. In fact, in the case of rhenium I have estimated the statistical sensitivity of a neutrino mass experiment performed with thermal calorimeters. First, through an analytical approach, I have derived an algorithm to assess the statistical sensitivity for a given experimental configuration and then, for the same experimental configuration, I have estimated the sensitivity on neutrino mass via a Montecarlo method. The results of the analytic approach are then validated through the comparison with the Montecarlo results over a wide range

of experimental parameters. The investigation is carried out for both phases of the MARE experiment. For example, the Montecarlo approach has shown that a neutrino mass sensitivity of 0.1 eV at 90% CL could be expected in 10 years running 3x10^5 detectors, each with a mass of 10 mg ($\sim$ 10 Hz) and with energy and time resolutions of about 1 eV and 1 μs respectively. Instead, a sensitivity on neutrino mass of 3.4 eV at 90% CL could be achieved in 3 years using 288 detectors, each with a mass of 500 μg ($\sim$ 0.3 Hz) and with energy and time resolutions of about 30 eV and 300 μs respectively. The latter is the configuration of the Milano MARE-1 experiment, which is one of the MARE-1 activities.

Subsequently, I have exploited the Montecarlo approach to study the main sources of systematic uncertainties of the calorimetric experiments, as the shape of the beta spectrum and the Beta Environmental Fine Structure (BEFS), which is a modulation of the beta spectrum due to the atoms surrounding the decaying nuclei. The systematics uncertainties relating to the source (i.e. excited final states and the escape electron) have been also investigated. Finally, I have evaluated the capability of the MARE experiment to measure the mass of heavy neutrinos from some tens of eV to 2.5 keV.

I have also participated in the Milano MARE-1 experiment. This experiment is carried out in Milano by the group of Milano–Bicocca in collaboration with NASA/GSFC and Wisconsin groups. The Milano MARE-1 arrays are based on semiconductor thermistors, provided by the NASA/GSFC group, with dielectric silver perrhenate absorbers, $AgReO_4$. These arrays consist of 6 x 6 implanted Si:P thermistors on which single crystal of $AgReO_4$ are attached. The mass of a single absorber is around 500 μg, corresponding to a single detector rate of 0.3 Hz. The cryogenic set-up of MARE-1 is designed to host up to 8 arrays (i.e. 288 detectors), but the installation of only two arrays has been funded so far.

The read-out electronics of MARE-1 in Milano is characterized by a cold buffer stage, based on JFETs which work at about 120 K, followed by an amplifier stage at room temperature. To electrically connect the detector at 85 mK to the JFETs at 120 K two decoupling stages are needed. The two stages have also to guarantee the mechanical stability. The first stage separates the detectors from the JFETs box, while the second one decouples the cold electronics box from the JFETs.

In this context, the activities I have carried out were focused primarily on the assembly of the entire cryogenic set-up of MARE-1 in Milano and then on its analysis and improvement.

Firstly, I have performed several cool-downs devoted to test the detector performances and to determinate the best thermal coupling between Si thermistors and $AgReO_4$ absorbers, in conclusion of which we have obtained an energy resolution of around 30 eV at 2.6 keV and a rise time of about 300 μs. With 72 detectors and such performances, a sensitivity on neutrino mass of 4.7 eV at 90 % C.L. is expected in three years running time. During these cool-downs it was used the electronics of the MIBETA experiment, the predecessor of the MARE-1 experiment in Milano.

Since its first installation the cryogenic set-up of MARE-1 has presented several structural and thermal problems. The first has concerned the electrical connections between the detectors and electronics, while the latter the insufficient thermal decoupling between the JFETs support and the cold electronic box as well as the insufficient thermalization of the array ceramic board and of the array itself. As a consequence, no signal could be acquired. Therefore, I have performed an R&D work in order to solve all of these problems in conclusion of which the detectors have reached a base temperature such that it was possible to acquire a first spectrum with a threshold below 800 eV. In this condition, an energy resolution of 175 eV at 1.5 keV and of 181 eV at 5.9 keV have been obtained, while the rise time was about 850 μs. It was the first time that a spectrum with this threshold was acquired with the MARE-1 set-up. The worsening observed in the detectors performances with respect to the test runs was due to an excessive microphonics noise. Nevertheless it can be hypothesized that a 72 channels measurement will be starting soon.

Chapter 1

Neutrino Physics

In the last decades, the observation of flavour oscillations of solar and atmospheric neutrinos, as well as of reactor and accelerator neutrinos, have provided the evidence of a non-vanishing neutrino mass leading to a new physics beyond the Standard Model (SM). The difficulty in detecting and studying them explains why the neutrinos are the object of many experiments dedicated to determine their mass and nature. While the oscillation experiments are sensitive only to the differences in squared neutrino mass Δm^2_{ij}, the absolute mass scale of neutrinos can be investigated by: a) high precision measurements of beta decay kinematics, providing information on the effective electron neutrino mass m_β; b) searches for neutrinoless double beta decay (0νDBD), yielding results for the effective Majora neutrino mass $m_{\beta\beta}$; c) cosmological researches, allowing to deduce the sum of neutrino mass Σm_i. In addition, 0νDBD is the most sensitive method to answer the question concerning the neutrino nature (i.e. Dirac or Majorana particle).

In this chapter, after a short overview of oscillation results, direct measurements of neutrino masses are presented.

1.1 Neutrino in particle physics

In 1930 W. Pauli postulated the existence of a new particle, saving the concept of energy and momentum conservation in the light of a continuous beta spectrum. But, it was E. Fermi [1] in 1934 who named this particle neutrino, within the formulation of his theory for beta decay. In 1956 neutrinos were detected for the first time by F. Reines and C. Cowan [2, 3], observing the inverse beta decay produced by anti-neutrino interactions. In 1962 muon neutrinos were discovered by L.M. Lederman et al. at Brookhaven National Laboratories [5], while the first direct detection of the tau neutrino was obtained by the DONUT experiment in 2000 [6].

In the Standard Model of electroweak interaction, constructed in the Seventies, neutrinos are described as left-handed massless partners of the charged leptons. The invisible

width of the Z boson, caused by its decay into unobservable channels and measured at the $e^+ - e^-$ annihilation experiments, shows that there are just three active neutrinos [4]. New discoveries of the last decade, however, have proven that neutrinos are massive particles implying that the Standard Model description of elementary fermions is not complete and that physics beyond the SM exists. There are many unified theories, developed to overcome the shortcomings of this model, investigating the origin of the neutrino mass and mixing. The Grand Unified Theories (GUTs), which unify the strong and electroweak interactions, provide a natural framework for neutrino masses. In the context of GUTs it is possible to develop predictive models to give mass to neutrinos. The smallness of neutrino masses is explained by means of the see saw mechanism, which is often incorporated in GUTs. In this contest neutrino is a Majorana particle. Therefore, the experimental determinations of the neutrino mass scale, pattern and nature are crucial tests for predictive GUTs and for the improvement of our understanding of the basic theory of fundamental interactions.

Moreover, neutrinos and their properties play a fundamental role in astrophysics and cosmology. In fact, the understanding of Big-Bang Nucleosynthesis and the features of the Cosmic Microwave Background (CMB) illustrate the important role of neutrinos in the history of the early universe. But, the role of neutrino in shaping the universe and if the neutrinos allow to understand the matter-antimatter asymmetry of the universe via leptogenesis are still open questions. In any case, the answer to these questions requires the precise knowledge of the neutrino mass value.

1.2 Neutrino oscillations

In the case of a non-vanishing neutrino mass the weak ($|\nu_e\rangle$; $|\nu_\tau\rangle$; $|\nu_\mu\rangle$) and the mass ($|\nu_1\rangle$; $|\nu_2\rangle$; $|\nu_3\rangle$) eigenstates are not necessarily identical. This allows the phenomenon of neutrino oscillations, a kind of flavour oscillations which is already known in other particle systems (i.e. the quark sector). It can be described by a pure quantum mechanism. In the Lagrangian, neutrinos with a well defined flavour are a coherent superposition of mass eigenstates via a unitary mixing matrix $U_{\alpha i}$:

$$|\nu_\alpha\rangle = \sum_i U_{\alpha i} |\nu_i\rangle \tag{1.1}$$

and similarly for the mass eigenstates:

$$|\nu_i\rangle = \sum_\alpha (U^\dagger)_{i\alpha} |\nu_\alpha\rangle = \sum_\alpha U^*_{\alpha i} |\nu_\alpha\rangle \tag{1.2}$$

To understand neutrino flavour change, or oscillation, it is necessary to consider how a neutrino born as ν_α of equation (1.1) evolves in time. The mass eigenstates are stationary states and show a time dependence according:

$$|\nu_i(x;t)\rangle = e^{-iE_it}|\nu_i(x,0)\rangle = e^{-iE_it}e^{ipx}|\nu_i\rangle \tag{1.3}$$

assuming neutrinos with momentum p emitted by a source positioned at $x = 0$ ($t = 0$) and being relativistic $E_i = \sqrt{m_i^2 + p_i^2} \simeq E + m_i^2/(2E)$ for $p \ll m_i$ and $E \sim p$ as neutrino energy. Assuming that the difference in mass between two neutrino states with different mass $\Delta m_{ij}^2 = m_i^2 - m_j^2$ cannot be resolved, then the flavour neutrino is a coherent superposition of neutrino mass states with definite mass. Neutrinos are produced and detected as flavour states. Therefore, considering equations (1.1) and (1.2) neutrinos with flavour ν_α, emitted by a source at $t = 0$, develop with time into a state:

$$|\nu(x;t)\rangle = \sum_i U_{\alpha i}e^{-iE_it}|\nu_i\rangle = \sum_{i,\beta} U_{\alpha i}U_{\beta i}^* e^{-iE_it}e^{ipx}|\nu_\beta\rangle \tag{1.4}$$

the phase factor in (1.4) depends on m_i. This implies that the flavour content of the final state differs from the initial one. At a macroscopic distances this effect can be large in spite of small differences in neutrino masses. The time dependent transition amplitude for a flavour conversion $\nu_\alpha \to \nu_\beta$ is given by:

$$A(\alpha \to \beta)(t) = \langle \nu_\beta|\nu(x;t)\rangle = \sum_i U_{\beta i}^* U_{\alpha i} e^{-iE_it}e^{ipx} \tag{1.5}$$

which can be rewritten using the expression of the relativistic energy:

$$A(\alpha \to \beta)(t) = \sum_i U_{\beta i}^* U_{\alpha i} e^{-i\frac{m_i^2}{2}\frac{L}{E}} = A(\alpha \to \beta)(L) \tag{1.6}$$

where $L = x = ct$ is the distance between source and detector.

Then the transition probability P is the square of the transition amplitude A:

$$\begin{aligned} P(\alpha \to \beta)(t) &= |A(\alpha \to \beta)(t)|^2 \\ &= \sum_i |U_{\alpha i}U_{\beta i}^*|^2 \qquad (1.7) \\ &+ 2\sum_{i>j} \Re(U_{\alpha i}U_{\alpha j}^* U_{\beta i}^* U_{\beta j}) e^{(-i\frac{\Delta m_{ij}}{2}\frac{L}{E})} \qquad (1.8) \end{aligned}$$

with $\Delta m_{ij}^2 \equiv m_i^2 - m_j^2$. The second term in (1.8) describes the time/spatial dependent neutrino oscillation, while the first one is an average transition probability, which can be rewritten as:

$$\langle P_{\alpha\to\beta}\rangle = \sum_i |U_{\alpha i}U_{\beta i}^*|^2 = \sum_i |U_{\alpha i}^* U_{\beta i}|^2 = \langle P_{\alpha\to\beta}\rangle \tag{1.9}$$

Using the CP invariance, the transition probability P becomes:

$$
\begin{aligned}
P(\alpha \to \beta)(t) &= \delta_{\alpha\beta} \\
&- 4 \sum_{i>j=1}^{3} \Re(U_{\alpha i} U^*_{\alpha j} U^*_{\beta i} U_{\beta j}) sin^2(\Delta m^2_{ij} \frac{L}{4E}) \\
&+ 4 \sum_{i>j} \Im(U_{\alpha i} U^*_{\alpha j} U^*_{\beta i} U_{\beta j}) sin^2(\Delta m^2_{ij} \frac{L}{4E})
\end{aligned} \tag{1.10}
$$

Therefore, the probability of finding the original flavour is given by:

$$
P(\alpha \to \alpha) = 1 - \sum_{\alpha \neq \beta} P(\alpha \to \beta) \tag{1.11}
$$

As one can see from (1.8) there will be neutrino oscillations if at least one neutrino mass eigenstate is different from zero and if there is a mixing among the flavour (i.e. non diagonal terms in U). In addition, oscillations are only sensitivity to Δm^2 and not to absolute neutrino mass scale.

In a three neutrinos scenario the mixing matrix U, also known as Pontecorvo-Maki-Nakagawa-Sakata (PMNS) matrix, is parametrized by three angles, Θ_{12},Θ_{13} e Θ_{23}, by a CP-violating phase δ and by two Majorana phases, α_1 e α_2. The Majorna phases do not affect the probability of oscillations and have physical consequences only if the neutrinos are Majorana particles (neutrino does not differ from its antiparticle). Using the Chau and Keung [7] parametrization of the PMNS matrix, it becomes:

$$
\begin{pmatrix} \nu_e \\ \nu_\mu \\ \nu_\tau \end{pmatrix} = \begin{pmatrix} c_{12}c_{13} & s_{12}c_{13} & s_{13}e^{-i\delta} \\ -s_{12}c_{23} - c_{12}s_{23}s_{13}e^{i\delta} & c_{12}c_{23} - s_{12}s_{23}s_{13}e^{i\delta} & s_{23}c_{13} \\ s_{12}s_{23} - c_{12}c_{23}s_{13}e^{i\delta} & -c_{12}s_{23} - s_{12}c_{23}s_{13}e^{i\delta} & c_{23}c_{13} \end{pmatrix} \begin{pmatrix} e^{i\alpha_1/2}\nu_1 \\ e^{i\alpha_2/2}\nu_2 \\ \nu_3 \end{pmatrix}
$$

where $c_{ij} = \cos\Theta_{ij}$ and $s_{ij} = \sin\Theta_{ij}$. The three masses m_i have to be added to the parameters set which describes the mixing matrix, giving therefore nine unknown parameters altogether.

In the case of three neutrinos mixing there are only two independent neutrino mass squared differences Δm^2_{21} and Δm^2_{31}. It is convenient for relating the mixing angles Θ_{12}, Θ_{23} and Θ_{13} to observables, to identify the $|\Delta m^2_{21}|$ with the smaller of the two neutrino mass squared differences, which, as it follows from experimental data, is responsible for the solar $\bar{\nu_e}$ and reactor ν_e oscillations. Just for convenience, the massive neutrino will be numbered in such a way that $m_2 > m_1$, so that $\Delta m^2_{21} > 0$. With this choice there are two possibilities: either $m_1 < m_2 < m_3$ or $m_3 < m_2 < m_1$. Then the larger neutrino mass squared difference $|\Delta m^2_{31}|$ or $|\Delta m^2_{32}|$ can be associated with the experimentally observed oscillations of the atmospheric $\bar{\nu_\mu}$ and ν_μ and of accelerator ν_μ. The angles Θ_{12} and Θ_{23} are often called "solar" and "atmospheric" neutrino mixing angles, and are often denoted as

$\Theta_{12} = \Theta_{sol}$ and $\Theta_{23} = \Theta_{atm}$, while Δm^2_{21} and Δm^2_{31} are often referred to as the "solar" and "atmospheric" neutrino mass squared differences and are often denoted as $\Delta m^2_{21} = \Delta m^2_{sol}$ and $\Delta m^2_{31} = \Delta m^2_{atm}$.

The most recent values of the oscillation parameters are given in table 1.1. They were obtained not only by considering atmospheric (SuperKamiokande and MACRO) and solar (SuperKamiokande, SNO and GALLEX/GNO) experiments but also the reactors (KamLAND and CHOOZ) and accelerators (K2K and NUMI) experiments.

Oscillation parameters	**Central value**	**99% CL range**
Solar mass splitting	$\Delta m^2_{12} = (7.58 \pm 0.21)10^{-5}\text{eV}^2$	$(7.1 \div 8.1)10^{-5}\text{eV}^2$
Atmospheric mass splitting	$\lvert\Delta m^2_{23}\rvert = (2.40 \pm 0.15)10^{-3}\text{eV}^2$	$(2.1 \div 2.8)10^{-3}\text{eV}^2$
Solar mixing angle	$\tan^2\Theta_{12} = (0.484 \pm 0.048)$	$31^\circ < \Theta_{12} < 39^\circ$
Atmospheric mixing angle	$\sin^2 2\Theta_{23} = (1.02 \pm 0.04)$	$37^\circ < \Theta_{23} < 53^\circ$
"CHOOZ" mixing angle	$\sin^2 2\Theta_{13} = (0.07 \pm 0.04)$	$0^\circ < \Theta_{13} < 13^\circ$

Table 1.1: Summary of current information on neutrino masses and mixing parameters from oscillations data [8].

The existing data do not allow one to determine the sign of Δm^2_{atm}. In the case of three neutrino mixing, the two possible signs of Δm^2_{atm} correspond to two types of neutrino mass spectrum. If that sign is positive, the neutrino mass pattern is called a normal mass ordering ($m_1 < m_2 < m_3$) and when it is negative it is called inverted mass ordering ($m_3 < m_2 < m_1$). The extreme mass orderings, $m_1 \ll m_2 < m_3$ and $m_3 \ll m_2 < m_1$, are called the normal and, respectively, inverted hierarchies. When $m_1 \sim m_2 \sim m_3$, one speaks of degenerate pattern. Figure 1.1 shows the three possible scenarios for the hierarchy of the masses.

In addition, the phase δ governing CP violation in the flavour oscillation experiments remains unknown, and a topic of considerable interest. The remaining unknown quantities, i.e. the absolute neutrino mass scale and the two Majorana phases α_1 , α_2 , are not accessible in oscillation experiments. Their determination is the ultimate goal of neutrinoless double beta decay experiments and beta decay experiments.

1.3 Non oscillation experiments

Oscillation experiments are insensitive to the absolute neutrino mass scale, parametrized by the mass of the lightest neutrino, and to the two Majorana phases. Other experiments are powerful tools to asses the neutrino mass pattern and to give information about the neutrino nature (i.e. to establish whether the neutrino is a Majorana or a Dirac particle). They are single and double beta decay experiments and the cosmological observations.

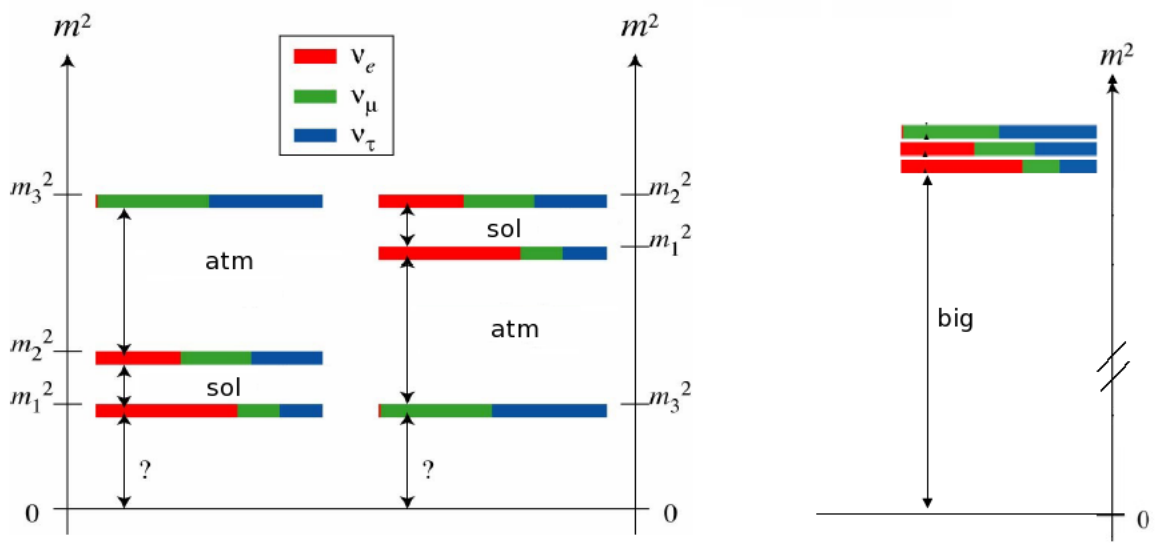

Figure 1.1: Possible configurations for the neutrino mass with the assumption $\Delta m^2_{12} \ll \Delta m^2_{23}$. Colors represent flavor abundances in mass eigenstates.

1.3.1 Cosmological researches

Neutrinos, like any other particle, contribute to the total energy density of the Universe. Light neutrinos are relativistic trough most of the evolution of the Universe and, as consequence, they play an important role in the formation of large scale structures leaving a clear signature in many cosmological observables. The main effect of neutrinos in cosmology is to suppress the growth of fluctuations on scales below the horizon when they become non-relativistic. Because of this suppression it is possible to infer constraints, although indirectly, on the neutrino masses by comparing the most recent cosmological data with the current theoretical predictions. The neutrino energy density $\Omega_\nu h^2$ is related to the total neutrino mass though:

$$\Omega_\nu h^2 = \Sigma_i m_i / (94 eV^2) \tag{1.12}$$

where h is the Hubble constant normalized to $H_0 = 100$ km s^1 Mpc^1 and $\Sigma_i m_i$ given by:

$$\Sigma_i m_i = m_1 + m_2 + m_3 \tag{1.13}$$

Therefore, cosmology is sensitive to the total neutrino mass $\Sigma_i m_i$ but it is blind to neutrino mixing angles or possible CP-violating phases.

A single cosmological bound on neutrino masses does not exist. Depending on the included set of data, limits on neutrino masses range from few eV to few hundreds of meV.

The current WMAP 7-year dataset obtains an upper bound on the sum of neutrino masses of 1.3 eV at 95% CL. [10] within the standard cosmological model, ΛCDM. Planck data alone will constrain $\Sigma_i m_i$ to 0.6 eV at 95% CL. [11]. This constraint should be considered as the most conservative and reliable cosmological constraint on neutrino masses. A tighter bound on the neutrino masses can be obtained by combining CMB observations with measurements of the Hubble constant H_0 and cosmic distances such as from Type Ia supernovae and Baryon Acoustic Oscillations (BAO). The WMAP7+BAO+H_0 analysis of [10] reports a constraint of 0.58 eV at 95% C.L., while a constraint about a factor 2 smaller could be achieved when the Planck data will be combined with similar datasets.

Current cosmological data probe the region of neutrino masses where the three neutrino states are degenerate.

In conclusion, the cosmological observations can lead to results complementary to laboratory experiments, such as single beta decay and neutrinoless double beta decay.

1.3.2 Double beta decay

The two-neutrino double beta decay mode (2νDBD) was first proposed in 1935 by Goeppert-Mayer [9]. It is expected to occur in the Standard Model as a second order effect of the well known beta decay, and it imposes no special requirements on neutrino properties. This process can be energetically favoured for some even-even nuclei belonging to A even multiplets. The first direct observation of the 2νDBD was in 1987 [12] and is now observed in more than ten nuclei [13, 14].

More interesting from a Particle Physics standpoint is neutrinoless double deta decay (0νDBD), proposed by Furry [15] in 1939. The neutrinoless double beta decay given by:

$$(A + Z) \rightarrow (A, Z + 2) + 2e^- \tag{1.14}$$

breaks lepton number conservation and it is therefore forbidden by the Standard Model. This process can occur only if the neutrino is a massive Majorana particle (i.e. $\nu = \bar{\nu}$) and it is the only known probe to test whether the neutrino is a Majorana or Dirac particle. The lifetime for the neutrinoless double beta decay is expected to be longer than 10^{25} y and only one evidence has been reported for ^{76}Ge so far [16].
0νDBD researches measure the process half-life $\tau^{0\nu}_{1/2}$ which is related to neutrino masses trough:

$$\tau^{0\nu\ -1}_{1/2} = \frac{|m_{\beta\beta}|^2}{m_e^2} G^{0\nu} |M^{0\nu}|^2 \tag{1.15}$$

where m_e is the electron mass, $G^{0\nu}$ is the space phase factor, $M^{0\nu}$ is the matrix element and $m_{\beta\beta}$ the effective Majorana mass, the most relevant parameter given explicitly by a coherent sum over the contributions of the different ν_i to the electron flavour:

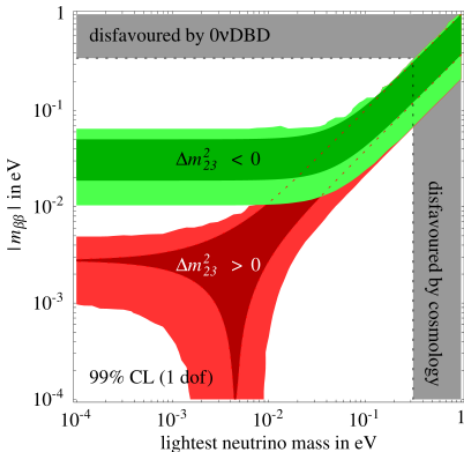

Figure 1.2: 99% C.L. expected ranges for the parameter $|m_{\beta\beta}|$ as a function of lightest neutrino mass. $\Delta m^2_{23} > 0$ corresponds to Normal Hierarchy ($m_{lightest} = m_1$), while $\Delta m^2_3 < 0$ corresponds to Inverted Hierarchy ($m_{lightest} = m_3$). The darker regions show how the ranges would shrink if the present best-fit values of oscillation parameters were confirmed with negligible errors. Picture from [8].

$$m_{\beta\beta} \equiv |\sum_i U_{ei}^2 m_i| = |\sum_i |U_{ei}|^2 e^{i\alpha_i} m_i| \tag{1.16}$$

where U_{ei} are the PMNS matrix element and α_i the two Majorana phases. Since the U_{ei} and the two squared mass differences are known from oscillation experiments, $m_{\beta\beta}$ can be written in terms of only three unknown parameters, the mass of the lightest neutrino and the two Majorana CP phases. The result is shown in figure 1.2, where the allowed values for $m_{\beta\beta}$ are plotted as a function of the lightest neutrino mass.

To obtain $m_{\beta\beta}$ from the experimentally observable $\tau^{0\nu}_{1/2}$ the product $F_N = G^{0\nu}|M^{0\nu}|^2$, referred to as nuclear factor of merit, must be known. While $G^{0\nu}$ can be precisely calculated, the nuclear matrix $|M^{0\nu}|$ contains the uncertain details of the nuclear part of the process and it is strongly dependent on the nuclear model used for its evaluation. In fact there is a large spread in the nuclear matrix elements calculated by different authors with different nuclear models [17, 18, 19, 20, 21].

From an experimental point of view, searching for 0νDBD consists in the detecting the two electrons emitted in the process. Since the energy of the recoiling nucleus is negligible, the sum of the kinetic energy of the two electrons is equal to the Q-value of the transition. So the signature for 0νDBD is a peak at the transition energy $Q_{\beta\beta}$.

Current experimental limits are reported in table 1.2

$m_{\beta\beta}$ in eV	% CL	Isotopes	Experiments
< 0.42 - 0.66	90	^{76} Ge	Heildeberg-Moscow [22]
< 0.33 - 1.35	90	^{76} Ge	IGEX [23]
< 0.89 - 2.4	90	^{82} Se	NEMO-3 [24]
< 0.45 - 0.93	90	^{100} Mo	NEMO-3 [24]
< 0.30 - 0.71	90	^{130} Te	CUORICINO [25]
< 1.1 - 2.7	90	^{136} Xe	DAMA [26]

Table 1.2: Summary of current results concerning the research of neutrinoless double beta decay.

1.3.3 Single beta decay

Direct neutrino mass measurements are performed by analyzing the kinematics of charged particles emitted together with flavour state neutrinos in suitable weak decays. To date the most sensitive neutrino mass measurement, involving electron type neutrinos, is based on studying the shape of the beta spectrum. Single beta decay experiments are sensitive to an incoherent combination of the mass eigenvalues, called effective electron neutrino mass m_β and defined as:

$$m_{\nu_e} = \sqrt{\sum_{i=1}^{3} |U_{ei}|^2 m_i^2} \tag{1.17}$$

where the sum is over all mass eigenvalues m_i which are too close together to be resolved experimentally. The weights $|U_{ei}|^2$, well known from neutrino oscillations, are the probabilities of generating the three mass eigenstates m_i in beta decay. In contrast to $m_{\beta\beta}$, m_β is not sensitive to the two Majorana phases.

A limit on m_{ν_e} implies an upper limit on the lightest mass eigenstate m_{min}, independent on the mixing parameters $|U_{ei}|^2$: $m_{min} \leq m_{\nu_e}$, i.e. the lightest neutrino can not be heavier than m_{ν_e}. If experiments on neutrino oscillations provide the values of all neutrino mass-squared differences Δm_{ij}^2 (including their signs) and the mixing parameters $|U_{ei}|^2$ then, determined the value of m_{ν_e}, the neutrino mass squared difference can be determined:

$$m_j^2 = m_{\nu_e}^2 - \sum_{i=1}^{3} |U_{ei}|^2 \Delta m_{ij}^2 \tag{1.18}$$

where $\Delta m_{ij} = m_i^2 - m_j^2$.

On the other hand, if only the absolute values $|\Delta m_{ij}^2|$ are known, a limit on m_{ν_e} from beta decay could be used to define an upper limit on the maximum value m_{max} of m_{ν_i}:

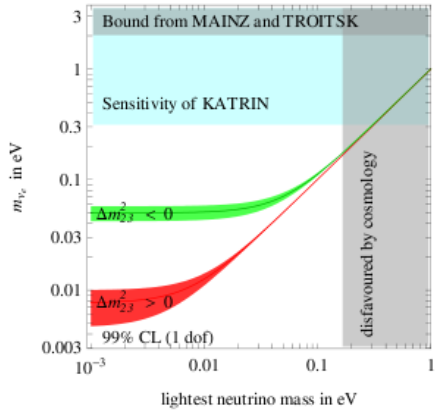

Figure 1.3: 99% C.L. expected ranges for the parameter m_β as a function of lightest neutrino mass. $\Delta m^2_{23} > 0$ corresponds to Normal Hierarchy ($m_{lightest} = m_1$), while $\Delta m^2_3 < 0$ corresponds to Inverted Hierarchy ($m_{lightest} = m_3$). The darker regions show how the ranges would shrink if the present best-fit values of oscillation parameters were confirmed with negligible errors. The constraints coming from the Troitsk and Mainz experiments are displayed together with the sensitivity of the future spectrometer experiment, KATRIN. Picture from [8].

$$m^2_{max} \leq m^2_{\nu_e} + \sum_{i<j} |\Delta m^2_{ij}| \tag{1.19}$$

In table 1.3 the results coming from calorimetric and spectrometric experiments are presented, while in figure 1.3 the allowed values for m_β are plotted as a function of the lightest neutrino mass.

$\mathbf{m_\beta}$ **in eV**	**CL %**	**Isotope**	**Experiment**
< 15	90	^{187} Re	Mibeta [27]
< 2.05	95	^{3} H	Troitsk [28]
< 2.3	95	^{3} H	Mainz [29]

Table 1.3: Results of single beta decay experiment, the first one is a calorimetric experiment while the other two are spectrometric experiments.

1.4 The direct neutrino mass measurement

Direct neutrino mass experiments are based on the kinematic analysis of electrons emitted in single β-decay. Relying only on energy-momentum conservation in β-decay, they are the only model-independent method to measure the neutrino mass scale with a sub-eV sensitivity. These experiments look for a tiny deformation of the beta spectrum close to

the end-point energy E_0 due to a non-zero neutrino mass. The most stringent limits are 2.1 eV at 95% CL. for electrostatic spectrometer and 15 eV at 90% CL. for calorimeters, the two most powerful methods that will be discussed extensively in sections 1.4.1 and 1.4.3.

The beta decay is a nuclear transition involving two nuclides $(A, Z-1)$ and (A, Z) according to:

$$(A, Z-1) \rightarrow (A, Z) + e^{-} + \bar{\nu}_e \tag{1.20}$$

From equation (1.20) one can see that the measured mass is the one of antineutrino $\bar{\nu_e}$. Since the CPT theorem assures that particle and antiparticle have the same rest mass, from now on it is possible to speak simply of "neutrino mass" both for ν_e and $\bar{\nu_e}$. The energy releases in this process is [1]:

$$Q = M(A, Z-1)c^2 - M(A, Z)c^2 \tag{1.21}$$

where M is the atomic mass of the atoms in the initial and final states (i.e. neutral mother and daughter). Single beta decays can be classified according to the rules reported in table 1.4

L=0,1	$\pi_f \pi_i = +1$	Allowed transitions
L=0,1	$\pi_f \pi_i = -1$	Non unique first forbidden transitions
L>0,1	$\pi_f \pi_i = (-1)^L$	Non unique L-th forbidden transitions
	$\pi_f \pi_i = (-1)^{L-1}$	Unique (L-1)-th forbidden transitions

Table 1.4: Classification and terminology of single beta decays. $L = \Delta J = |J_f - J_i|$, where J_f, J_i, π_f and π_i are respectively the spins and the parities of the initial and final nuclides.

Neglecting the nucleus recoil and defining the maximum electron energy E_0 in the case of a zero neutrino mass, the energy spectrum of the emitted electrons is described in the most general form by:

$$N_\beta = p_\beta(E_\beta + m_e c^2)(E_0 - E_\beta)\sqrt{(E_0 - E_\beta)^2 - m_{\nu_e}^2 c^4}F(Z, E_\beta)S(E_\beta)[1 + \delta_R(Z, E_\beta] \tag{1.22}$$

where, by indicating with p_β and E_β the momentum and the energy of the emitted electron respectively, the following terms appear:

- $p_\beta(E_\beta + m_e c^2)(E_0 - E_\beta)\sqrt{(E_0 - E_\beta)^2 - m_{\nu_e}^2 c^4}$ is the phase-space term in three body decay, for which the nuclear recoil is neglected.

[1] approximating the neutrino mass to zero

- $F(Z, E_\beta)$ is the term called Coulombian correction (or Fermi function) which accounts for the effect of the nuclear charge on the wave function of the emitted electron. In a model dealing with the relativistic effects and the finite size of the nucleus, this term appears as:

$$F(Z, E_\beta) = 4\left(\frac{2p_e R}{\hbar}\right)^{2\gamma-2} \exp(\pi\eta)\frac{|\Gamma(\gamma + i\eta)|^2}{|\Gamma(2\gamma+1)|^2} \approx \frac{2\pi\eta}{\exp(-2\pi\eta)} \tag{1.23}$$

  where $\eta = \alpha Z E_\beta 7 p_e$, $\gamma = (1 - (\alpha Z)^2)^{1/2}$, R is the nuclear ratio ($R = 1.2A^{1/3} fm$) and α is the fine structure constant. The formula (1.23) can be derived from the solution of the Dirac equation with point-like nucleus, computed at a distance R from the nucleus. In equation (1.23) the shielding effect of the $Z - 1$ electrons of the initial atom is neglected. Considering this shielding effect it means replacing the energy E_β of the emitted electron with the term $E'_\beta = E_\beta - \langle V_\beta \rangle$, where $\langle V_\beta \rangle$ is the average potential experimented by the electron at the nuclear surface due to the atomic electrons. In this way, the equation (1.23) becomes:

$$F(Z, E_\beta)' = F(Z, E_\beta - \langle V_\beta \rangle)\frac{E_\beta - \langle V_\beta \rangle}{E_\beta} \tag{1.24}$$

  In the Thomas-Fermi atomic model: $\langle V_\beta \rangle = 1.45 m_e \alpha^2 Z^{4/3}$.

- $S(E_\beta)$ is the form factor beta spectrum which takes into account the nuclear matrix element of the electroweak interaction $M(\mathcal{E}_\beta)$. It can be written as:

$$S(E_\beta) = G_F^2\left(\frac{m_e^5 c^4}{2\pi^3\hbar^7}\right) cos^2\Theta_c |M(\mathcal{E}_\beta)|^\epsilon \tag{1.25}$$

  where G_F is the Fermi factor and Θ_c the Cabibbo angle. The matrix element can be calculated by describing the interaction with an Hamiltonian including the V-A term.

- δ_R is the radiative electromagnetic correction, which is usually neglected due to its exiguity.

The experimental beta spectra are normally analysed by means of a transformation which produces a quantity generally linear with the energy E_β of the emitted electron:

$$K(E_\beta) \equiv \sqrt{\frac{N_\beta(Z, E_\beta, m_{\nu_e})}{p_\beta E_\beta F(Z, E_\beta) S(E_\beta)[1 + \delta_R(Z, E_\beta]}} = (E_0 - E_\beta)\left(1 - \frac{m_{\nu_e}^2 c^4}{(E_0 - E_\beta)^2}\right)^{1/4} \tag{1.26}$$

The graphic of $K(E_\beta)$ as a function of E_β is known as "Kurie Plot". Assuming a zero neutrino mass and an infinite energy resolution, the Kurie Plot is a straight line intersecting the X-axis at the transition energy E_0. Instead, in the case of non-vanishing neutrino mass, the Kurie Plot is distorted and it intersects the abscissa axis at an energy equal to $E_0 - m_\nu$. Figure 1.4 displays the two different cases.

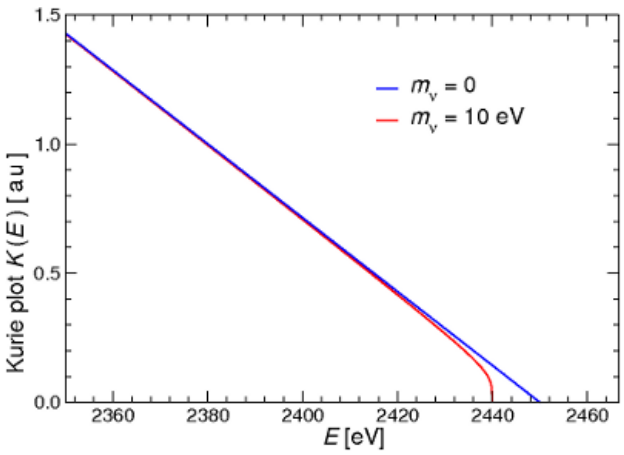

Figure 1.4: ^{187}Re *Kurie plot* close to the end-point, computed for a neutrino mass equal to zero (in blue) and 10 eV (in red).

As seen from plotted spectra for neutrino masses of 0 eV and 10 eV in figure 1.4, the sensitivity on neutrino mass is highest in the region close to the end-point. Unluckly, this is the region where the counting rate is lower. In particular, the relevant energy interval is $\Delta E \approx 3m_{\nu_e}$ and the fraction of events occurring is:

$$F_{\Delta E}(0) = \int_{E_0-\Delta E}^{E_0} N_\beta(Z, E_\beta, m_{\nu_e} = 0)dE \approx 2A_\beta \left(\frac{\Delta E}{E_0}\right)^3 \tag{1.27}$$

Other factors complicate the extraction of the neutrino mass from the final part of the beta spectrum. First of all, no real detector is characterized by an infinite energy resolution. A finite energy resolution distorts the shape of the beta spectrum near the end-point in an opposite way with respect to the neutrino mass effect. Therefore, it is mandatory to evaluate and/or measure the detector response function, which includes the detector energy resolution. Secondly, the atom or the molecule containing the decaying nucleus can be left in an excited state, leading even in this case to dangerous distortions of the beta spectrum. Due to the excited final states, the measured beta spectrum is a

combination of different spectra characterized by different transition energies $(E_0 - V_i)$, where V_i is the energy of the i-th excited state:

$$N_\beta(Z, E_\beta, m_{\nu_e}) \approx \sum_i w_i p_\beta E_\beta (E_0 - E_\beta - V_i)^2 \left(1 - \frac{m_{\nu_e}^2 c^4}{(E_0 - E_\beta - V_i)^2}\right) F(Z, E_\beta) S(E_\beta) \tag{1.28}$$

where w_i is the transition probability to the i-th final level. The existence of excited final states is particularly misleading in determining the neutrino mass. Assuming a vanishing neutrino mass and summing over all final states

$$N_\beta(Z, E_\beta, 0) \approx p_\beta E_\beta (E_0 - E_\beta - \langle V_i \rangle)^2 \left(1 + \frac{\langle V_i^2 \rangle - \langle V_i \rangle^2}{(E_0 - E_\beta - \langle V_i \rangle)^2}\right) F(Z, E_\beta) S(E_\beta) \tag{1.29}$$

which approximates the beta spectrum with a neutrino squared mass equal to $-\sigma^2 < 0$, with $\sigma^2 = \langle V_i^2 \rangle - \langle V_i \rangle^2$.

Last but not least, the background due to environmental radioactivity and cosmic rays could complicate the analysis of the beta spectrum. Because of the low beta counting rate in the interesting region, spurious background counts may affect the neutrino mass determination. It is possible to show that an uncertainty δB in the radioactive background evaluation modifies the spectrum according to:

$$N_\beta = p_\beta E_\beta (E_0 - E_\beta)^2 \left(1 + \frac{\delta B}{p_\beta E_\beta (E_0 - E_\beta) F(Z, E_\beta) S(E_\beta)}\right) F(Z, E_\beta) S(E_\beta) \tag{1.30}$$

simulating a neutrino with a negative squared mass $-2\delta B/(p_\beta E_\beta F S)$. The background rate B, and equivalently the uncertainty δB is expressed as counts per time and energy unity.

According to equation (1.27), an high sensitivity direct ν-mass experiment requires a β-emitting isotope characterized by a low E_0 to maximise the number N of decay events close to the end-point (see equation (1.27)). To date the two isotopes meeting this demand are ^{3}H and ^{187}Re. Tritium beta decay

$$^3H \rightarrow ^3He + e^- + \bar{\nu_e} \tag{1.31}$$

is a super-allowed transition with a low end-point energy $E_0 = 18.6$ keV and with a rather short half-life of 12.3 y. The very high intrinsic decay rate of ^{3}H allows to use thin sources. Finally, tritium is the only beta emitter which allows a specific activity large enough for an experimental set-up with a beta source and a separated high resolution electrostatic spectrometer. In addition, the type of transition poses no problem for the

analytical determination of the electron energy spectrum (i.e. the nuclear matrix element has not any energy dependence on the energy of the beta electron). Finally, tritium is characterized by a simple configuration of the electron shell, so that final state effects can be calculated precisely.

The ^{187}Re beta decay

$$^{187}Re(5/2^{+}) \rightarrow ^{187}\,Os(1/2^{-}) + e^{-} + \bar{\nu_e} \tag{1.32}$$

is a unique first forbidden transition, as can be deduced from table 1.4. Unlike non-unique transitions, the nuclear matrix element is computable, even if the calculation is not straightforward as in the case of tritium. In literature, it is possible to find detailed calculations both of the matrix element and of the Fermi function for this process. The main advantage of ^{187}Re is its very low end-point energy (E_0 =2.47 keV), one of the lowest known in nature. The ^{187}Re half-life is 42.3×10^9 y. These values were determined with bolometric experiments and they are reported in [27]. The large isotopic abundance (62.8%) of ^{187}Re in natural rhenium allows to get useful source without any isotopic separation process. The beta decay rate in natural rhenium is of the order of 1 Bq/mg, almost ideally suited to bolometric detection. Thanks to the much lower transition energy, the useful fraction of events close to the end-point is $\sim$ 350 times higher in rhenium than in tritium.

1.4.1 The electrostatic spectrometers

Since half a century, many tritium beta decay experiments have been performed using magnetic or electrostatic spectrometers. The firsts select electrons with given energy by means of the bending effect of a proper magnetic field, obtaining the most sensitive results until the Nineties. Over the past decades, the electrostatic spectrometers with adiabatic magnetic collimation have taken the place of magnetic spectrometers. In these devices, the electrons are collimated by means of a magnetic field with a characteristic space profile and selected by an electrostatic potential barrier. Higher energy resolutions and luminosities can be achieved with respect to magnetic spectrometers. The history of the results obtained with this techniques is reported in table 1.4.1.

The two main advantages, which make spectrometers the most sensitive devices in this field at the moment, are:

- Only the useful fraction of electrons with energies very close to the transition energy can be selected. Therefore, a very high statistics can be accumulated in the interesting interval.
- A very high energy resolution can be achieved (of the order of 1 eV for next generation experiment).

Experiments	Type	Source	m_ν in eV
ITEP [30]	M	Valine	35
INS [31]	M	$C_{20}H_{40}O_2$	<13
Zurich [32]	M	OTS	<11
LANL [33]	M	T_2 (gas)	<9.3
LNLN [34]	M	T_2 (gas)	<7
Troitsk [28]	E	T_2 (gas)	< 2.05
Mainz [29]	E	T_2 (solid)	< 2.3

Table 1.5: Summary of the most stringent results coming from spectrometers. In the second column M indicates magnetic spectrometers and E electrostatic ones.

In conclusion, spectrometers allow to focus on a very narrow energy range below E_0, which can be investigated with a very sharp energy resolution.

The major disadvantage of spectrometers is the fact that the radioactive source is external at the detector. As a consequence, the response function is a convolution of the exact transmission function of the spectrometer T [35] with four correction functions for energy loss, source charging, backscattering from the substrate present when the source is deposited on a solid substrate and energy dependence of detection efficiency.

$$T' = T \otimes f_{loss} \otimes f_{charge} \otimes f_{back} \otimes f_{det} \tag{1.33}$$

Each carries its particular systematic uncertainty, but f_{loss} is the dominant correction. Therefore, it is necessary to deconvolve the response function from the data, in order to trace back to the pure shape of the electron energy distribution. The experience with the Mainz and Troitzk experiments shows that other factors, not predicted a priori, can appear after the data taking and analysis.

Another important effect is connected to the already mentioned role of the excited states in the source. In a spectrometer experiment the experimental beta spectrum is described by (1.28), while for the calorimetric approach by (1.34) - see section 1.4.3 for more details. It is the main points that distinguish the spectrometers from the calorimeters.

1.4.2 KATRIN

The Karlsruhe Tritium Neutrino (KATRIN) is a direct ν-mass experiment which is currently being set-up on the site of Tritium Laboratory at KIT by an international collaboration. The construction of the experiment is expected to be concluded in 2014. The goal of the experiment is to improve the sensitivity on the electron-neutrino mass by an order of magnitude down to 0.2 eV. KATRIN will push the MAC-E filter, where β electrons from a

windowless gaseous ^{3}H source are adiabatically guided to a system of electrostatic retarding spectrometer for energy analysis, to its technological limits. The KATRIN set-up is 70 m long. A decay rate of about 10^{11} Bq is required from the ^{3}H source cooled down to 27 K. A flux of 10^{19} T_2-molecules/s is injected at the midpoint of the source. An additional cryopumping section guarantees the T_2-flux entering in the spectrometer not to exceed 10^5 T_2/s. A pre-spectrometer will transmit only the uppermost end of the β-spectrum in order to reduce the background from ionizing collisions. Background electrons, which are emitted from the spectrometer walls, will be screened off electrostatically by an inner grid system. Strong attention has been put on the electromagnetic layout of the experiment in reference to the adiabatic transport of β electrons over more than 70 m, the alignment of the flux tube relative at the beam pipe, the minimization of the background as well as on the control of systematic uncertainties such as electron losses in the source.

1.4.3 The calorimetric approach

An alternative approach to spectrometry is calorimetry where the β-source is embeded in the detector so that all the energy emitted in the decay is measured, except for the one taken away by the neutrino. The part of the energy spent for the excitation of atomic or molecular levels is measured through the de-excitation of these states, provided that their lifetime be negligible with respect to the detector time response. In this way the measurement is completely free from systematics induced by any possible energy loss in the source and due to decays into excited final states.

In a calorimeter, the observed beta spectrum is a combination of different spectra and it can be obtained from equation (1.28) by operating the following replacements: $E_\beta \rightarrow E'_\beta = E_\beta - V_i$ and $p_\beta \rightarrow p'_\beta = ((E'_\beta = E_\beta - V_i)^2 - m_e^2c^4)^{1/2}$. These substitutions are motivated by the fact that calorimeters simultaneously measure the beta electron energy and the de-excitation energy V_i of the final state.

Noticed that $F(Z, E_\beta - V_i)S(E_\beta - v_i) \approx F(Z, E_\beta)S(E)$ and expanding in V_i/E_β one gets:

$$\begin{aligned} N(Z, E_\beta, m_{\nu_e}) \;\approx\; & p_\beta E_\beta (E_0 - E_\beta)^2 \left(1 - \frac{m_{\nu_e}^2 c^4}{(E_0 - E_\beta)^2}\right) F(Z, E_\beta) S(E_\beta) \\ & \sum_i w_i \left(1 - \frac{V_i}{E_\beta} - \frac{V_i E_\beta}{E_\beta^2 - m_e^2 C^4} + \frac{V_i^2}{2(E_\beta^2 - m_e^2 c^4)}\right) \end{aligned} \tag{1.34}$$

In case of vanishing neutrino mass, (1.34) describes a linear Kurie-plot in the final region ($E - \beta \gg V_i$). Focusing only on the case of the the first forbidden unique beta transition, the beta spectrum in (1.34) can be approximated by the following expression:

$$N_\beta(E, m_\nu) \approx \frac{3}{E_0^3}(E_0 - E)^2 \sqrt{1 - \frac{m_\nu}{(E_0 - E)^2}} \tag{1.35}$$

The main advantages of a calorimetric approach are:

- Measured of the energy spent in exciting states.
- No electron backscattering.
- No self-absorption problem.
- No reflection on the source substrate.

However, there is an important inconvenience which represents a serious limitation for this approach. In fact, in contrast to the spectrometric approach, the full beta spectrum is acquired. Therefore, the source activity has to be limited to avoid pile-up which would deform the shape of beta spectrum. As a consequence the statistics near the end-point is limited as well. This limitation may be then partially balanced by using β-emitting isotopes with an end-point energy as low as possible.

Another critical phenomenon which characterizes calorimetric detection is a solid state effect known as Beta Environmental Fine Structure (BEFS), which will be presented in detail in section 2.2.

1.4.4 Comparison between spectrometers and calorimeters

Nowadays the electrostatic spectrometers and calorimeters presented above are the most sensitive detection principles for a direct measurement of neutrino mass. Despite of the most stringent results come from spectrometers, the calorimetric approach is important as well. In fact, thanks to the different systematic effects of both approaches, which mainly result from using thick or thin beta-emitters, they are two complementary techniques with the same goal.

A comparison between spectrometers and calorimeters is presented in table 6.18.

1.5 The MARE project

MARE is a new large scale experiment to directly measure the neutrino mass with a calorimetric technique. The MARE project has a staged approach. The goal of the last phase (MARE-2) is to achieve a sub-eV sensitivity on neutrino mass. It will consist of several arrays of thermal microcalorimeters. The first phase (MARE-1) is a collection of activities with the aim of sorting out both the best isotope and the most suited detector technology to be used for the final experiment. The two competing isotopes are ^{187}Re and ^{163}Ho.

	electrostatic spectrometer	**calorimeter**
detector response	kinetic energy of beta-electron	entire energy
β-emmiters	thin source	thick source
β- energy interval	narrow interval near E_0	entire spectrum
β spectroscopy	integral spectrum	differential spectrum
experimental set-up	integral design	modular design
energy resolution	$\Delta E = 1$ eV (100%)	$\Delta E_{FWHM} = 30$ eV
systematic effects:	HV fluctuations, scattering	shape of beta spectrum,BEFS
	energy loss in source	electron escape

Table 1.6: Comparison between spectrometers and calorimeters. The calorimeter energy resolution is the one obtained with the available bolometers today.

Rhenium is in principle suited for fabricating thermal detectors. Metallic Rhenium crystals should allow to reach high sensitivity thanks to their low thermal capacity. Dielectric compounds can be also used. Up to now, only two β decay experiments have been carried out with thermal detectors: MANU [45, 118] and MIBETA [27, 117] experiments. MANU used metallic Rhenium single crystal as absorber, while MIBETA used $AgReO_4$ crystals. Collecting a statistic of about 10^7 events, they achieved an upper limit on neutrino mass of about 26 eV/c^2 at 95% CL and 15 eV/c^2 at 90% CL, respectively. In these experiments, the systematic uncertainties are still small compared to the statistical errors. The main sources of systematics are the background, the theoretical shape of the ^{187}Re β spectrum and the detector response function.

In order to have a viable alternative to the baseline MARE design using Rhenium β decay, the MARE collaboration is considering the possibility to use ^{163}Ho electron capture (EC) [119, 120].

Since the 80's ^{163}Ho EC decay has been the subject of many experimental investigations as a powerful means for neutrino mass determination thanks to its low transition energy ($\sim$ 2.5 keV). ^{163}Ho decays to ^{163}Dy and the capture is only allowed from the M shell or higher. The EC may be only detected through the mostly non radiative atom de-excitation of the Dy atom and from the Inner Bremsstrahlung (IB) radiation. There are at least three proposed independent methods to estimate the neutrino mass from the ^{163}Ho EC: a) absolute M capture rates or M/N capture ratios [36], b) IB end-point [37] and c) total absorption spectrum end-point [38].

There has been no experiment so far attempting to exploit the last method which consists in studying the end-point of the total absorption spectrum as proposed by De Rujula and Lusignoli [38]. The total spectrum is made up of peaks with Breit-Wigner shapes and it ends at $E_0 - m_\nu$, in analogy to what happens for β spectrum. Also in ^{163}Ho

experiments the sensitivity on m_ν depends on the fraction of events at the end-point. The various Q_{EC} determinations span from 2.2 to 2.8 keV [40], with a recommended value of 2.555 keV [39]. Figure 1.5 shows the ^{163}Ho EC decay calorimetric spectrum for two hypotetical Q_{EC} values and for a choice of parameters found in literature, while figure 1.6 shows the effect of a finite neutrino mass for a $Q_{EC} = 2.555$ keV.

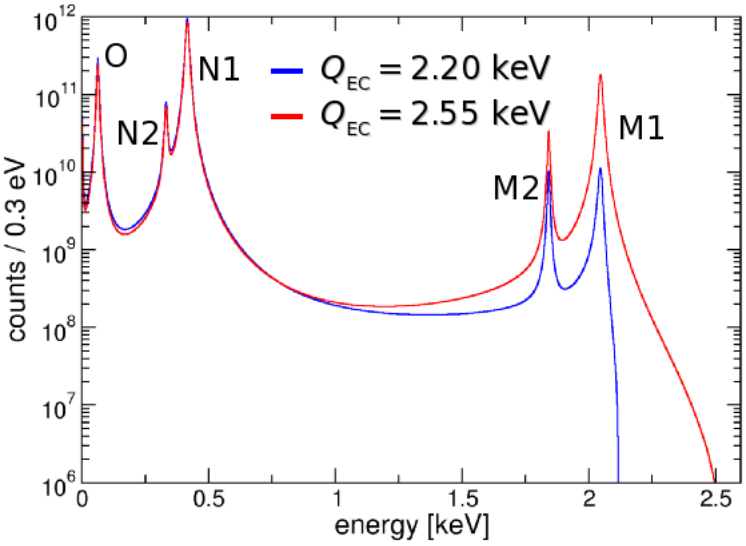

Figure 1.5: ^{163}Ho total absorption spectrum calculated for an energy resolution $\Delta E_{FWHM} = 2$ eV, a fraction of pile up event of $f_{pp} = 10^{-6}$ and a number of events equal to 10^{14}.

MARE-1 activities are devoted to the design of the single detector for the final MARE large scale experiment. This mainly consists in optimizing the coupling between Rhenium crystals - or ^{163}Ho implanted absorbers - and sensitive sensors like Transition Edge Sensor (TES) [41], Metallic Magnetic Calorimeters (MMC) [42] or Kinetic Inductance Detectors (MKID) [43].

1.5.1 MARE-1 in Milan

One of the MARE-1 activities is carried out in Milan by the group of Milano–Bicocca in collaboration with NASA/GSFC and Wisconsin groups. The Milan MARE-1 arrays are based on semiconductor thermistors, provided by the NASA/Goddard group, with dielectric silver perrhenate absorbers, $AgReO_4$. So far, the established energy and time resolutions are about 30 eV and 300 μs respectively. The experiment is designed to host up to 8 arrays. With 288 detectors - each with a mass of around 500 μg corresponding to a beta activity of 0.27 Hz - and such performances, a sensitivity of 4 eV at 90 % CL on the neutrino mass can be reached within 3 years. This corresponds to a statistics of about 10^{10} decays. The purpose of this experiment is also to investigate the systematics of ^{187}Re

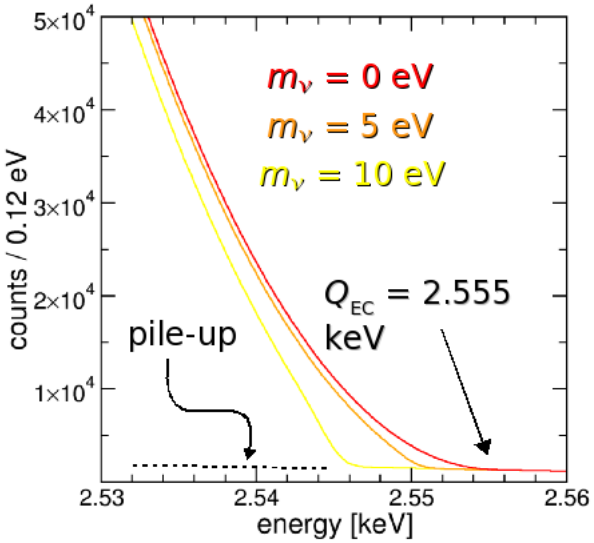

Figure 1.6: A zoom of the last part of the ^{163}Ho total absorption spectrum shown in figure 1.5.

neutrino mass measurements, focusing on those caused by the Beta Environmental Fine Structure (BEFS) and the beta spectrum theoretical shape.

Chapter 2

Calorimeter sensitivity

In this chapter a discussion of the potential sensitivity to the neutrino mass for a calorimetric experiment is presented.

2.1 Statistical sensitivity

First, we derive an algorithm to assess the statistical sensitivity for a given experimental configuration through an analytical approach. Then a Montecarlo method is described. The results of the analytic approach are then validated through the comparison with the Montecarlo results over a wide range of experimental parameters. Finally, the tools are applied to estimate the sensitivity on the neutrino mass of a present experiment (MARE-1 in Milan) and to investigate the optimal configuration for a future experiment based on Rhenium thermal detectors.

2.1.1 The analytic approach

The primary effect of a finite neutrino mass m_ν is to cause a tiny deformation of the beta spectrum close to the end-point energy E_0: the spectrum turns more sharply down to zero at a distance m_ν below the end-point as shown in the lower panel of figure (2.1). To look for a finite mass, we must be sensitive to the number of counts expected in this interval. The fraction of the total spectrum within an interval ΔE below the end-point E_0 is given by:

$$F_{\Delta E}(m_\nu) = \int_{E_0-\Delta E}^{E_0} N_\beta(E_\beta, m_\nu) dE \tag{2.1}$$

where $N_\beta(E_\beta, m_\nu)$ is the beta spectrum for a neutrino of mass m_ν normalized to unit. The signal to detect in counts is therefore:

$$signal = A_\beta N_{det} |F_{\Delta E}(m_\nu) - F_{\Delta E}(0)| t_M \tag{2.2}$$

where A_β is the beta activity, N_{det} is the number of identical detectors, t_M is the measuring time and $F_{\Delta E}(0)$ is (2.1) in the case of a zero neutrino mass.

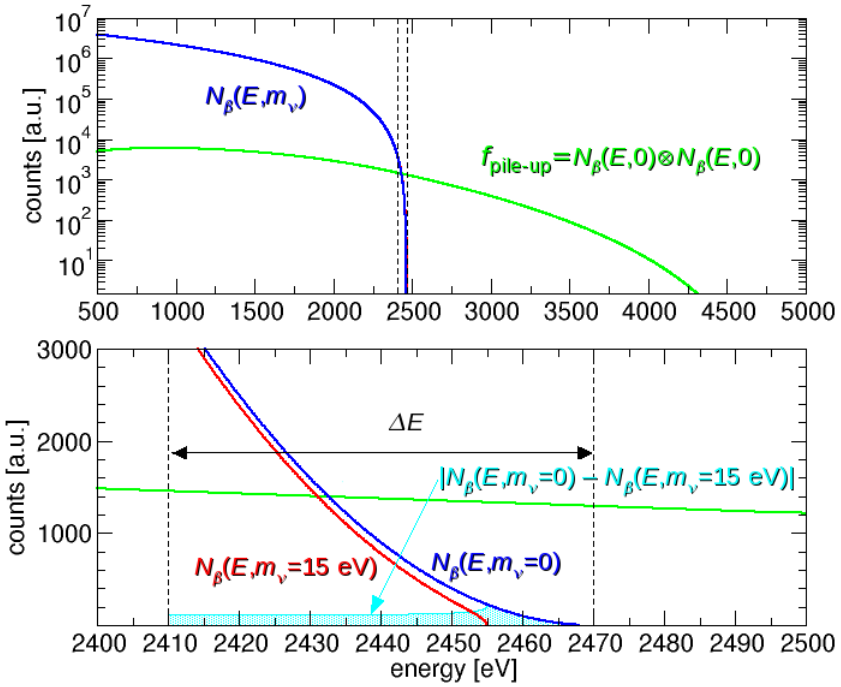

Figure 2.1: Higher panel: beta spectrum in blu compared to pile-up spectrum in green which extends up to $2E_0$. Low panel: zoom around the Rhenium end-point with a comparison between 0 and a finite neutrino mass spectrum.

The total spectrum of a calorimetric experiment is the sum of the beta decay events, the counts due to unresolved pile-up of two or more decays and any additional background counts from all detectors. In first approximation we can neglect the pile-up of more than two events. The pile-up spectrum can be approximated assuming a constant pulse-pair resolving time, τ_r , such that events with greater separation are always detected as being doubles, while those at smaller separations are always interpreted as singles with an apparent energy equal to the sum of the two events. This approximation is good enough to get the correct scaling and an approximate answer. In practice, τ_r is of the same order of magnitude of the detector rise time.

With these assumptions the pile-up spectrum is given by:

$$N_{pp}(E) = (1 - e^{-A_\beta \tau_R}) N_\beta(E,0) \otimes N_\beta(E,0) \tag{2.3}$$

where, at first order, $A_\beta \tau_R$ is the probability for the two event pile-up to occur, i.e. the fraction of unresolved pile-up events, f_{pp}. The pile-up spectrum extends up to $2E_0$ as shown in the higher panel of figure (2.1). So the fraction of the pile-up events which falls

in the region within ΔE of the end-point E_0 can be approximated by:

$$F^{pp}_{\Delta E} = \int_{E_0-\Delta E}^{E_0} N_{pp}(E)dE \approx A_\beta \tau_R \int_{E_0-\Delta E}^{E_0} N_\beta(E,0) \otimes N_\beta(E,0)dE \tag{2.4}$$

Using the equation (2.1) and (2.4) one can express the noise in counts as:

$$noise = \sqrt{A_\beta N_{det}(F_{\Delta E}(0) - F^{pp}_{\Delta E})t_M + N_{det} b \Delta E t_M} \tag{2.5}$$

where b is the average background counting rate for unity energy and for a single detector. Therefore, the signal to noise ratio can be expressed as:

$$\frac{signal}{noise} = \sqrt{N_{det} t_M A_\beta} \frac{|F_{\Delta E}(m_\nu) - F_{\Delta E}(0)|}{\sqrt{F_{\Delta E}(0) + F^{pp}_{\Delta E} + b\Delta E / A_\beta}} \tag{2.6}$$

This ratio must be equal to 1.7 for a sensitivity, $\Sigma_{90}(m_\nu)$, on neutrino mass at 90% confidence level. Therefore, one has to solve for m_ν the following equation:

$$1.7 = \sqrt{N_{ev}} \frac{|F_{\Delta E}(m_\nu) - F_{\Delta E}(0)|}{\sqrt{F_{\Delta E}(0) + F^{pp}_{\Delta E} + b\Delta E / A_\beta}} \tag{2.7}$$

where $N_{ev} = N_{det} t_M A_\beta$ is the total number of events, i.e. the total statistics of the experiment.

To evaluate (2.7), two approximate expressions for $F_{\Delta E}(m_\nu)$ and $F^{pp}_{\Delta E}$ can be used. In particular, if we only focus on the ^{137}Re case, which has a first forbidden unique beta transition, the shape of the beta spectrum can be approximated as seen in the previous section by:

$$N_\beta(E, m_\nu) \approx \frac{3}{E_0^3}(E_0 - E)^2 \sqrt{1 - \frac{m_\nu}{(E_0 - E)^2}} \tag{2.8}$$

which is a good approximation of the expected theoretical shape [44] as well as a perfect description of the experimental observations [27, 45].

In the case of a zero neutrino mass the expression (2.1) becomes:

$$F_{\Delta E}(0) = \left(\frac{\Delta E}{E_0}\right)^3 \tag{2.9}$$

while for a finite neutrino mass, using a second order expansion in $m_\nu/\Delta E$, the (2.1) approximately becomes:

$$F_{\Delta E}(m_\nu) \approx F_{\Delta E}(0) \left(1 - \frac{3m_\nu^2}{2\Delta E^2} + \frac{3m_\nu^4}{8\Delta E^4}\right) \tag{2.10}$$

Concerning the pile-up spectrum (2.3), using the approximate expression for the Rhenium beta spectrum given by (2.8), we can calculate between 0 and E_0:

$$N_{pp}(E) = (1 - e^{-A_\beta \tau_R}) \frac{1}{E_0} \left(9\frac{E}{E_0} - 18\frac{E^2}{E_0^2} + 12\frac{E^3}{E_0^3} - 3\frac{E^4}{E_0^4} + \frac{3}{10}\frac{E^5}{E_0^5} \right) \tag{2.11}$$

The expression $(1 - e^{-A_\beta \tau_R})$ can be approximated with $A_\beta \tau_R = f_{pp}$ because in all interesting experimental configurations $f_{pp} \ll 0.01$.

Substituting (2.11) in (2.4) and carrying out the integration we obtain:

$$F_{pp}(\Delta E) = f_{pp} \frac{1}{20} \left(6\frac{E}{E_0} + 15\frac{E^2}{E_0^2} + 20\frac{E^3}{E_0^3} - 15\frac{E^4}{E_0^4} - 6\frac{E^5}{E_0^5} - \frac{E^6}{E_0^6} \right) \tag{2.12}$$

Substituting equations (2.9),(2.10) and (2.11) in (2.7) and, keeping only the therms up to $(\Delta E/E_0)^3$ and considering that $(1 + f_{pp}) \approx 1$, the following expression is obtained:

$$\frac{m_\nu^2}{E_0^3} \left(\frac{3}{2}\Delta E - \frac{3m_\nu^2}{8\Delta E} \right) \sqrt{N_{ev}} = 1.7 \sqrt{\frac{\Delta E^3}{E_0^3} + f_{pp} \left(\frac{3\Delta E}{10E_0} + \frac{3\Delta E^2}{4E_0^2} \right) + b\Delta E/A_\beta} \tag{2.13}$$

which can be solved for m_ν to give the sensitivity on neutrino mass at 90% confidence level. Considering only the leading terms in (2.10) and (2.12) the solution is just:

$$\Sigma_{90}(m_\nu) = 1.13 \frac{E_0}{\sqrt[4]{N_{ev}}} \left[\frac{\Delta E}{E_0} + \frac{E_0}{\Delta E} \left(\frac{3}{10} f_{pp} + b\frac{E_0}{A_\beta} \right) \right]^{\frac{1}{4}} \tag{2.14}$$

The energy interval ΔE has to be correctly interpreted in order to make a meaningful use of (2.14). The first term in the square brackets in equations (2.14) represents the contribution to noise from the statistical fluctuations of the beta events, while the second one is the contribution due to the pile-up events. If the pile-up term is negligible, situation that happens when τ_R is short or when the beta activity A_β is low, the left term will dominate. Therefore, the interval of energy ΔE must be taken as small as possible, but it is obviously limited by the detector energy resolution. On the contrary, when the end-point is hidden by the pile-up events, the second term dominates. In this case, the signal to noise ratio improves by enlarging ΔE. As a consequence, there is not a defined value of ΔE. The solution we have found is to choose ΔE as the value that minimizes $\Sigma(m_\nu)$ for a given set of experimental parameters, taking into account that ΔE can not be smaller than the detector energy resolution ΔE_{FWHM}. In the case of equation (2.14), by deriving respect with ΔE, it is obtained:

$$\Delta E = max \left(E_0 \sqrt{\frac{3}{10} f_{pp} + b\frac{E_0}{A_\beta}}, \Delta E_{FWHM} \right) \tag{2.15}$$

The same approach can be applied to the more general case (2.13). In this case ΔE can be numerically evaluated after making the substitution $\Delta E \rightarrow |\Delta E_{opt}| + \Delta E_{FWHM}$. So

that the value of ΔE_{opt} which minimizes (2.13) is numerically found. Therefore, $\Sigma_{90}(m_\nu)$ is a functions of several parameters

$$\Sigma_{90}(m_\nu) = f(\Delta E_{opt}, \Delta E_{FWHM}, \tau_R, A_\beta, N_{det}, t_M, b) \tag{2.16}$$

Only in this way the detector energy resolution appears in equation (2.15) and (2.16).

2.1.2 The Montecarlo approach

A Montecarlo code has been developed to estimate the sensitivity of a neutrino mass experiment performed with thermal calorimeters. The approach is to simulate many β spectra, characterized by the same experimental set up, and to analyse them as the real ones. The statistical sensitivity is deduced from the distribution of the obtained m_ν^2 parameters. The Montecarlo parameters are: the total statistics N_{ev}, the detector energy resolution ΔE_{FWHM}, the fraction of unresolved pile-up events f_{pp} and the background b. All of them describe the entire experimental configuration. These input parameters can be derived from the ones actually characterizing a real experiment:

$$N_{ev} = N_{det} A_\beta t_M = T A_\beta \tag{2.17}$$

and by recalling (2.4)

$$f_{pp} = F^{pp}_{\Delta E = E_0} \approx A_\beta \tau_R \tag{2.18}$$

where, again, N_{det} is the number of detectors, A_β is the beta decay activity of a single detector, t_M is the measuring time, τ_R is the pile-up resolving time and $T = N_{det} t_M$ is the exposure. Several steps lead to estimate the statistical sensitivity:

– Evaluation of the theoretical spectrum $S(E)$ which is expected to be measured by the virtual experiments

$$S(E) = [N_{ev}(N_\beta(E, m_\nu) + f_{pp} N_\beta(E, 0) \otimes N_\beta(E, 0)) + b(E)] \otimes R(E) \tag{2.19}$$

where $N_\beta(E, m_\nu)$ is the rhenium beta spectrum normalized to unity, $b(E)$ is the background energy spectrum and $R(E)$ is the detector energy response function. The $b(E)$ function is usually taken as a constant $b(E) = bT$, while the response function $R(E)$ is assumed to be a symmetric Gaussian:

$$G(E) = \frac{1}{\sigma\sqrt{2\pi}} e^{-\frac{E^2}{2\sigma^2}} \tag{2.20}$$

where σ is the standard deviation ($\sigma = \Delta E_{FWHM}/2.35$).

– The virtual outcome of a large number (between 100 and 1000) of experiments is numerically generated by letting the spectrum $S(E)$ fluctuate according to a Poisson statistics. The simulated experimental spectra are generated on an energy interval which is smaller than the full $0 - 2E_0$ interval.

– Each simulated spectrum is fitted using (2.19) and leaving m_ν^2, E_0, N_{ev}, f_{pp} and b as free parameters.The fit is restricted to an energy interval smaller than the one used for the simulated spectrum generation.

– The statistical sensitivity on m_ν at 90%CL is given by

$$\Sigma_{90}(m_\nu) = \sqrt{1.7\sigma^2_{m_\nu}} \tag{2.21}$$

where $\sigma^2_{m_\nu}$ is the standard deviation of the distribution of the m_ν^2 found by fitting the spectra

$$\sigma^2_{m_\nu^2} = \frac{1}{N-1}\Sigma_i(m^2_{\nu_i} - \overline{m^2_\nu})^2 = \frac{N}{N-1}(\overline{m^4_\nu} - \overline{m^2_\nu}^2) \tag{2.22}$$

where N is the number of generated spectra and $m^2_{\nu_i}$ are the values found in each fit.

– Estimation of the statistical error on the 90%CL m_ν. Defining $y_i = (m^2_{\nu_i} - \overline{m^2_\nu})^2$, $\overline{y} \approx \sigma^2_{m_\nu^2}$ and we can write:

$$\sigma^2_y = \frac{N}{N-1}(\overline{y^2} - \overline{y}^2) \approx \frac{N}{N-1}\left[\frac{1}{N}\Sigma(m^2_{\nu_i} - \overline{m^2_\nu})^4 - \sigma^4_{m_\nu^2}\right] \tag{2.23}$$

The error on $\sqrt{\overline{y}} = \sigma_{m_\nu^2}$ is given by

$$\epsilon_{\sqrt{\overline{y}}} = \frac{1}{2}\sqrt{\frac{\sigma^2_y}{N\sigma_{m_\nu^2}}} \tag{2.24}$$

and consequently the error on $\Sigma_{90}(m_\nu)$ is just:

$$\epsilon_{\Sigma_{90(m_\nu)}} = \frac{1.7}{2}\frac{\epsilon_{\sqrt{\overline{y}}}}{\Sigma_{90}(m_\nu)} \tag{2.25}$$

2.1.3 Statistical analysis vs Montecarlo approach

The predictions of the two approaches have been compared for a wide range of experimental configurations suitable for obtaining a sub-eV neutrino mass sensitivity. The results obtained are shown in figure (2.2),(2.3),(2.4) and (2.5). In all plots the symbols are the Montecarlo results, the continuous lines are obtained through equations (2.14) and (2.15),

while the dashed lines are obtained from (2.13). At this scale the Montecarlo errors are negligible. In fact, according to equation (2.25) the statistical error on the Montecarlo results is around 3% and 1% for about 100 and 1000 simulated spectra, respectively.

Figure 2.2 displays the dependence of the neutrino mass sensitivity on the total statistics N_{ev}. The greatest reduction on the limit of m_ν happens when increasing the statistics. To reach a sensitivity on m_ν of 0.1 eV, an energy resolution of 1 eV and a pile-up fraction of the order of 10^{-6} are needed. Furthermore, the results show that the 90% confidence level sensitivity is proportional to $N_{ev}^{-1/4}$, this dependence may be exploited to scale the Montecarlo results.

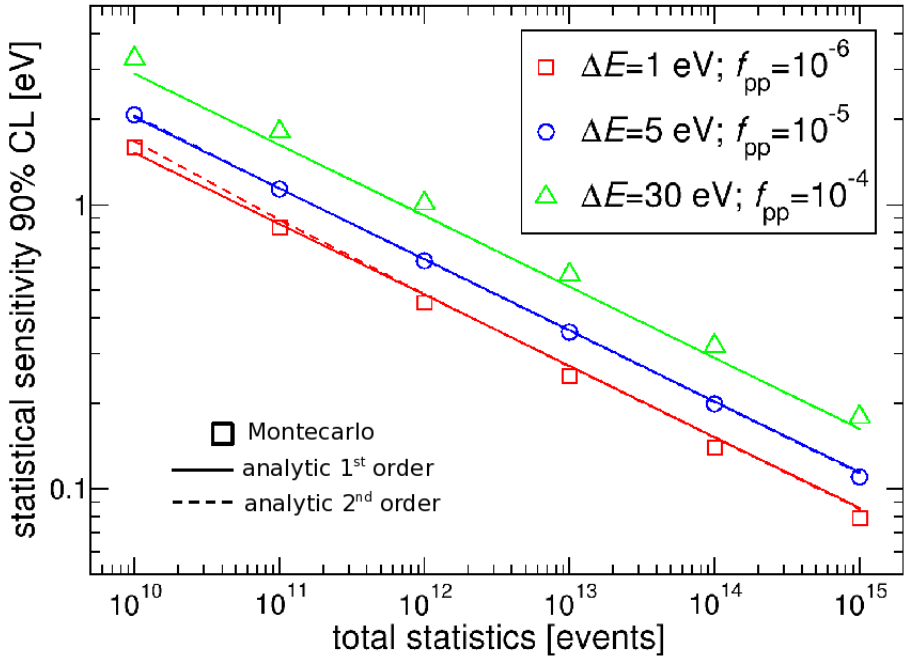

Figure 2.2: Comparison between the statistical sensitivity as estimated by a Montecarlo approach (symbols) and by the analytic formulation (lines). The continuous and dashed lines are obtained using (2.14) with (2.15) and (2.16) respectively.

In figure 2.3 it has been shown how the impact of the energy resolution on the sensitivity is reduced for high values of f_{pp}. This plot also points out the limit of the analytic approach described above: the poor consideration of the detector energy resolution which translates in a too weak dependence of the sensitivity on this parameter.

In figure 2.4 the dependence of the statistical sensitivity on the beta activity A_β is displayed. It shows how the statistical sensitivity improves increasing the beta activity, with the other parameters fixed and for an exposure T of 10000 detector x year.

Finally, figure 2.5 shows the impact of a continuous background below the rhenium beta spectrum for different experimental configurations. The abscissa is the ratio between

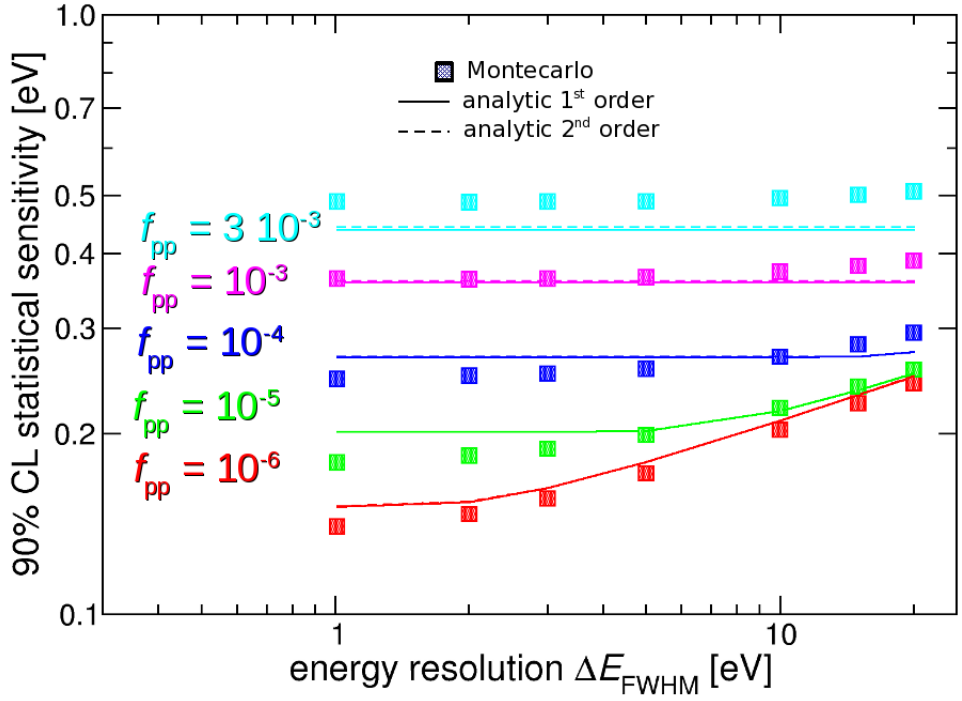

Figure 2.3: Comparison between the statistical sensitivity as estimated by a Montecarlo approach (symbols) and by the analytic formulation (lines) for a total statistics N_{ev} of 10^{14} events. Continuous and dashed lines are as in figure 2.2.

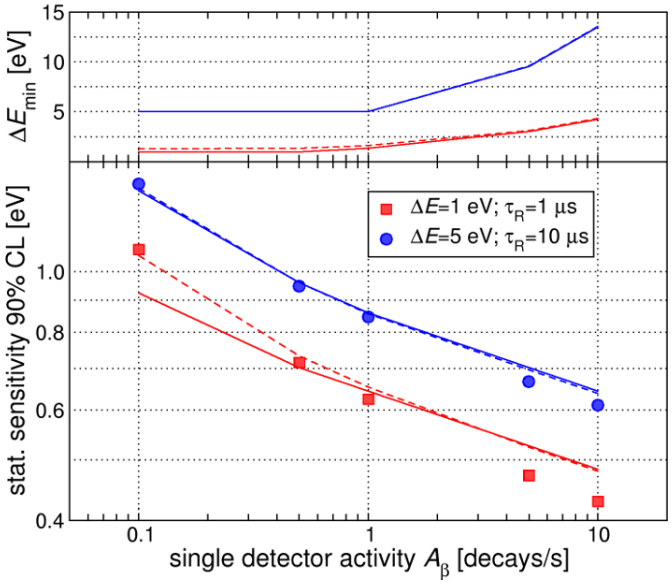

Figure 2.4: Comparison between the statistical sensitivity as estimated by a Montecarlo approach (symbols) and by the analytic formulation (lines). Continuous and dashed lines are as in figure 2.2. The statistical sensitivity is evaluated for an exposure $T = 10000$ detector $\times$ year. The upper panel shows how ΔE_{opt} gets larger as the pile-up spectrum increases its weight.

the total events N_{ev} and the number of background counts N_{bck} between 0 and E_0, where $N_{bck} = bE_0T$. The number of total events N_{ev} is set to 10^{14}. The presence of a high background deteriorates the sensitivity on neutrino mass. Clearly, the impact is lower for higher pile-up fractions f_{pp}.

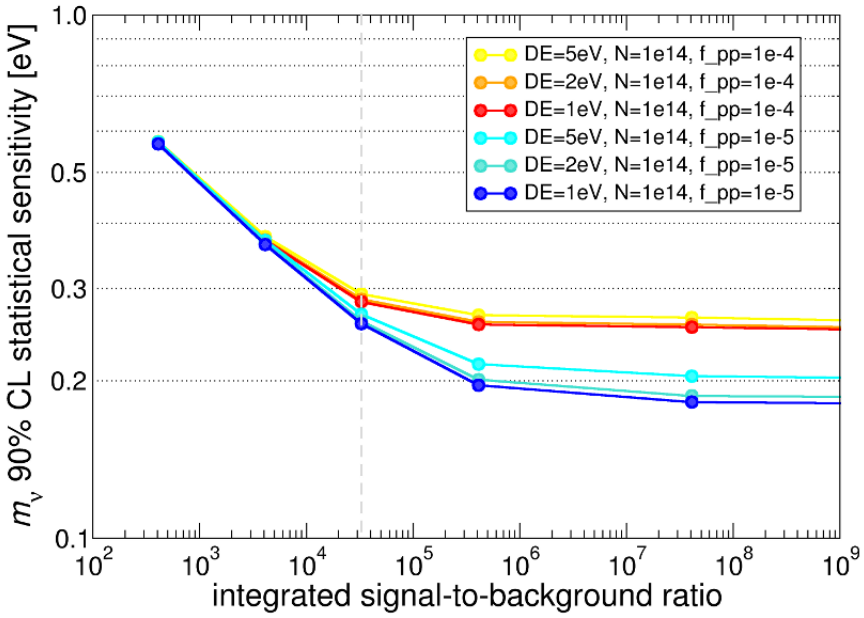

Figure 2.5: Comparison between the statistical sensitivity as estimated by a Montecarlo approach (symbols) and by the analytic formulation (lines). The integrated signal-to-background ratio is given by N_{ev}/N_{bkg} where $N_{bkg} = bE_0T$ and $N_{ev} = 10^{14}$. An integrated ratio of about $3{\times}10^4$ corresponds to the background level measured in the MIBETA experiment.

Although the agreement is only partial, the comparison confirms that the analytic formulation goes in the right direction and it can be used to make useful predictions. Nevertheless, the most accurate estimate of the sensitivity is the one obtained through the Montecarlo approach. In fact, the formula tends to overestimate the sensitivity for increasing ΔE_{opt}, i.e. when the sensitivity is limited by the pile-up or the continuous background. As a general check, the two approaches can be applied to the MIBETA experiment. For $N_{ev} = 1.7 \times 10^7$, $\Delta E_{FWHM} = 28.5$ eV, $f_{pp} = 2.3 \times 10^4$ and $N_{ev}/N_{bkg} = 3.28 \times 10^4$ one obtains a sensitivity at 90% C.L. of about 15 and 17 eV, using equations (2.14) and the Montecarlo respectively, while the limit on the neutrino mass reported in [27] is about 16 eV at 90% C.L.

2.1.4 Present and future calorimetric experiments

The two methods described above are applied to estimate the sensitivity on neutrino mass of a present experiment (MARE-1 in Milan) and to investigate the optimal configuration for a future experiment based on Rhenium thermal detectors (MARE-2).

MARE-1 in Milan

As said in the previous chapter, the Milano MARE-1 experiment will consist of 288 detectors, each characterized by a beta activity of 0.27 Hz. Taking into account these two constraints dictated by the experimental configuration and using the Montecarlo approach, the sensitivity on neutrino mass at 90% CL is evaluated for the Milano MARE-1 experiment. Figure 2.6 shows the statistical sensitivity on neutrino mass at 90% CL versus the total statistics for three different possible configurations of MARE-1.

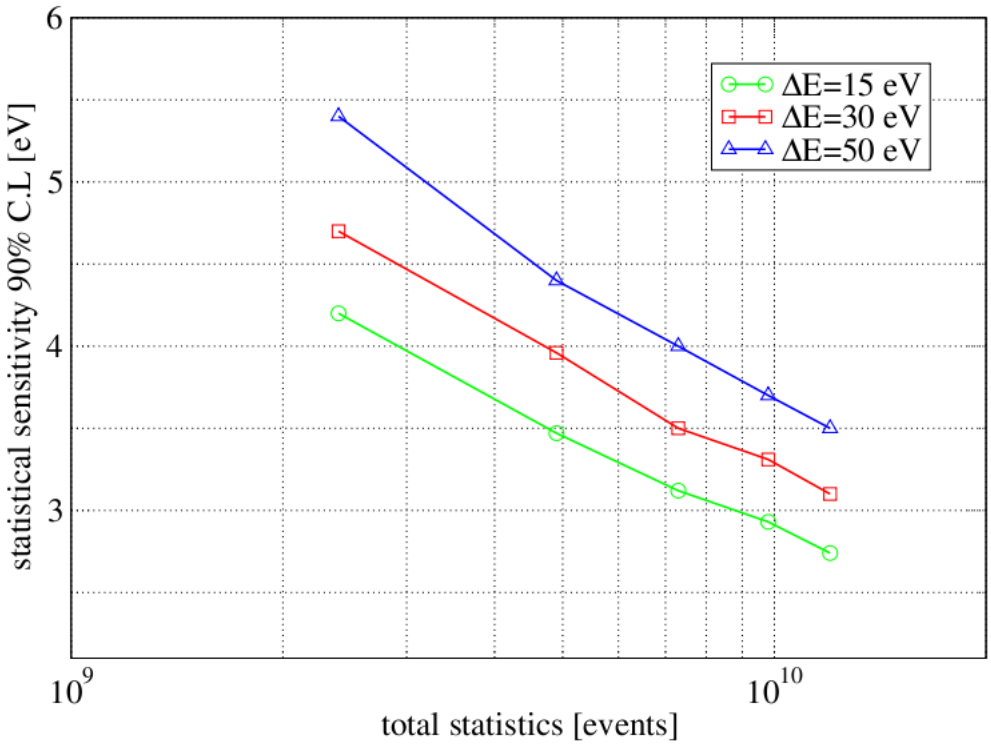

Figure 2.6: The statistical sensitivity estimated by a Montecarlo approach versus the total statistics for different values of ΔE_{FWHM} and the same value of $f_{pp} = 10^{-4}$. For each configuration 500 spectra are simulated.

Tables 2.1 and 2.2 report the results obtained changing the exposure $T = N_{ev} t_M$, the energy (ΔE_{FWHM}) and time (τ_R) resolution in absence of background.

τ_R [μs]	ΔE_{FWHM} [eV]	N_{ev} [counts]	Exposure T [det $\times$ years]	$\Sigma_{90}(m_\nu)$ [eV]
300	15	2.4×10^9	288	4.1
	30			4.6
	50			5.2
400	15	2.4×10^9	288	4.2
	30			4.7
	50			5.4
500	15	2.4×10^9	288	4.4
	30			4.8
	50			5.4
300	15	4.9×10^9	576	3.4
	30			3.9
	50			4.4
400	15	4.9×10^9	576	3.5
	30			4.0
	50			4.4
500	15	4.9×10^9	576	3.7
	30			3.9
	50			4.4
300	15	7.3×10^9	864	3.1
	30			3.4
	50			3.8
400	15	7.3×10^9	864	3.1
	30			3.5
	50			4.0
500	15	7.3×10^9	864	3.2
	30			3.6
	50			3.9

Table 2.1: Montecarlo results obtained changing the exposure $T = N_{ev} t_M$, the energy (ΔE_{FWHM}) and time (τ_R) resolution in absence of background for the Milano MARE-1 experiment.

τ_R [μs]	ΔE_{FWHM} [eV]	N_{ev} [counts]	Exposure T [det $\times$ years]	$\Sigma_{90}(m_\nu)$ [eV]
300	15	9.8×10^9	1152	2.8
	30			3.3
	50			3.6
400	15	9.8×10^9	1152	2.9
	30			3.3
	50			3.7
500	15	9.8×10^9	1152	2.9
	30			3.4
	50			3.7
300	15	12×10^9	864	2.7
	30			3.0
	50			3.4
400	15	12×10^9	864	2.7
	30			3.1
	50			3.5
500	15	12×10^9	864	2.8
	30			3.2
	50			3.6

Table 2.2: Montecarlo results obtained changing the exposure $T = N_{ev} t_M$, the energy (ΔE_{FWHM}) and time (τ_R) resolution in absence of background for the Milano MARE-1 experiment.

For example a target neutrino mass of 3.0 eV at 90% CL could be achieved in 3 years using 288 detectors, each with an energy and time resolutions of about 30 eV and 300 μs, respectively.

Since only two arrays are installed up to now, it is useful to estimate the sensitivity on neutrino mass over the years by increasing the detectors number from year to year. For that estimation the equation (2.14) is used in the case of a zero background. The results are listed in table 2.3 and they are displayed in figure 2.7.

$\mathbf{t}_M$ **[years]**	1	2	3	4	5
$\mathbf{N}_{det}$	72	144	288	288	288
Exposure [det $\times$ **years]**	72	216	504	792	1080
$\mathbf{N}_{ev}$ **[counts]**	6.1×10^8	1.8×10^9	4.3×10^9	6.7×10^9	9.2×10^9
a) $\Sigma_{90}(m_\nu)$ **[eV]**	6.1	4.7	3.8	3.4	3.1
b) $\Sigma_{90}(m_\nu)$ **[eV]**	6.5	5.0	4.0	3.6	3.3
c) $\Sigma_{90}(m_\nu)$ **[eV]**	6.9	5.2	4.2	3.8	3.5

Table 2.3: Results obtained considering detectors characterized by an energy resolution of 30 eV and a time resolution of 300 μs (series a), by an energy resolution of 40 eV and a time resolution of 400 μs (series b) and by an energy resolution of 50 eV and a time resolution of 500 μs (series c).

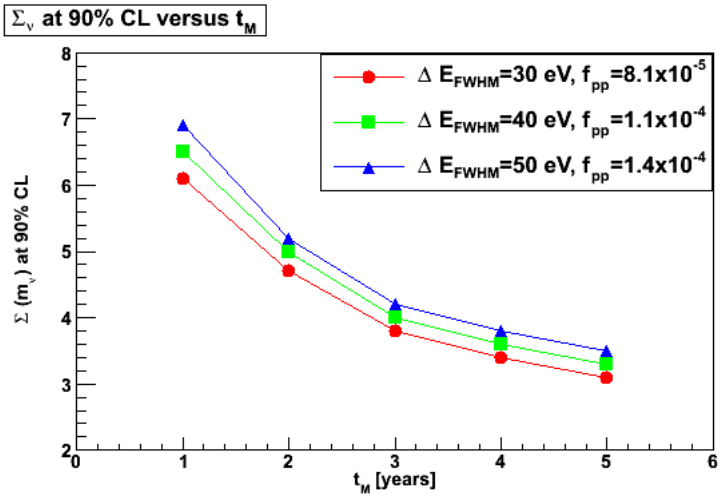

Figure 2.7: Sensitivity on neutrino mass at 90% CL versus the measuring time t_M in years. The number of detectors is increasing up to 288 (i.e. the final number) during the years. The number of detectors is 72 in the first years, 144 in the second year and 288 from the third year onwards.

Running only two arrays (i.e. 72 detectors with an energy and time resolution of 30 eV and 300 μs, respectevely) for 3 years the upper limit on neutrino mass which could be achieved is 4.7 eV at 90% CL.

MARE-2

Since the second phase of MARE (i.e. MARE-2) is only a project, no experimental constraints are presented. It is precisely for this reason that a Montecarlo analysis is needed to determine the best experimental configuration, which will allow to achieve a sub-eV sensitivity on neutrino mass.

The main question is whether it is desirable to keep the pile-up negligible or not. On one hand, increasing the pile-up by increasing the beta activity (A_β) allows to accumulate more quickly large statistics and when pile-up dominates the dependence on the energy resolution - which tends to degrade when A_β increases - is attenuated (see figure 2.4 and 2.5). On the other hand, the background caused at the end-point by the pile-up, together with a degraded energy resolution, may impair the ability to recognize and understand systematic effects. In any case the single channel activity A_β is limited by technical considerations concerning the performance of the thermal detector (heat capacity, quasiparticle diffusion length, ...). Therefore, single beta activities higher than 10 Hz are not considered.

The scaled Montecarlo results for a target sensitivity $\Sigma_{90}(m_\nu)$ of 0.2 eV and 0.1 eV are listed in tables 2.4 and 2.5. Also in this case the results are obtained in absence of background. The first line is a baseline experimental configuration characterized by high energy and time resolution and by a limited pile-up fraction f_{pp}, which is obtained considering a single beta activity of 1 Hz. In this condition the low statistics is balanced by a large exposure T. In the other lines of the tables an activity of 10 Hz is considered together with a progressive degradation of energy and time resolutions. The poorer performances are compensated by the need of a larger statistics. From the tables it is clear that one can find a compromise between performances and exposure which is more convenient than the baseline experimental configuration shown in the first line.

A_β **[Hz]**	τ_R [μs]	ΔE_{FWHM} **[eV]**	N_{ev} **[counts]**	**Exposure** T **[det** $\times$ **years]**
1	1	1	0.2×10^{14}	7.6×10^5
10	1	1	0.7×10^{14}	2.1×10^5
10	3	3	1.3×10^{14}	4.1×10^5
10	5	5	1.9×10^{14}	6.1×10^5
10	10	10	3.3×10^{14}	10.5×10^5

Table 2.4: Exposure required to achieve a sensitivity on neutrino mass of 0.2 eV.

For example, the Montecarlo approach shows that a neutrino mass sensitivity of 0.1 eV at 90% CL could be expected in 10 years running 3x10^5 detectors, each with a mass of 10

A_β [**Hz**]	τ_R [μ**s**]	ΔE_{FWHM} [**eV**]	N_{ev} [**counts**]	**Exposure** T [**det** $\times$ **years**]
1	0.1	0.1	1.7×10^{14}	5.4×10^6
10	0.1	0.1	5.3×10^{14}	1.7×10^6
10	1	1	10.3×10^{14}	3.3×10^6
10	3	3	21.4×10^{14}	6.8×10^6
10	5	5	43.6×10^{14}	13.9×10^6

Table 2.5: Exposure required to achieve a sensitivity on neutrino mass of 0.1 eV.

mg ($\sim$ 10 Hz) and with energy and time resolutions of about 1 eV and 1 μs respectively.

2.2 Systematic uncertainties

In a calorimetric neutrino mass experiment the beta source is embedded in the detector so that the experiment is considered free from systematics related to the external source effects. Nevertheless, it may be affected by other systematics uncertainties.

Some effects as the electron escape, the shape of the beta spectrum and BEFS are related to the beta source and, as a consequence, they may be present also in the calorimetric experiments. In order to minimize the related uncertainties, these effects must be precisely modelled with the help of theoretical investigations, independent experiments and Montecarlo simulations. Other systematic uncertainties arising from instrumental effects can be smoothed through an improved detector design as well as a careful off-line analysis.

The Montecarlo code described in the previous section can be adapted to estimate the many systematic effects due to a lack of accuracy with which the experimental parameters are determined and due to an incomplete or incorrect modelling of the data. To asses the systematic uncertainties of the first category the parameters are randomly fluctuated with a given accuracy, while they are fixed to their average value in the fitting function $S(E)$. For the second category of systematic uncertainties the adopted approach is to include the effects in the generated spectra, but not in the fitting function S(E). During my ph.D I have focused on the second category.

As a results of both procedures, there is a shift of m_ν^2 away from zero and, in some cases, there is a sensible deterioration of the sensitivity as shown by the wider error bars in the plot. The goal of this analysis is to identify the size of the inaccuracy or of the neglected effect for which the shift remains within a given limit.

Related to the source

– **Excited final states**
The beta spectrum is not perturbed by beta decays to excited final states if the state lifetimes are shorter then the detector integration time. In fact, while an excitation energy E_{exc} lost in the beta decay shifts the end point to $E_0' = E_0 - E_{exc} < E_0$, at the same time the coincident detection of the energy E_{exc} released in the de-excitation state adds an energy offset to the beta spectrum. As a consequence, to each excited state corresponds a beta spectrum starting at E_{exc} and with an end-point $E_0 = E_0' + E_{exc}$. Thanks to its simple energy dependence the rhenium beta decay spectral shape above E_{exc} remains unperturbed.

– **Electron escape**
A fraction of electrons emitted in the decays of ^{187}Re nuclei close to the detector surface can not be contained in the calorimeter. A Geant4 toolkit is used to estimate the type and magnitude of this effect on the measured spectrum. Figure 2.8 shows the results for a 1 mg cubic Rhenium detector in terms of relative deviation with respect to the spectrum given by (2.8). The simulation has been repeated for the available Geant4 low energy extensions and for different energy cuts applied in the electron transport. The results shown in figure 2.8 are obtained using the Penelope extension. These tests have confirmed the shape of the effect and its magnitude. Therefore, the effect on measured spectrum can be parametrized as a multiplicative factor to include in (2.8)

$$f_{esc}(E) = 1 - a_{esc}\frac{E}{E_0} \tag{2.26}$$

where the parameter a_{esc} will have to be left free in the data analysis. Therefore, taking into account this correction the beta spectrum becomes:

$$N'(E) = f_{esc}(E)N(E) \tag{2.27}$$

where $N(E)$ is given by equation (2.8). The line in figure 2.8 corresponds to $a_{esc} = 1.9 \times 10^{-5}$.

Subsequently, the systematic error arising when this effect is not included in the data analysis for various value of a_{esc} has been estimated (see figure 2.9).

Beta spectrum uncertainties

– **Spectral shape**
Up to now equation (2.8) has well described the ^{187}Re beta decay spectrum, but future high statistic experiments will need a more precise description of the spectrum.

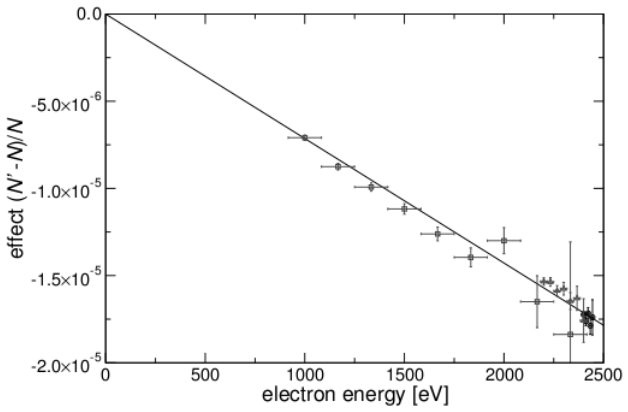

Figure 2.8: Spectral distortion caused by surface electron escape. The Montecarlo simulation is carried out for a 1 mg cubic Rhenium detector. The effect plotted in the graph is $N(E') - N(E)/N(E)$, where $N(E)$ is given by equation (2.8) and $N'(E) = f_{esc}(E)N(E)$ versus the electron energy.

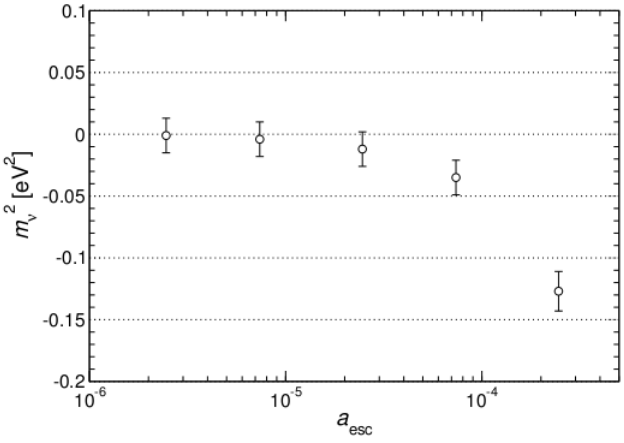

Figure 2.9: Systematic m_ν^2 shift caused by ignoring the electron escape. Points obtained for $N_{ev} = 10^{14}$, $\Delta E_{FWHM} = 1.5$eV, $f_{pp} = 10^{-6}$ and in absence of background.

To estimate the sensitivity deviations from the simple equation (2.8) the following corrective factor has to be introduced

$$f_{corr}(E) = 1 + a_1 E + a_2 E^2 \tag{2.28}$$

which is an extension of the correction for the escape of beta electrons. The effect of this correction has been investigated by generating the experimental spectra according to a modified beta spectrum $N'(E) = N(E) f_{corr}(E)$ and fitting them using the regular beta spectrum $N(E)$ in $S(E)$. Figure 2.10 shows the effect on m_ν^2 for different values of a_1 and a_2, while figure 2.11 displays the results for positive values of a_i coefficients.

For example, one can consider that the deviation of the beta spectrum given by (2.8) with respect to the theoretical one given in [46] can be parametrized as:

$$f_{corr} \sim 1.0 - 1.8 \times 10^{-5} E + 2.8 \times 10^{-10} E^2 - 3.5 \times 10^{-15} E^3 + ... \tag{2.29}$$

Neglecting this correction m_ν^2 is systematically shifted by about -280 eV^2.

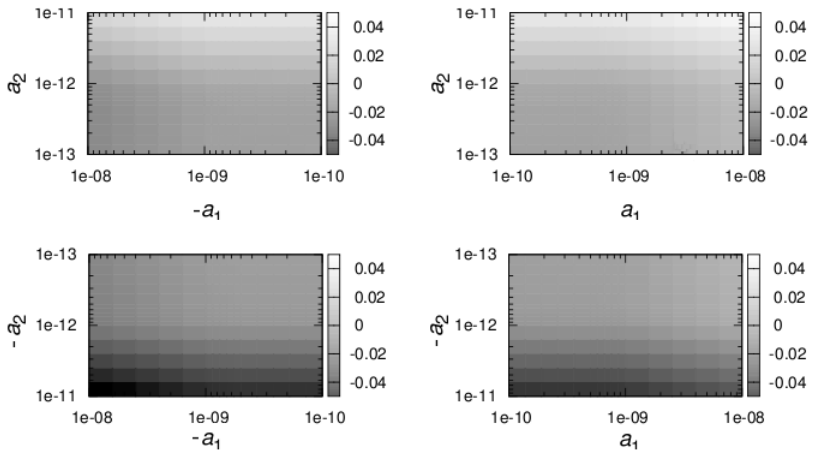

Figure 2.10: Systematic m_ν^2 shift due to a deviation of the beta spectrum from (2.8). The four graphs represent the (a_1, a_2) plane, where a_1 and a_2 are the corrections coefficients introduced in (2.29). The colour coded z-axis is the m_ν^2 value. In this case the Montecarlo parameters are $N_{ev} = 10^{14}$, $\Delta E_{FWHM} = 1.5eV$, $f_{pp} = 10^{-6}$. The results are obtained in a zero background configuration.

– **Beta Environmental Fine Structure**

The Beta Environment Fine Structure (BEFS) is a modulation of the beta spectrum due to the atoms surrounding the decaying nuclei and it has been theoretically

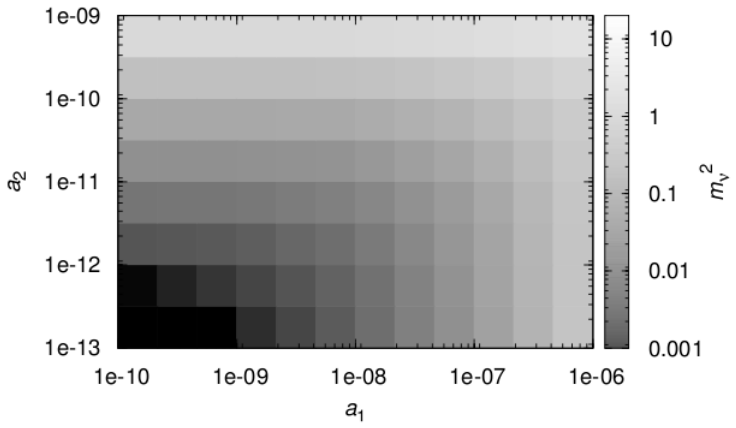

Figure 2.11: Detail of the first quadrant where both a_i are positive for a wider range and with logarithmic z-axes.

suggested in 1991 by Koonin [47] in analogy with Extended X-ray Absorption Fine Structure (EXAFS) [48]. The EXAFS is the oscillatory pattern observed in X-ray absorption spectra just above the absorption edges as an effect of the interference between the direct wave of the ejected photoelectron and the waves scattered by neighbouring atoms. These oscillation effects depend on the interatomic distance, while their amplitude is tied to electron-atom scattering cross section. In BEFS the beta electron plays the same role of the photoelectron in EXAFS. In fact, the electron emitted by a nucleus is reflected by neighbouring atoms of a molecule or of a crystal, where the emitting nucleus is embedded. It could be detected in the low energy region of the beta spectrum, which is generally more populated when the transition energy is low. Koonin had theoretically evaluated this effect for ^{14}C and ^{3}H. The BEFS effect has not been searched in these nuclei, but it has been detected in metallic Rhenium by F. Gatti et al [49] in 1999 and in $AgReO_4$ [50] only below 1.5 keV where it is larger.

For future neutrino mass experiment a very accurate description of the BEFS modulation up to the beta spectrum end-point is needed. Since the beta spectra acquired up to now are characterized by a low statistics and since for a safe extrapolation up to the end-point of the BEFS effect beta spectra must be characterized by a much higher statistics, the only possible way to study this effect is trough a Montecarlo simulations. The Montecarlo approach can be used to show the shift on m_ν^2 when data with BEFS included are fitted to a model without BEFS. For the BEFS function it is assumed that the one used to interpolate the data up to 1.5 keV can be used up to the end-point without modifications. Figure 2.12 shows the results of a Montecarlo simulation of the Rhenium BEFS in terms of residuals of the fit. The

Montecarlo is for a statistics of 10^{10} events. Figure 2.13 displays what happens to m_ν^2 when fitting spectra like the one in figure 2.12 with different left boundaries of the fitting energy interval. The effect worsens when the left boundary is moved to lower energies where the BEFS gets larger. The plot confirms that the inclusion of the BEFS in the end-point analysis is mandatory.

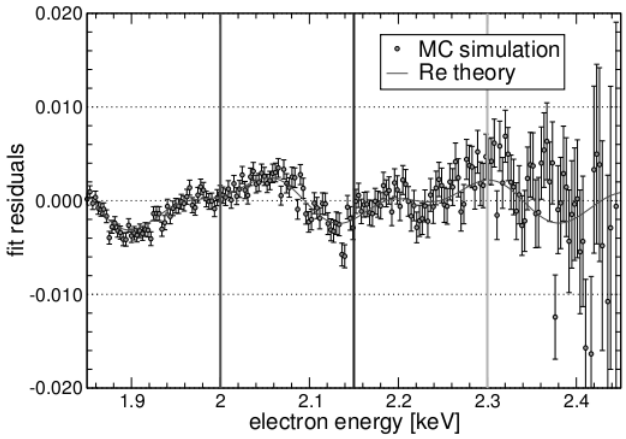

Figure 2.12: Residuals from the fit of a Montecarlo generated beta spectrum with BEFS using a fit function without BEFS. The Montecarlo parameters are $N_{ev} = 10^{10}$, $\Delta E_{FWHM} = 5$ eV, $f_{pp} = 10^{-5}$ and in absence of background.

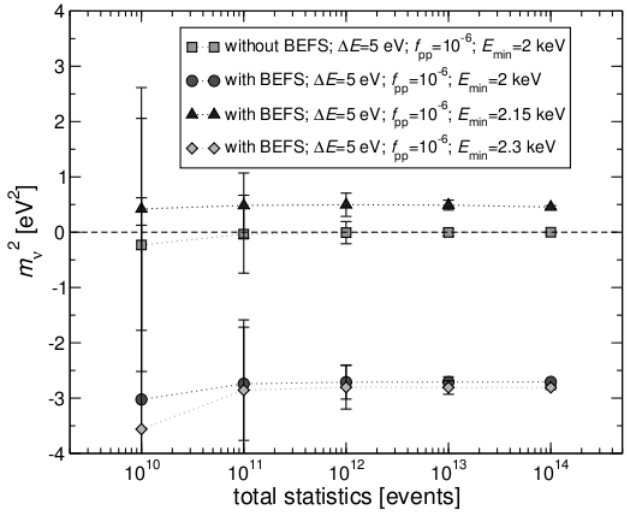

Figure 2.13: Systematic effects caused on m_ν^2 by neglecting the BEFS effect when fitting the Montecarlo generated spectra. Different left energy boundaries are considered. The Montecarlo parameters are $N_{ev} = 10^{10}$, $\Delta E_{FWHM} = 5$ eV, $f_{pp} = 10^{-6}$ and in absence of background.

Chapter 3

Light and heavy neutrinos

In this chapter the capabilities of MARE to measure the mass of heavy (sterile) neutrinos is presented.

3.1 Heavy Neutrinos

One of the most exciting problems in astrophysics and cosmology, but also one of the most attractive connection points of these fields to elementary particle physics is the explanation of the Dark Matter (DM). In fact, although the existence of Dark Matter (DM) was inferred in the Thirties [51, 51, 53], its nature remains still elusive. Dark Matter could be cold, hot or warm depending on its velocity despersion. Many different hypotetical particles coming from physics beyond the Standard Model has been proposed to play a role of dark matter particle during the years; but none of them have been discovered yet.

A possible warm Dark Matter (WDM) candidate is a sterile neutrino [54]-[63] with a mass in the keV range and produced via their mixing and oscillation with an active neutrino species. Other possible WDM candidates in the KeV mass scale are: gravitonos, light neutralinos and majorons [64]-[75].

A possible argument about the admixture of heavy neutrinos is the "quark and lepton symmetry": there are both left and right handed quarks while the active neutrinos are only left handed; it is thus natural to have right handed neutrinos besides the well known left-handed active neutrino. Sterile neutrinos can be naturally embedded in the Standard Model of Particle Physics. They do not participate in weak interactions and one sterile neutrino per lepton is expected. Only the lightest one (i.e. electron family) has a lifetime such that it can describe the DM.

A recent re-analysis of existing reactor data by Mention and collaborator [76] appears compatible with the existence of a fourth non standard neutrino, corresponding in the flavour basis to the existence of a sterile neutrino. In fact, the oscillation of electron neutrinos into a new neutrino state with a large $|\Delta m_{sterile}|$ could be a possible explanation of

the reactor neutrino anomaly valuated by Mention and collaborators. A combined analysis using available reactor data, as well as data collected by gallium solar neutrino calibration experiments [77, 78] and the MiniBooNe data [79] leads to the following constraints on oscillation parameters: $|\Delta m^2_{sterile}| < 1.5\text{eV}^2$ and $\sin^2(\theta_{sterile}) = 0.14 \pm 0.08$ at 95% CL, disfavouring the non-oscillation case at 99.8% CL.

3.2 Heavy Neutrinos and β decay

Experimental methods investigating weak decays or looking directly for decay involving neutrinos are indicated to test the assumption of heavy neutrino existence [80]. Particularly for neutrino masses above some tens of eV and below 1 MeV, beta decay experiments looking for a kinks in the energy spectra of the emitted electron are most sensitive. Experiments of this kind has been performed on ^{3}H, ^{35}S, ^{63}Ni, ^{64}Cu, ^{20}F and ^{187}Re [81]-[90].

In heavy neutrino investigation it is useful to assume that the electron neutrino ν_e is predominately a linear combination of two mass eigenstates ν_L and ν_H of masses m_L and m_H, where L and H stand for light and heavy respectively.

$$\nu_e = \nu_L \cos(\theta) + \nu_H \sin(\theta) \tag{3.1}$$

with $m_L \ll m_H$ and θ is the mixing angle.

Then the β spectrum expressed by (1.22) can be rewritten as

$$N(E, m_L, m_H, \theta) = N(E, m_L)\cos^2(\theta) + N(E, m_H)\sin^2(\theta) \tag{3.2}$$

with the mixing angle θ as an additional fitting parameter. The emission of heavy neutrino would manifest as a kink in the spectrum at energy $Q - m_H$ for heavy neutrinos with masses between 0 and $Q - E_{th}$, where E_{th} is the experimental energy threshold. Figure 3.1 shows the effect of the existence of a sterile heavy neutrino with $m_H = 1.5$ keV mixed with a massless light neutrino on the shape of beta spectrum for different values of $\sin^2\theta$.

3.3 Heavy neutrinos and MARE

To evaluate the capability of the MARE experiment to measure the mass of heavy neutrinos from some tens of eV to 2.5 keV, the Montecarlo code used in the chapter 2 has been modified. Also in this case the approach has been to simulate many beta spectra, characterized by the same experimental configuration, and to analyse them as the real ones. The steps which lead to the statistical sensitivity to the emission of heavy neutrinos with mass m_H are:

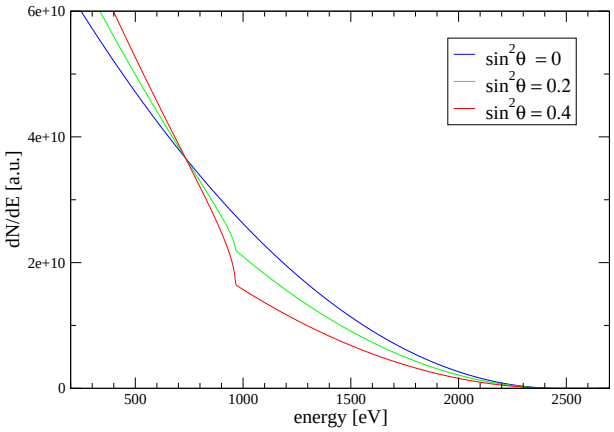

Figure 3.1: Effect of the existence of an heavy neutrino with $m_H = 1.5$ keV on the shape of beta spectrum for different values of $\sin^2\theta$ (i.e 0, 0.2 and 0.4). Montecarlo simulations with $N_{ev} = 10^{14}$, $\Delta E_{FWHM} = 5$ eV and $f_{pp} = 10^{-5}$.

– Evaluation of the theoretical spectrum $S'(E)$ which is expected to be measured by the virtual experiments

$$S'(E) = [N_{ev}(N(E, m_L, m_H, \theta) + f_{pp} N_\beta(E, 0) \otimes N_\beta(E, 0)) + b(E)] \otimes R(E) \quad (3.3)$$

where $N(E, m_L, m_H, \theta)$ is the rhenium beta spectrum normalized to unity given by (3.2), $b(E)$ is the background energy spectrum and $R(E)$ is the detector energy response function. The $b(E)$ function is usually taken as a constant, while the response function $R(E)$ is assumed to be a symmetric Gaussian.

– The simulated spectra are numerically generated by letting the spectrum $S'(E)$ fluctuate according to a Poisson statistics. The simulated experimental spectra are generated on an energy interval which is smaller than the full $0 - 2E_0$ interval.

– Each simulated spectrum is fitted using (3.3) and leaving $\sin^2\theta$, E_0, N_{ev}, f_{pp} and b as free parameters. The fit is restricted to an energy interval smaller than the one used for the simulated spectrum generation. The mass of the light neutrino has been set equal to zero.

– The limit on $\sin^2\theta$ is quoted using the definition of sensitivity given by Feldman e Cousins in [91].

In practice, two different experimental configuration for different possible values of m_H (from 20 eV to 2000 eV) have been simulated:

– MARE-1 in Milan with a statistics of $N_{ev} = 10^{10}$, a fraction of unresolved pile up events $f_{pp} = 10^{-4}$, an energy resolution of ΔE_{FWHM}=30 eV and background $b = 0$.

– a possibile configuration of a MARE-2 experiment with $N_{ev} = 10^{14}$, $f_{pp} = 10^{-5}$, ΔE_{FWHM}=1 eV and $b = 0$.

For both experimental configurations 300 beta spectra have been created for each m_H and then they have been analysed. Figure 3.2 shows the exclusion plot for the two simulated configurations.

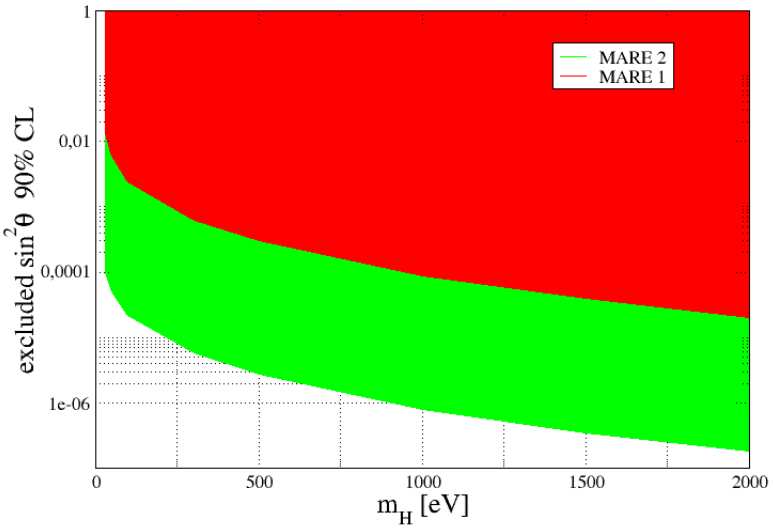

Figure 3.2: Upper limits at 90% CL on the mixing angle between a heavy neutrino and a massless one as a function of the heavy neutrino mass in the range 20-2000 eV. The filled areas are excluded at 90% CL. The comparison is between the MARE-1 configuration and one possible MARE-2 configuration.

The search for heavy neutrinos could be affected by systematics uncertanties due to the background and to the ripple observed in ^{187}Re spectrum and caused by BEFS.

3.4 Haevy Neutrinos and Mibeta

The Mibeta experiment was running between the years 2002 and 2003 using an array of 8 detectors made with silver perrhenate ($AgReO_4$) crystals glued to doped silicon thermistors. The total mass of the array was 2.17 mg, corresponding to a ^{187}Re activity of $\sim$ 1.2 Hz. The average energy resolution was 28.5 eV FWHM at the ^{187}Re endpoint, and the

average rise time 490 μs. In 0.6 years of live time Mibeta collected 6.2×10^6 ^{187}Re decays above the 700 eV common energy threshold [27].

To investigate the existence of an heavy neutrino mixed with a light one the experimental beta spectrum acquired by Mibeta has been analysed. In this case, the spectrum has been fitted using (3.3). It has been assumed that the light neutrino is massless ($m_L = 0$). The free parameters of the fit function are E_0, N_{ev}, f_{pp}, b and $\sin^2\theta$.

The upper limit on $\sin^2\theta$ is quoted using the unified approach proposed by Fieldman and Cousins [91] and accepted by the Particle Data Group [92]. No evidence of a heavy neutrino mass in the range 10-1500 eV has been found and the upper limits at 95% CL of the $\sin^2\theta$ as a function of m_H are plotted in figure 3.3.

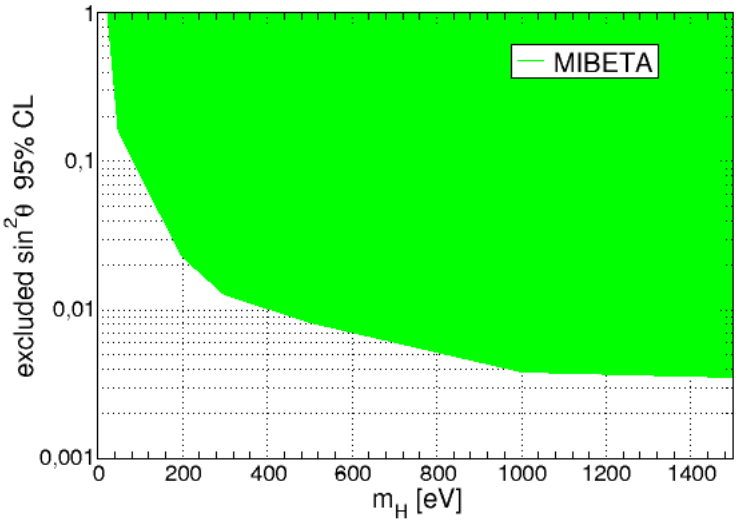

Figure 3.3: Upper limit at 95% CL on the mixing angle of an heavy neutrino ν_H with a mass in the range 10-1500 eV with a massless neutrino ν_L given by the Mibeta experiment. The filled area is excluded at 95% CL.

Chapter 4

Thermal Detectors

Thermal detectors are a wide set of phonon-mediated detectors. These detectors have a number of characteristics that make them more attractive than ionization detectors for many applications. One of them is tightly related to the lack of a requirement for efficient charge transport. This also allows a wide choice of different materials, so that the source may be used as detector. If it is not necessary to collect electrons, then large amounts of impurities can be tolerated and a radioactivity source could be embedded within the detector.

Thermal detectors were proposed initially as perfect calorimeters with a heat capacity C, i.e. as devices able to thermalize thoroughly the energy released by the impinging particle. In this approach, the energy deposited determinates an increase of temperature T. This temperature variation corresponds to the ratio between the energy E released by the impinging particle and the heat capacity C. The only requirements are to operate the devices at low temperature in order to make the heat capacity low enough, and to have a sensitive enough thermometer coupled to the absorber. At low temperatures they provide better energy resolution, lower energy thresholds and wider material choice than conventional detectors in many applications. The term *microcalorimeters* is used when the detector total mass does not exceed 1 mg and the linear dimensions are a few hundreds of μm maximum.

Low temperature detectors are widely used in single and double beta decay experiments, in cosmological dark matter searches, in X-ray detection of galactic and extragalactic objects as well as in cosmic background radiation experiments.

4.1 Basic Theory of Calorimeters

A simple calorimeter or bolometer can be essentially sketched as a three component object. As shown in Fig. 4.1 these are: 1) an absorber, where the interacting particles deposit their energy, 2) a perfectly coupled thermometer, which measures the temperature rise,

and 3) a weak thermal link to a heat sink that returns the absorber temperature to some defined value in the absence of any signal. The absorber can be characterized by its heat capacity C, the thermal link by its conductivity G and the heat sink by its temperature T_0.

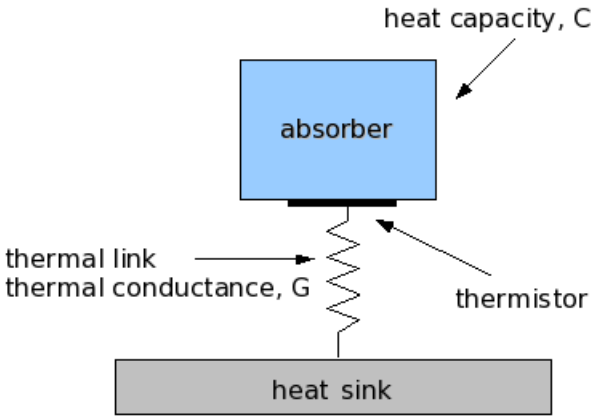

Figure 4.1: A simple sketched of a thermal microcalorimeter.

Thermal detectors can be classified into two big families:

- ***Monolithic detectors:*** the absorber and the sensor are the same object.
- ***Composite detectors:*** the absorber and the sensor are two different objects.

A peculiarity of thermal detectors at low temperature is the possibility to achieve better energy resolution than conventional ones. In a typical ionization detector the charge channel gets only about 30% of the event energy, and the statistical fluctuations in this fraction produce a fundamental constraint, or Fano limit, on resolution:

$$\Delta E_{FWHM} = 2.35F\sqrt{\epsilon E} \tag{4.1}$$

where F is the Fano factor which quantifies the departure of the observed statistical fluctuations in the number of charge carries from pure Poisson statistics [93], ϵ is the energy for a pair generation and E is the deposited energy. For silicon, the energy resolution is about 120 eV FWHM (full width at half maximum) at 6 keV.

In thermal detectors the limit on energy resolution comes from the random exchange of energy between the absorber and the heat sink through the finite thermal link. It is an elementary result of classical statistical mechanics that the magnitude of resulting fluctuations in the energy content of the calorimeter is given by:

$$\Delta E = \sqrt{k_B C(T_b) T_b^2} \tag{4.2}$$

ΔE is independent of the conductance of the link and of the energy of the impinging particle. If the energy carriers in the calorimeter have a mean energy $k_B T$, this can be thought as Poisson fluctuations in their number.

An adimensional factor α has to be introduced as multiplier for eq. (4.2) in order to take into account the effects due to the thermal contact, the sensor and the temperature dependence of C.

In microcalorimeters operating at 100 mK, the mean energy of one phonon is about 10 μeV and the statistical fluctuations limit the energy resolution around 1 eV or less.

4.2 Thermalization Process

Interacting with the detector a particle releases its energy into the absorber in the form of ionization and/or excitations. The deposited energy is downgraded via interactions with the nuclear and the electronic systems into out of equilibrium phonons. This initial population successively decays via different processes in an equilibrium Bose-Einstein distribution of thermal phonons.

In dielectrics and semiconductors the energy is downgraded through the electronic channel. The incoming particle is slowed down after the interaction into the absorber. Along its track it produces many electron-hole pairs. This pairs, having at the beginning high spatial density and energy, interact with each other and with the lattice impurities producing phonons. In this processes a large fraction of the initial energy is transferred to the lattice as vibrational phonons but also other processes could occur. Indeed, a fraction of this energy can leave the crystal or can be stored in stable or metastable states. Three are the possible recombinations modes:

- **radiative recombinations** of e-h pairs with the escape of the emitted photons.
- **non-radiative recombinations** which take too much time compared to the signal development
- **trapping** of electrons and holes in the states created by an impurity defects in the lattice

The detector is blind to these undesirable processes.

In order to understand the phonon thermalization processes it is useful to consider the mono-dimensional representation of the phonon dispersion curves (fig. 4.3).

These curves describe the allowed energy states of phonons. The upper curve traces the optical branch of the phonon dispersion and the lower curve represents the acoustic branch.

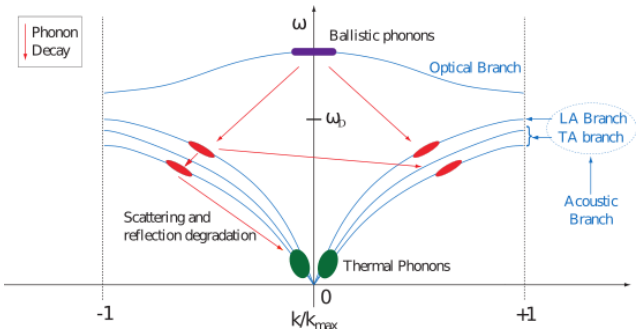

Figure 4.2: A mono-dimensional thermal model for the phonons thermalization.

The optical branch has a constant behaviour, while the acoustic branch is characterized by a photon-like linear dispersion at low energy. The phonons, generated as a result of one interaction, are produced with high probability in the optical branch. Optical phonons decay in the longitudinal acoustic branch (LA) at lower frequencies in a very short time (10÷100 ps). The energy and momentum are conserved and so the decay produces two phonons, each having half of the energy of the initial particle ($E \sim \hbar\omega_D$ where $\omega_D = 2\pi\nu_D$ and ν_D is the Debye cutoff frequency of the crystal) and opposite momentum. This energy is higher than the average energy of the thermal phonons at the bolometric working temperature, which is of the order of μeV. So that new phenomena of phonon energy degradation can occur: an-harmonic decay of the only longitudinal acoustic phonons, dominating until 10 meV, the isotopic scattering, which allows also the conversion from the longitudinal acoustic mode into the transverse acoustic mode, and the scattering on impurities. The conversion towards lower energies becomes a slower and slower process.

After a certain number of decays the mean free path of the phonons becomes larger than crystal dimensions. In pure crystal this means that phonons propagate ballistically until they reach the crystal surface. Phonons that are not absorbed by sensor will be reflected by surfaces and therefore they can undergo other decays processes leading to a complete thermalization.

Since ballistic and thermal phonons have separated development times, two kind of phonon sensor have been developed:

- **ballistic phonon sensors** detect athermal phonons at their first interaction with the crystal surface interface. They are used for spatial event reconstruction.
- **thermal phonon sensors** detect thermalized phonons. A fast and complete ther-

malization of the phonons is assumed.

4.3 Energy Absorber

One of the most important parameters of the detector is its heat capacity, which needs to be kept as small as possible in order to have measurable temperature variations. To fulfil this requirement, low temperatures are needed.

At low temperatures the specific heat of a pure crystal is the sum of two different contributes:

$$c(T) = c_r(T) + c_e(T) \tag{4.3}$$

where c_r and c_e, respectively, represent the lattice and the electron contributions.

For dielectric and diamagnetic crystals the principal contribution to the heat capacity is due to the lattice. This contribution can be expressed referring to the Debye Model in the low temperature approximation:

$$c_r(t) = \frac{12}{5}\pi^4 k_B N_A \left(\frac{T}{\Theta_D}\right)^3 T \ll \Theta_D \tag{4.4}$$

where k_B, N_A e Θ_D are, respectively, the Boltzmann constant, the Avogadro number and the Debye temperature, a parameter characteristic of the material.

The corresponding heat capacity can be written as:

$$C_r(t) = \beta \frac{m}{M} \left(\frac{T}{\Theta_D}\right)^3 T \ll \Theta_D \tag{4.5}$$

where $\beta = 1944\ \mathrm{J} \cdot \mathrm{K}^{-1} \cdot \mathrm{mol}^{-1}$, m is the absorber mass and M is the molecular weight.

The electronic contribution c_e depends on the conductive or superconductive nature of the material.

Besides the lattice vibration, in a metal there are conduction electrons, which can be thermally excited and can be treated as an ideal gas. Taking into account the Fermi-Dirac distribution at finite temperature, the specific heat is given by:

$$c_e(T) = \frac{\pi^2}{\Theta_D} Z R \frac{T}{\Theta_F} \tag{4.6}$$

where Z, R, Θ_F are, respectively, the number of electrons in the conduction band for each atom, the gas constant and the Fermi temperature. If a metal is in a superconductive state, then the electric contribution to the specific heat at T below the critical temperature T_c is:

$$c_e(T) = K_s e^{-2\frac{T_c}{T}} \tag{4.7}$$

where K_s is a constant depending on the material characteristics. For $T \ll T_c$ this contribution become negligible with respect to the lattice one.

The best choice for absorbers are dielectric and diamagnetic materials with high Debye temperature. For that materials the heat capacity is described by 4.5. Another good choice are superconductive materials with T_c well above the working temperature.

The absorber dimension usually depends on the application of the Low Temperature Detector (LTD). The size range from hundred of micrograms [96], in case of X-ray spectroscopy and single beta decay, to kilograms in case of Gamma-ray spectroscopy, Double Beta Decay and Dark Matter researches [97].

4.4 Phonon sensor

The phonon sensor is a device able to collect phonons produced in the absorber. Some phonon sensors are sensitive to quasi-ballistic phonons, therefore the detectors with these sensors are not ideal calorimeters. Thermal detectors operated in a non-equilibrium mode can be fast relative to equilibrium ones, since thermal equilibrium often takes a very long time to establish at low temperatures. With these detectors it is possible to obtain a good spatial resolution, but their energy resolution is not so good.

Other phonon sensors are able to collect only thermal phonons converting them in an electrical signal. The detectors using this kind of phonon sensors are known as equilibrium detectors and they in principle offer the ultimate in energy resolution. In this case the phonon sensor is usually a resistive element with a heavy dependence of the resistance on the temperature, so that a little variation of temperature can generate a significant and measurable variation of resistance. It can be either a semiconductor thermistor or a superconducting film kept at the transition edge, named usually transition edge sensors (TES). Semiconductor thermistors and TESs are usually characterized by their logarithmic sensitivity A, which describes the sensor capability of transforming a small temperature increase in a significant resistivity variation. This parameter is defined as:

$$A = \left| \frac{d \log R(T))}{d \log T} \right| \tag{4.8}$$

The value of the sensitivity usually spans from 1 to 10 for semiconductor thermistors and from 10^2 to 10^3 for TESs.

There are other sensors sensitive to thermal phonons, like the magnetic thermometers. With these latest devices it is possible to register a temperature change through a magnetization change.

4.4.1 Semiconductor Thermistors

As semiconductor thermistors are intrinsically slow due to the electron-phonon decoupling which will be described later, they are mainly sensitive to thermal phonons. In this context, they give information about the system in thermal equilibrium, and they could be thought as temperature sensors. These devices consist of Ge or Si small crystals with a particular doping density in order to have a strong dependence of the sensor resistance on the temperature. Semiconductor thermistors can be also realized in an amorphous film form, like NbSi.

At the absolute zero the valence band of a pure semiconductor is completely full and the conduction band is completely empty. The energy gap between the two bands is no more than 2 eV. For silicon this gap is 1.14 eV and for germanium it is 0.67 eV. So, for intrinsic semiconductors, i.e. for a semiconductor without impurities, the conduction can happen only with an activation energy equal or larger than the energy gap. This mechanism is possible if the working temperature is above the room temperature (i.e. $k_B T_r \simeq 0.025$ eV).

Adding impurities in the semiconductor lattice (doped semiconductors) the electronic conduction at lower temperature is also possible. In fact, the impurities introduce discrete levels slightly above the top of the valence band or under the bottom of the conduction band, depending on the type of the dopant atom. The basic properties of such systems were determined by Anderson [94] and Mott [95]. They found that there is a critical doping density (N_c) below which the conductivity goes to zero at zero temperature, and above which there is always a finite conductivity. The region near this concentration is called metal-insulator transition region (MIT). To be sensitive thermometers, semiconductor must be doped below this metal-insulation transition, where charge transport takes place by phonon-assisted tunneling between impurity sites. The energy levels of these sites are randomized by the long-range coulomb potential of charges distributed over distant sites, and the energy difference required in a given tunneling event is made up by absorption or emission of phonons of required energy.

At temperature lower than 10 K the charge carriers, located in the impurity sites, jump from a donor site to an other without using the conduction band. The tunneling event takes place to the nearest unoccupied site. This is referred to as *Nearest Neighbour Hopping*. This mechanism, which is represented schematically in Fig. 4.3, is due to quantum-mechanical tunneling through the potential barrier that separates the two dopant sites.

At $T \ll 10$ K, the scarcity of high energy phonons favours longer tunneling events as necessary to find an unoccupied site sufficiently close to the same energy. In this regime, named *Variable Range hopping - VRH*, the compensation level $K = N_A/N_D$, where N_A and N_D are the acceptor and donor concentrations respectively, plays a fundamental role

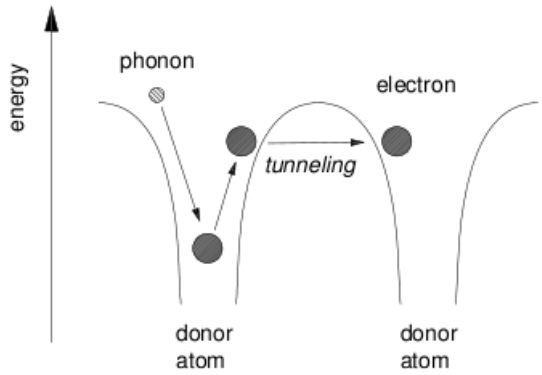

Figure 4.3: Sketch of the hopping conduction mechanism.

in the VRH process, as it determines the density of states near the Fermi energy and so the possibility of charge carriers to jump to other sites. This is usually the regime of interest for low temperature thermometers. In this regime the resistivity is expected to behave as:

$$\rho = \rho_0 e^{\left(\frac{T_0}{T}\right)^{\gamma}} \tag{4.9}$$

where ρ_0 and T_0 are parameters depending on the doping and compensation levels. Increasing the doping the value of T_0 decreases according to [99]:

$$T_0 \propto \left(1 - \frac{N}{N_c}\right)^{1.7} \tag{4.10}$$

The rise of the compensation level leads to an increasing of T_0. In the Mott Model the exponent γ is equal to 1/4 for a three-dimensional system and for low compensation levels. For larger values of K, the Coulomb repulsion among the electrons leads to the formation of a parabolic gap (Coulomb gap) in the electron state density near the Fermi energy. In fact the density of states ($g(E)$) is given by:

$$g(E) \propto (E - E_F)^2 \tag{4.11}$$

This modifies the result to make $\gamma = 1/2$. Data from samples doped by nuclear transmutation (NTD) or by ion implantation do show the expected behaviour. One example can be seen in Fig. 4.4 [98], where the $T^{-1/2}$ behaviour predicted by VRH with Coulomb gap is quite accurately followed over several orders of magnitude in resistance.

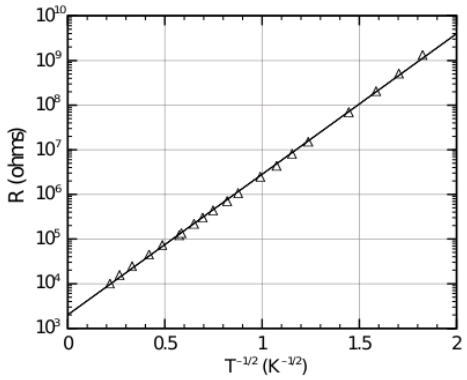

Figure 4.4: Measured $R(T)$ for ion-implanted silicon [98]. The linear dependence of $\log(R)$ on $T^{-1/2}$ predicted by VRH a with Coulomb gap is observed over several orders of magnitude in resistance.

Deviation from Coulomb gap behaviour

At sufficiently low temperature, $T_0/T >\sim 24$, systematic deviation from this Coulomb gap behaviour are observed [100, 101]. Observing a similar behaviour in arsenic-doped germanium, Shlimak suggested that a magnetic hard gap due to spin-spin interactions may be responsible [102]. Applied a magnetic field > 1T, the $R(T)$ reverts to Coulomb gap behaviour. This evidence supports the idea that the deviations are some kind of magnetic effect [103].

From an experimental standpoint, this deviation can easily be masked by light leaks, RF pickup, or other extraneous heating effects. All of them tend to make the measurements turn down below the intrinsic $R(T)$ curve. It is useful to have an analytic expression to fit data at higher temperature, where these effects are negligible. In fact comparing extrapolated data to the lowest temperature measurements it is possible to determine the extent of any heating problem.

Doping and device fabrication

There are several methods to produce thermistors characterized by an uniform dopant distribution. The most common techniques are the neutron transmutation doping (NTD) for germanium thermistors and ion implantation for silicon ones.

– **Neutron transmutation doped germanium:** Extremely reproducible thermometers can be produced by irradiating germanium with reactor neutrons [104]. Natural germanium has four stable isotopes. The neutron capture on two of these isotopes

produces gallium-doped (p-type) material that is 32% compensated with arsenic. Since the isotopes are chemically identical, they are perfectly randomly distributed in the lattice, and the neutron cross section makes the neutron flux uniform throughout even quite large blocks of material. Then these blocks can be cut to make large numbers of very uniform thermometers. So the uniformity and predictability of NTD Ge thermometers is valuable in the construction of large arrays of detectors. But the penetrating power of the neutrons also means that it is practical impossible to mask the process and dope only one selected area in the crystals. Therefore the thermometers must be cut in the optimum dimensions, and then individually attached to the absorber. This is not a drawback when the elements are very large and individually mounted as in the CUORE project [105].

– **Ion-implanted silicon** Silicon requires very large neutron doses to dope by transmutation, and so this technique is not used. However, doping by implanting ions from beam with a kinetic energy from tens of keV to a few MeV is a well-developed technique in the semiconductor electronics industry. This allows penetration of up to $\sim 1\mu$m, but results in an approximately Gaussian density profile with depth. It is possible to obtain uniform densities: 1) superimposing implants with several different energies and carefully designed doses to produce a flat-top profile; 2)implanting a single dose of each ion into a thin piece of silicon and then treating it at high temperature to allow the implanted ions to diffuse completely and uniformly throughout the thickness.

  The great advantages of this doping method is that it can be masked by standard photolitographic techniques, allowing the simultaneous fabrication of small thermistors with fully integrated electrical connections [106, 107]. Silicon has also excellent mechanical end thermal properties.

  Ion implanted thermistors have been plagued by a lack of reproducibility that is not understood. Both doses and energies can be measured with high accuracy, but the run-to-run repeatability is poor enough. So it is common to implant a series of wafers with slightly different doses, and then pick up the one that comes closest to the desired resistivity. Fortunately, the uniformity across a wafer is good.

4.4.2 Electrical nonlinearities

Doped semiconductors should be ideal thermometers. The logarithmic sensitivity (4.8) is just:

$$A = \left| \frac{d \log R(T))}{d \log T} \right| = \gamma \left(\frac{T_0}{T} \right)^{\gamma} \tag{4.12}$$

for Coulomb gap $R(T)$. One can make T_0 arbitrarily high by lightly doping, so it should be possible to make A as large as desired. It is also possible to produce ion-implanted sensors with such small volumes that the heat capacity contribution of the thermometer is negligible despite of the high specific heat of the doped materials.

However, the effects presented below introduce limits to the thermistor size and sensitivity. None of them is entirely understood theoretically, but empirical data are available. For a given application optimum values for thermistor size and T_0 are determined by these data. These effects also introduce intrinsic limits on the speed of semiconductor thermistors.

Electric field effects

Phonon-assisted tunneling is an inherently non-linear process, and it is expected to be linear only in the limit of small electric fields. The field effect is responsible for:

$$R(T, E) = R(T, 0)e^{-CeE\lambda/kT} \tag{4.13}$$

where E is the electric field, $R(T, 0)$ is the resistance in the limit of low fields - the coulomb gap function in this case - C is a constant of order unity, λ is the characteristic hopping length that in the most cases scales as $T^{-1/2}$ and e is the electronic charge. This hopping effect is observed in germanium and silicon thermistors under certain conditions [108, 109, 110].

This behaviour is represented by a local slope evaluated at the operating point and acts to reduce thermometer sensitivity. Raising T_0 by decreasing the doping concentration makes λ larger and increases the magnitude of this term. In the limit of a strong electric field the resistance becomes independent from temperature.

“Hot Electron ” effects

The electric field effect given by (4.13) does not always describe the observed behaviour very well. A new empiric model, in which the decoupling between the electronic system and the phononic one is hypothesized, has been proposed in order to explain the experimental data. This model is known as “ hot-electron model ” [111]. If the thermistor polarization power, known also as bias power, is dissipated in the conduction electron system and then transfered to the crystal lattice, one can envision an effective thermal conductivity G_{ep} between the electrons and phonons.

In the hot-electron model there are two different temperatures: the electrons temperature T_e and the lattice one T_l. The temperature dependence of G_{ep} is given by:

$$G_{ep}(T_e) = \frac{dP_e}{dT_e} = \alpha g_{ep} T_e^{\alpha-1} \tag{4.14}$$

where α and g_{ep} are constants and P_e is the dissipated power in the thermistor for its polarization. In addition, G_{ep} is proportional to the thermistor volume. Then T_e will be higher than T_l according to:

$$T_e = \left(T_l^{\alpha} + \frac{P_e}{g_{ep}} \right)^{\frac{1}{\alpha}} \tag{4.15}$$

As a result, the VRH theory is modified so that the resistance is no longer dependent on lattice temperature but on T_e . Then the equation (4.9) becomes:

$$\rho(T_e) = \rho_0 e^{\left(\frac{T_0}{T_e}\right)^{1/2}} \tag{4.16}$$

Since the sensor resistance depends on the electronic temperature T_e, the electron-phonon decoupling leads to a loss of sensitivity in the evaluation of the lattice temperature T_l. In addition, this decoupling causes a decrease in sensitivity even more evident when the electronic temperature is lower and the dissipated power P_e on the electronic system is higher. Using equations (4.14) and (4.16) the logarithmic sensitivity is just:

$$A(T_e, P_e) = \left| \frac{d \log R(T_e))}{d \log T_l(T_e)} \right| = \gamma \left(\frac{T_0}{T_e} \right)^{\gamma} \left(1 - \frac{P_e}{g_{ep} T_e^{\alpha}} \right) \tag{4.17}$$

and including (4.15) becomes:

$$A(T_e, P_e) = \left| \frac{d \log R(T_e))}{d \log T_l(T_e)} \right| = \gamma \left(\frac{T_0}{T_l} \right)^{\gamma} \left(1 + \frac{P_e}{g_{ep} T_l^{\alpha}} \right)^{\frac{1-\alpha-\gamma}{\alpha}} \tag{4.18}$$

– **Time constants and heat capacity.**

The hot electron effect has a consequences that go beyond a particular $R(T, E)$ relationship. Since the electron system should be characterized by some heat capacity C_e and considering the electron-phonon thermal conductivity G_{ep} introduced just above, then there should be a characteristic time $\tau = C_e/G_{ep}$ for changes in the electron temperature T_e. This has been investigated both for NTD Ge [112, 113] and for ion implanted thermistors [114].

Figure 4.5 shows G_{ep}, τ and their product C_e as a function of the electron temperature. G_{ep} and τ are measured with two independent approaches.

Remarkably, while the independently-measured G_{ep} and τ both vary almost of three orders of magnitude over this temperature range, their product is almost constant. The electronic heat capacity is considerably flatter than linear temperature dependence expected for a metallic system. It is almost constant below 0.1 K and then steepens at higher temperature. The flat temperature dependence was predicted and it is ascribed to the formation of spin-exchange clusters [115].

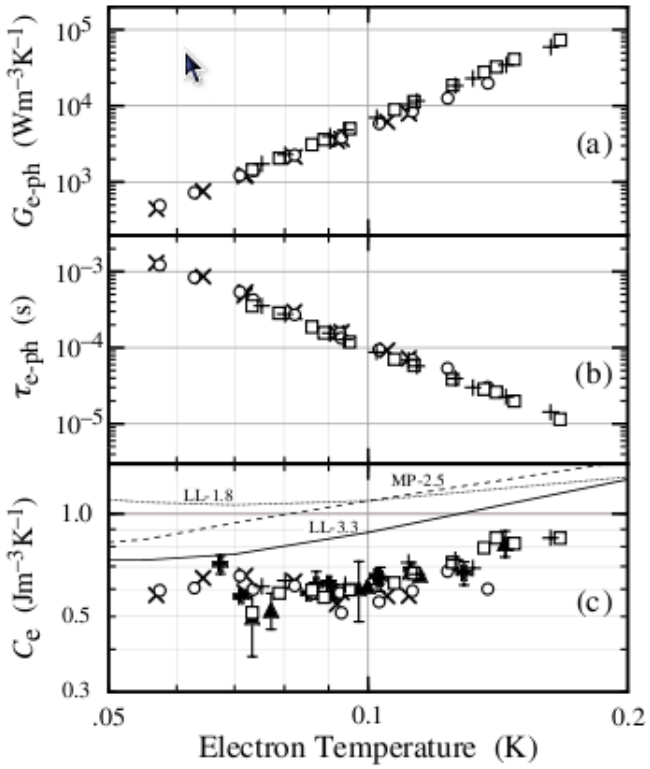

Figure 4.5: a) Coupling constant G_{ep} as a function of T_e determined from D:C resistence as a function of the bias power. b) Characteristic time constant τ determined from A.C impedance measurements c) Electron heat capacity $C_e = G_{ep}\tau$ opened symbols. Picture from [98]

– **Internal thermodynamics fluctuation noise**
Another consequence of the hot-electron model is that additional noise should be introduced in the thermometer output due to temperature fluctuations of the electronic system caused by a random energy transport between the electron and phonon systems. This means that when a doped semiconductor thermistor is used in a bolometric or a calorimetric structure with a separate absorber and thermal isolation link, the effective thermal circuit must include at least two thermal links and two heat capacity when we will see later (see section 4.6).

4.5 Thermistor characterization

The sensor converts thermal pulses into electrical signals. It is possible to connect the voltage across the thermistor to the lattice temperature T_l if the thermistor is polarized by a constant current. The circuit used to do that is shown in figure 4.6.

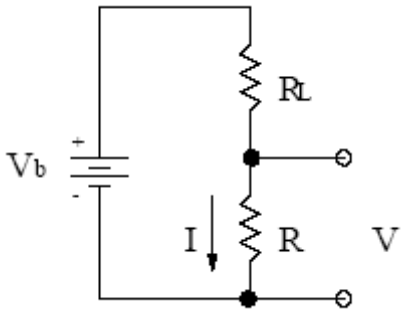

Figure 4.6: Biasing circuit for a silicon thermistor

The biasing source consists of a voltage supply and a load resistance (R_L) in series with the thermistor (R). The value of the load resistance is chosen to be much grater than the resistance of the thermistor at the working temperature so that an approximately constant current $I = V_{bias}/(R_L + R) \sim V_{bias}/R_L$ flows through the thermistor. The voltage across the thermistor is proportional to the thermistor resistance.

The thermistor characterization consist in linking its static properties to the lattice temperature T_l of the silicon substrate. For that reason, the thermal coupling between the lattice and the heat-sink, which is at the well known temperature T_s, is maximized so that it is possible to assume T_s and T_l coincident regardless of the dissipated power. The logarithmic sensitivity A is an important parameter in the thermistor characterization.

Using its definition, the ratio between the maximum voltage signal ΔV and the voltage across the thermistor V is given by:

$$\frac{\Delta V}{\Delta T} = \frac{AV}{T} \tag{4.19}$$

where ΔT is the maximum temperature signal. In presence of non-linear behaviours the thermistor temperature depends on the bias voltage even if the T_l remains constant. Therefore to correctly determine the thermistor parameters like ρ_0, T_0 and γ it is not enough to measure the resistance with the temperature. So a more complex analysis based on non-linearity model must be preferred. These non-homic behaviours are identified and characterized through the study of load curves at different T_l temperatures. A load curve is the $I - V$ relationship. A typical behaviour of one load curve for a real thermistor is shown in figure 4.7.

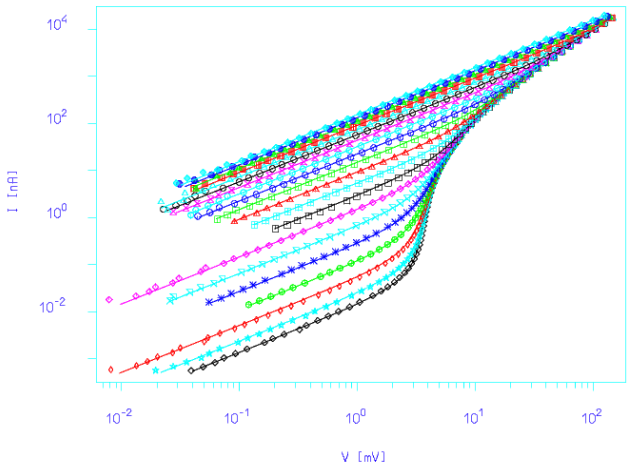

Figure 4.7: A load curve for the XRS2 array, *wafer*3.

In conclusion the thermistor characterization is based on a set of load curves at different base temperatures T_l. The base temperature spans from about few mK to about 1 K (for example, in the case of the MARE-1 thermistor it spans from 50 mK to 1 K). Each load curve is composed by several $I - V$ pairs.

Studing the load curves it is possible to determine g_{ep} and α parameters of the equation (4.14) for the "hot-electron" model. A first simple approach is to calculate the γ, T_0, and ρ parameters interpolating the resistance values, obtained by extrapolating the load curves

in the limit where the bias goes to zero. Then the $I-V$ pairs are transformed into $P_e - T_e$ pairs by:

$$\begin{cases} P_e = IV \\ T_e = T_0 \left[\log \left(\frac{V/I}{R_0} \right) \right]^{-1/\gamma} \end{cases} \tag{4.20}$$

The G_{ep} curves are obtained by numerical differentiation of $P_e(T_e)$ curves. Since the dissipated power P_e on the electronic system could be due not only to the bias voltage but also to the electromagnetic interferences, it not so easy to determine the correct values for γ, T_0, and ρ with the previous model. Therefore, it is used a new procedure which interpolates the load curves with the new relations:

$$\begin{cases} R(T_e) = R_0 \exp[(T_0/T_e)^{\gamma}] \\ P_e^{tot} = P_e + P_e^{bkg} = g_{ep}(T_e^{\alpha} - T_l^{\alpha}) \end{cases} \tag{4.21}$$

where $R = I/V$, $P_e = VI$ and γ, T_0, ρ, g_{ep}, γ, and P_e^{bkg} are free parameters. P_e^{bkg} is the background power, i.e. any additional contribute to the total power as the electromagnetic interferences.

4.6 Microcalorimeter Thermal Model

As said in the previous sections a microcalorimeter is composed by an absorber or thermal mass where the interacting particles deposit their energy, a perfectly coupled thermometer that measures the temperature increase of the absorber, and a weak thermal link to a heat sink that returns the absorber temperature to a defined value in the absence of a signal.

In this section thermal models for monolithic and composite microcalorimeter are presented.

4.6.1 Thermal model for a monolithic microcalorimeter.

A monolithic microcalorimeter is just composed by a small silicon substrate where the thermistor is implanted. It could be sketched by a thermal capacity C linked to a heat sink at a defined temperature T_s trough a finite conductance G_{ls}, as shown in figure 4.8.

The heat capacity includes all the contributions of the detector elements: the lattice capacity of the absorber and the electron capacity of the sensor. The finite conductance G_{ls} is the electrothermal connection between the detector and the heat sink. Thanks to it a variation of energy causes an observable variation of the lattice temperature T_l. The finite conductance is expected to behave as:

$$G_{ls} = \beta g_{ls} T^{\beta - 1} \tag{4.22}$$

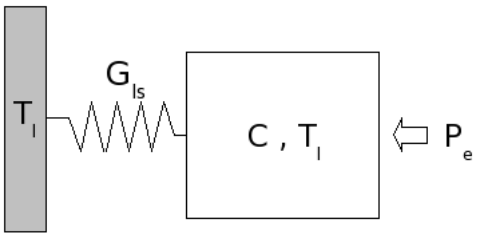

Figure 4.8: A simplified sketch of a monolithic microcalorimeter with only one stage.

where β is equal to 2 for metals and 4 for insulators, g_{ls} is a constant.

For a given absorber with temperature $T_l(t)$ at the time t one can assume that:

$$\Delta T = |T_l(t) - T_s| \ll T_s \ \forall t \tag{4.23}$$

so that C and G could be treated as constants.

To describe a microcalorimeter it is convenient to use its load curve at the temperature T_s described by:

$$\begin{cases} V/I = R(T_l) \\ VI + P^{bkg} = g_{ls}(T_l^{\beta} - T_s^{\beta}) \end{cases} \tag{4.24}$$

parametric in T_l.

The energy deposited by a single quantum breaks the thermal equilibrium and the time evolution of T_l is obtained resolving the differential equation which describes the dynamic of the system shown in figure (4.8). Moreover, in first approximation an ideal instantaneous deposition of energy in the absorber is considered. The dynamic of the system is described by:

$$C\frac{dT_l}{dt} + G_{ls}(T_l - T_l^0) = P(t) \tag{4.25}$$

whit $T_l^0 = T_l(t = 0)$. In the case of an instantaneous deposition of energy $P(t)$ is given by:

$$P(t) = \delta(t)\Delta E \tag{4.26}$$

Then the solution is:

$$T_l(t) = \frac{\Delta E}{C}e^{-t/\tau} + T_l^0 \qquad \tau = \frac{C}{G} \tag{4.27}$$

where τ is the decay time of the thermal signal. Therefore, the rise of temperature is followed by an exponential decay. One can easily see from equation (4.27) that the heat

capacity C is a crucial parameter for this device: the smaller is C and higher is the signal amplitude (i.e. $\Delta E/C$). For that reason the working temperature of such devices is below 100 mK. Only in these conditions sufficiently small heat capacities can be obtained.

In this naive description an instantaneous deposition of energy is considered, but this hypothesis is not so true. The thermalization process of high energy phonons is usually a rapid process but it sometimes happens on a time scale comparable to τ. In these conditions the time evolution of the decay of athermal phonons is an exponential with a time constant τ_{dec}. Then the equation (4.26) becomes:

$$P(t) = \frac{\Delta E}{\tau_{dec}} e^{-t/\tau_{dec}} \tag{4.28}$$

Using (4.28) the solution of (4.25) is a combination of two exponentials with time constants τ and τ_{dec}.

In this naive model the voltage response to an instantaneous deposition of energy is just:

$$\frac{\Delta V}{\Delta E} = \frac{AV}{TC} e^{-t/\tau} \tag{4.29}$$

obtained substituting (4.27) in (4.19). In the frequency domain it can be written as:

$$S(\omega) = \frac{AV}{TC} \frac{\tau}{1 + \jmath\omega\tau} = S(0) \frac{1}{1 + \jmath\omega\tau} \tag{4.30}$$

where $S(\omega)$ is the detector responsivity. The dissipative nature of the thermistor modifies the time evolution of the signal. In (4.25) the power term P_e does not appear because it is considered constant. But the Joule heating of the thermistor increases its temperature and decreases its resistance so that $P_e = I^2 R(T)$ could not be considered constant. This phenomena, known as "*electrothermal feedback*", leads to a more rapid going back to the equilibrium temperature T_s. Considering the electrothermal feedback equation (4.30) is expressed by:

$$S_e(\omega) = \frac{\Delta V(\omega)}{P(\omega)} = \frac{Z/R - 1}{2I} \frac{1}{1 + \jmath\omega\tau_e} = \frac{AV}{TG} \frac{1}{1 + \jmath\omega\tau_e} = S(0) \frac{1}{1 + \jmath\omega\tau_e} \tag{4.31}$$

with $Z = dV/dI$ is the dynamic impedance obtained by differentianting the load curve ($|Z| < R$ for a thermistor characterized by a negative A) and τ_e

$$\tau_e = \tau \frac{|Z| + R}{2R} < \tau \tag{4.32}$$

A real monolithic microcalorimeter is somewhat more elaborate than the naive description presented above. It is made of different systems: the electrons of the sensor and the lattice. Only the latest is in thermal contact with the heat sink through G_{ps}. An elementary scheme is reported in figure 4.9.

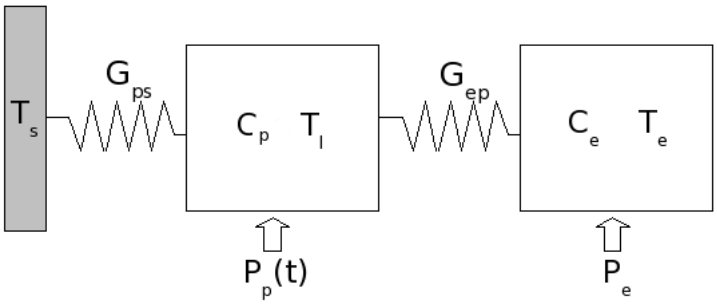

Figure 4.9: A simple sketched of a two-stages monolithic microcalorimeter.

In first approximation one can assume that the athermal phonons produced by impinging particles thermalize in the absorber before reaching the temperature sensor. In this way the power is dissipated only in the lattice system. Considering the electron temperature T_e and the lattice temperature T_l, a microcalorimeter is described by:

$$\begin{cases} V/I = R(T_e) \\ VI + P_e^{bkg} = g_{ep}(T_e^{\alpha} - T_l^{\alpha}) \\ VI + P_e^{bkg} + P_p^{bkg} = g_{ps}(T_l^{\beta} - T_s^{\beta}) \end{cases} \tag{4.33}$$

where P_e^{bkg} and P_p^{bkg} are the background power dissipated in the electron and lattice system, respectively. With the same simplifications of the previous analysis the dynamic of a microcalorimeter after an instantaneous deposition of energy could be expressed by:

$$\begin{cases} C_e \frac{dT_e}{dt} + G_{ep}(T_e^0 - T_p) \\ C_p \frac{dT_l}{dt} + G_{ps}(T_p - T_p^0) + G_{ep}(T_p - T_e) = P_p(t) \end{cases} \tag{4.34}$$

with T_e^0 and T_p^0 the initial conditions; C_p and C_e are the thermal lattice and electric capacity, respectively.

Then the general solution is a combination of two exponentials:

$$T_e(t) = \frac{EG_{ep}}{C_p C_e(1/\tau_2 - 1/\tau_1)}(e^{-t/\tau_1} - e^{-t/\tau_2}) + T_e^0 \tag{4.35}$$

In practice the microcalorimeters are built in such a way that $G_{ps} \ll G_{es}$, under this condition and with the hypothesis that $\tau_2 \ll \tau_1$, then the (4.35) becomes:

$$T_e(t) = \frac{E}{C_p + C_e}(e^{-t/\tau_1} - e^{-t/\tau_2}) + T_e^0 \tag{4.36}$$

where the time constants are given by:

$$\tau_1 \approx \frac{C_e + C_p}{G_{ps}} \qquad \tau_2 \approx \frac{C_e C_p}{(C_e + C_p)G_{ep}} \tag{4.37}$$

the electrothermal feedback must be introduced a posteriori. τ_1 is the detector decay time, while τ_2 is the detector rise time. As it can be seen by the expression of τ_2, the most fundamental limitation on the rise time is the electron-phonon coupling time in the thermometer.

But in reality the real pulses are characterized by three different time constants so that the expression (4.36) is not so precise, even if it is a good approximation.

When the radiation is directly absorbed in the silicon substrate the energy resolution is lower than the expected one. This phenomenon is due to the existence of metastable states inside the gap: the signal development times are such that the detector is blind to this energy. Therefore silicon is not a good absorber, instead materials with a lower gap like null-gap semiconductor and superconductors are good ones. For those materials the energy lost in metastable states is minimized. Another phenomenon, connected to the energy resolution degradation, is that a portion of energy thermalizes directly in the sensor. In this condition the detector response depends on the position in which the interaction takes place. In order to minimize these energy resolution degradations composite microcalorimeters are preferred.

4.6.2 Thermal model for a composite microcalorimeter

A model of a composite microcalorimeter is shown in figure (4.10). C_a is the absorber capacity. The thermal link G_{ap} between the lattice and the substrate in which the thermistor is implanted must be realized in such a way that the thermalization takes place only in the lattice.

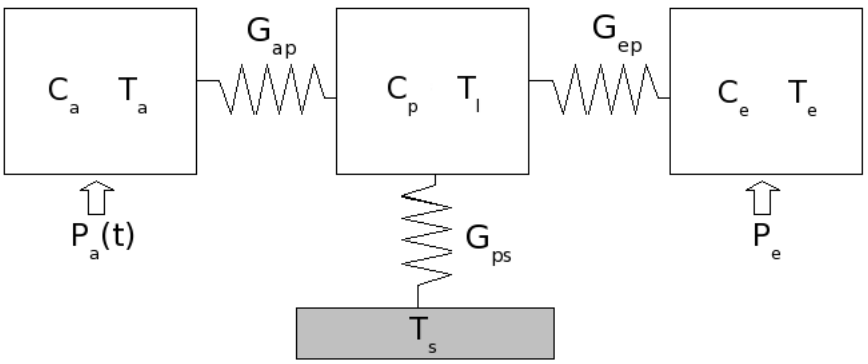

Figure 4.10: A simple sketched of a composite microcalorimeter.

Then at equilibrium the system can be described by:

$$\begin{cases} V/I = R(T_e) \\ VI + P_e^{bkg} = g_{ep}(T_e^{\alpha} - T_l^{\alpha}) \\ P_a^{bkg} = g_{ap}(T_a^{\eta} - T_l^{\eta}) \\ VI + P_e^{bkg} + P_p^{bkg} + P_a^{bkg} = g_{ps}(T_l^{\beta} - T_s^{\beta}) \end{cases} \tag{4.38}$$

with g_{ap} and η parameters. T_a and P_a^{bkg} are the absorber temperature and absorber background power, respectively. For a little temperature variation the dynamic of the system can be expressed by a system of differential equations:

$$\begin{cases} C_e \frac{dT_e}{dt} + G_{ep}(T_e - T_l) = 0 \\ C_p \frac{dT_l}{dt} + G_{ps}(T_l - T_l^0) + G_{ap}(T_l - T_a) + G_{pe}(T_l - T_e) = 0 \\ C_a \frac{dT_a}{dt} + G_{ap}(T_a - T_l) = P_a(t) \end{cases} \tag{4.39}$$

In the approximation of an instantaneous thermalization the solution of (4.39) is a combination of three exponentials. In practice if $G_{ep} \gg G_{ap} \gg G_{ps}$ the solution becomes a combination of only two exponentials:

$$T_l(t) \approx T_e(t) \approx T_e^0 + \frac{E}{C_a + (C_e + C_p)}(e^{-t/\tau_1} - e^{-t/\tau_2}) \tag{4.40}$$

where E is the total energy deposited in the absorber and the time constants could be written as:

$$\tau_1 \approx \frac{(C_e + C_p) + C_a}{G_{ps}} \qquad \tau_2 \approx \frac{C_a(C_e + C_p)}{(C_e + C_p + C_a)G_{ap}} \tag{4.41}$$

The time constant τ_1 is the ratio between the total heat capacity and the conductance G_{ps} and τ_2 is the rise time. The condition $\tau_2 \ll \tau_1$ is verified when $C_a \gg C_e + C_p$, and then the time constants becomes $\tau_2 \approx (C_e + C_p)/G_{ap}$ and $\tau_1 \approx C_a/G_{ps}$ with $G_{ap} \gg G_{ps}$.

4.7 Noise Sources

Different sources of noise limit the energy resolution of a bolometric detector. These sources can be classified in intrinsic and extrinsic noise. The intrinsic noise, dependent on the physical characteristics of the absorber and of the thermistor, is a unavoidable source of noise. It sets the lowest reachable theoretical limit for the energy resolution. So an accurate analysis is necessary. The extrinsic noise accounts for all the noise sources dependent on the experimental set-up. In this category are included the noise due to the cryogenic system, to the electronics read-out, to the electromagnetic interferences and to the mechanical microphonic noise.

The noise analysis is done assuming all the noise sources uncorrelated. So it is possible to separately study them and to assume the mutual influences negligible. The total power spectrum will be the sum in quadrature of all single components.

4.7.1 Intrinsic Noise

The intrinsic noise of one bolometer is constituted by the thermistor Johnson noise and by the thermodynamic fluctuation noise.

Thermometer Johnson Noise

This noise, also known as Nyquisit noise, is an irreducible source of noise in resistive thermistors. It can be modeled as a voltage source with spectral density

$$e_j(\omega) = \sqrt{4k_B T R} \tag{4.42}$$

in series with a noiseless resistance R. Being a thermal decoupling between the heat sink and the detector through a finite conductance, the effect of electrothermal feedback could not be negligible. Taking into account that one can demonstrate that the voltage noise is expressed by:

$$e'_j(\omega) = \sqrt{4k_B T R}\, \frac{|Z+R|}{2R} \frac{|1+j\omega\tau|}{|1+j\omega\tau_e|} \tag{4.43}$$

where R is the thermistor resistance, $Z = dV/dI$ is the dynamic impedance and τ_e is given by (4.32).

Thermodynamic Fluctuation Noise

This source of noise is a peculiarity of every device with heat capacity C in thermal contact with a thermometer [116]. It is due to the thermodynamic fluctuations of the number of thermal phonons exchanged with the heat bath through the thermal link G. These fluctuations lead to temperature fluctuations. One can derive directly from fundamental assumptions and definitions of statistical mechanics that

$$\langle U^2 \rangle = k_B T^2 C \tag{4.44}$$

using $\Delta U = C\Delta T$ it can be rewritten as:

$$\langle T^2 \rangle = \frac{k_B T^2}{C} \tag{4.45}$$

This, however, says nothing about the power spectrum. Studing the thermodynamic of the power fluxes, one can demonstrate that the power spectral density is given by:

$$P(\omega)^2 = 4k_B T^2 G \tag{4.46}$$

which is valid for a isothermic system. A white spectrum is the only spectrum that will give the correct result (4.44) for an arbitrary choice of C. Equations (4.44) and (4.46) are valid only in thermal equilibrium, where the temperature of the detector is equal to the temperature of the heat sink. In general, the detector will be at higher temperature than the heat sink, most usually due to the bias power used to read-out the thermometer. The power spectral density in the link will then depend on details of the nature of the link.

Using the naive approach where the detector and the heat sink are at the same temperature and taking into account the electrothermal feedback, the output noise spectral density is given by:

$$e_{term}(\omega) = P(\omega) S(\omega) \approx \sqrt{4k_B T^2 G} \frac{S(0)}{1 + j\omega\tau_e} \tag{4.47}$$

where $S(\omega)$ is the detector responsivity. Since the thermodynamic noise and the signal are characterized by the same dependence on frequency, it is possible to maximise the signal to noise ratio extending the using bandwidth. In reality, the Johnson noise of the thermistor makes this maximization impossible.

4.7.2 Extrinsic Noise

The bias circuit and the electronic used to read-out the thermistor are sources of extrinsic noise.

The load resistance Johnson noise could be normally made negligible by choosing $R_L/R \ll 1$. Also they must stay at the heat sink temperature. This noise is described by the current power spectrum

$$i_n RL(\omega)^2 = \frac{4k_b T_L}{R_L} \tag{4.48}$$

where T_L is the load resistance temperature. By reducing to the voltage power spectrum the expression becomes

$$e_n RL(\omega)^2 \sim 4k_B T_L \frac{R_s^2}{R_L} \tag{4.49}$$

Amplifier noise is normally specified as a voltage noise source $e_n A(\omega)$ in series with the amplifier input and a current noise source $i_n A(\omega)$ in parallel with the input as shown in figure 4.11.

The voltage noise source can be expressed by:

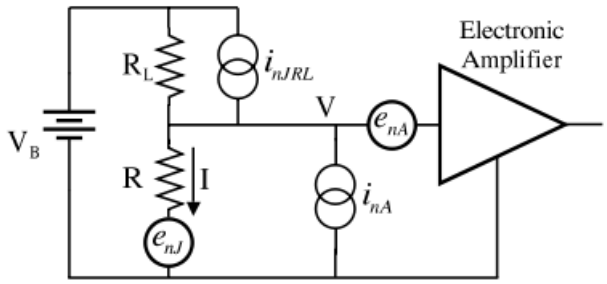

Figure 4.11: Equivalent circuit showing definition of amplifier noise and Johnson noise sources.

$$e_n A(\omega)^2 = 4k_B T \frac{0.7}{g_m} \tag{4.50}$$

where g_m is the transmittance and the current noise is:

$$i_N A(\omega)^2 = 2q_e i_{leak} \tag{4.51}$$

where i_{leak} is the leak current of the JFET gate and q_e is the electron charge. So the total noise is given by:

$$e_{tot}(\omega)^2 = e_n A(\omega)^2 + i_n A(\omega)^2 R \tag{4.52}$$

Other sources of noise could not be neglected. The $1/f$ noise, for example, appears only when the detector is polarized. Probably it is due to the presence of trapping centres on the semiconductor surface, i.e. it is a generation-recombination noise. At the bolometer working temperature its contribution is not negligible because the trapping time is longer and longer.

Finally, the mechanical microphone noise due to mechanical vibrations is not a negligible source of noise. For example, the noise due to the mechanical vibration of the wires used to read-out the detectors is proportional to the detector impedance. Its amplitude does not depend on the absolute value of the capacitance associated to the wires, but by the percentage change.

Chapter 5

The MARE-1 Experiment

In this chapter the entire experimental set-up of the MARE-1 experiment is described in detail.

5.1 The experimental set-up of MARE-1 in Milan

As said in the first chapter, one of the MARE-1 activities is carried out in Milan by the group of Milano–Bicocca in collaboration with NASA/GSFC and Wisconsin groups. The goal of this experiment is to achieve a sensitivity on the neutrino mass of few eV. Giving an alternative approach to the spectrometers, it has the potential to validate the spectrometers results [28, 29]. In order to achieve a sensitivity of few electronvolts, a total statistics of about 10^{10} events is necessary. Such statistics can be collected in 3 years running 288 detectors (corresponding to an exposure of 864 det$\times$years), with each detector having an activity of about 0.27 decays/s. As the Montacarlo simulations have shown (see chapter 2), a sensitivity on neutrino mass of 3.0 eV at 90% CL could be achieved in 3 years using the 288 MARE-1 detectors, each with an energy and time resolutions of about 30 eV and 300 μs, respectively. Finally, the purpose of this experiment is also to investigate the systematics of ^{187}Re neutrino mass measurements, focusing on those caused by the Beta Environmental Fine Structure (BEFS) [47, 49, 50] and the beta spectrum theoretical shape.

The experiment is installed in a dilution refrigerator located in the cryogenic laboratory of the University of Milano-Bicocca and the Milan MARE-1 detectors are based on semiconductor thermistors, provided by the NASA/GSFC group, with dielectric Silver Perrhenate absorbers, $AgReO_4$.

5.1.1 Microcalorimeter

Absorber

As said above, the absorber is made of single crystal of Silver Perrhenate ($AgReO_4$), a dieletric compound of Rhenium. The Silver Perrhenate has been selected because it is characterized by better thermal and physical properties than the other compounds of Rhenium, as $Re_2(CO)_{10}$, K_2ReCl_6, $KReO_4$. $AgReO_4$ crystals (PM=358.066, PA_{Re} = 186.2, ^{187}Re$\approx$ 62.8%) are transparent, crumbly and slightly hygroscopic. The crystalline structure of $AgReO_4$ is *scheelite*, with four molecules per unit cell and tetragonal symmetry (see figure 5.1).

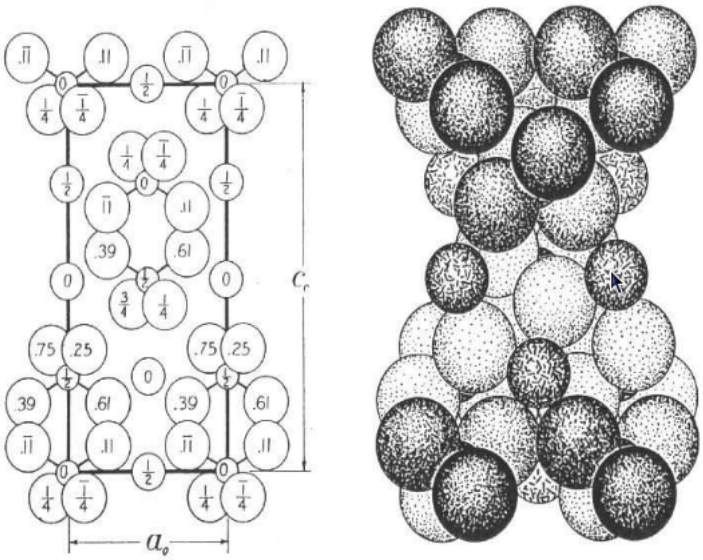

Figure 5.1: $AgReO_4$ structure. In the righ panel the biggest atoms are the Oxigen atoms, while the smallest ones are the Silver atoms.

At room temperature the cell is characterized by: $a_0 = b_0 = 5.378$ Åand $c_0 = 11.805$ Å. The decaying Rhenium atom is surrounded, with almost tetrahedral symmetry, by four oxygens located at an approximate distance of 1.7 Å. Four equivalent covalent bonds are responsible for the anion structure. The Ag^+ ion is 3.8 Åaway at room temperature.

Exposing the crystals to the air their colour becomes slightly yellow and cleaning them with ethanol it comes back as before. Knowing the ^{187}Re half-life ($\tau_{1/2} = 42.3 \times 10^9$ years), its molecular weight (358.066) and its isotopic abundance (62.8%), one can derive the $AgReO_4$ beta specific activity, which is about 5.4×10^{-4} Hz/μg. A possible target for the single crystal mass, resulting from a trade-off between rate, pile-up and energy resolution is around 500 μg, corresponding to a single detector rate of about 0.3 Hz. Tha $AgReO_4$ absorbers are grown by Mateck GmbH in Germany. Mateck has developed a

procedure to grow large single crystals with high purity and to cut them as precisely as possible. So the crystals are cut in regular shape of 600 x 600 x 250 μm^3.

It is important to underline the difference between the extremely compact metallic Rhenium structure ($\rho = 20.8$ g/cm^3) and the relativity low-density Silver Perrhenate ($\rho = 5.7 \pm 0.9$ g/cm^3). In metallic Rhenium no unused atoms (additional heat capacity) are added, instead in $AgReO_4$ Silver and Oxygen are spectator atoms (i.e. they do not decay). Thanks to their presence the BEFS (*Beta Environment Fine structure*) effect is one order of magnitude reduced for $AgReO_4$ with respect to the metallic Rhenium case, assuming the same energy resolution.

Temperature sensor

The Milano MARE-1 temperature sensors are arrays of semiconductor thermistors provided by NASA/Goddard. These arrays, developed as detectors for the XRS2 experiment on the ASTRO-E2 mission, consist of 6 x 6 implanted Si:P thermistors with a size of 300 x 300 x 1.5 μm^3. An energy resolution of 3.2 eV FWHM at 5.9 keV has been obtained with these thermistors and HgTe absorbers [121]. Outside the 6 x 6 grid there are other four pixels: two of them are suspended, while the other two are embedded in the silicon wafer. The latters are used to monitor the temperature of the array itself. The XRS-2 array is produced using innovative technology for silicon thermistor. In fact, the DRIE technology (*Deep reactive ion etching*) together with the use of *wafer SOI* (*Silicon on insulator*) allow to obtain suspended pixels of different shapes. Using a high temperature annealing the impiant is uniformly diffused throughout the depth of the top layer of the SOI wafer, thus the pixels are characterized by an uniform doped over all the volume. In addition, the uniformity in the volume lowers the $1/f$ noise. In conclusion, the combination of all these innovative techniques leads to an uniform doping, a substantial increase of the electron-phonon coupling (i.e. implants with bigger volume), a decrease of $1/f$ noise and a greater reproducibility of the geometry of these devices. A detailed description of the production of these devices is reported in [122].

These sensors are equipped with supports for absorbers. These supports, made of SU-8 epoxy resin, are produced using the photolithographic technique. Each pixel is suspended by four support beams, in two of them the electrical contacts are present. These beams are also the thermal contact between the thermometer and the heat sink. The conductance of one support beam is about 7x10^{-11} W/K at 100 mK. Figure 5.2 shows a sketch of the structure for a single pixel and a picture of the entire array.

The $R(T)$ dependence of these devices is modeled by the NASA/Goddard group trough this modified VHR formula:

$$R(T) = R_0 e^{\sqrt{T_0/T_e}} + R_0' e^{\sqrt{T_0'/T_e}} \tag{5.1}$$

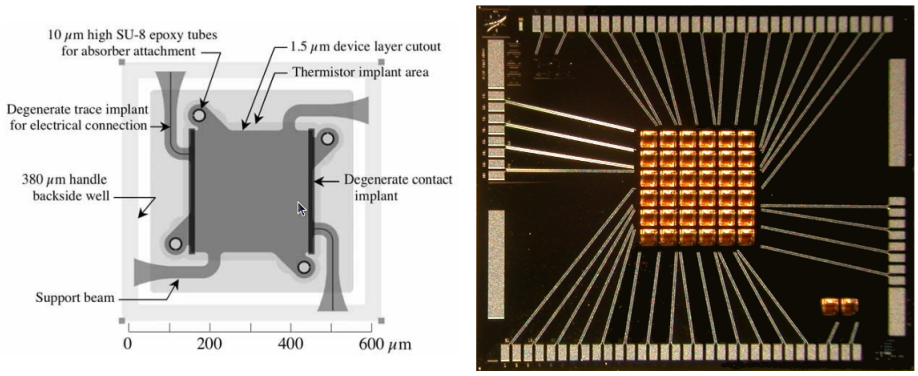

Figure 5.2: Left panel: the structure of a monolithic X-ray detector with ion-implanted thermistor. Right panel: a full view of the 6x6 array. One can glimpse the two embedded pixels in the upper left corner and see the two sunspended pixels in the lower right corner.

with $R_0 = 270\,\Omega$, $T_0 = 7.2$ K, $R_0' = R_0(2.522T_0^{-0.25} - 8.733)$ and $T_0' = 2.715T_0 + 1.233$K. It is a purely empirical function, but it introduces no additional free parameters. Also it considerably increases the temperature range over which a good fit can be made. The function is designed to give the same values for T_0 and R_0 as the Coulomb gap model if data are only fit at high temperature. This calibration has been performed randomly picking up the arrays of *wafer C*. For this reason, it has been decided to calibrate the array which has been used in the test runs (see chapter 6). Due to the non-uniformity of the thin layer on which the plant is diffused, the dopant density varies depending on the position occupied by the array in the wafer even if the wafer is uniformly doping. A variation of the dopant density is reflected in different values of R_0, T_0. Therefore, the characteristic parameters (i.e. γ, T_0 and R_0) of one of the two embedded pixels are determined. The static characterization is performed for temperatures which spans from 56 mK to 1 K. For each heat sink temperature the load curve relative to this pixel toghether with the heat sink temperature are recorded .

The $R(T)$ dependence is shown in the left panel of figure 5.3, while the acquired loads curves in the right panel of figure 5.3. The load curves are analysed using the VRH model and the model of the electron-phonon thermal decoupling.

In table 5.1 are listed the parameters extrapolated by analysing the load curves.

Detector Assembly

The assembly of the crystals on thermistors is made using a specially designed micropositioner. It is composed by a series of translation and rotation stages which permit the perfect positioning of the crystals on the sensor so that crystal faces are parallel with thermistor surface. In particular it consists of three different main parts: a syringe needle used

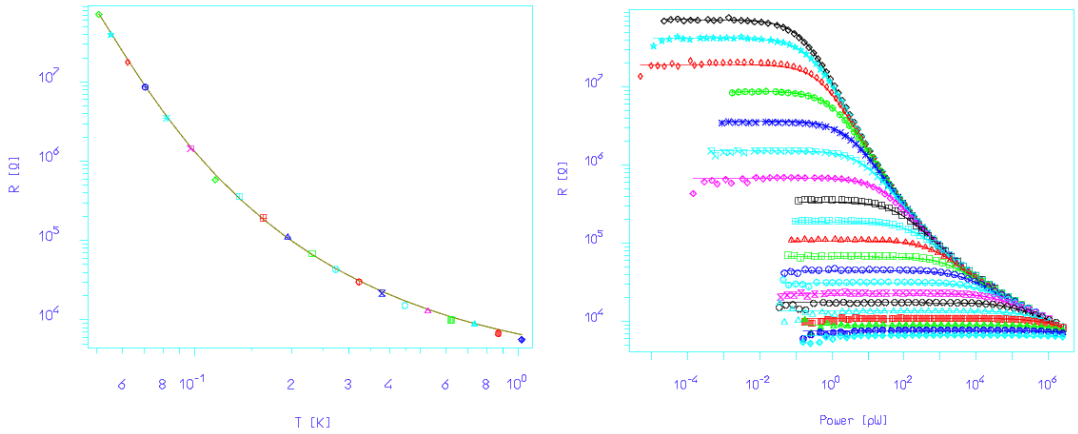

Figure 5.3: a) The $R(T)$ dependence. b) Load curves analysed using the VRH model and the model of the electron-phonon thermal decoupling. Each curve corresponds to a different heat sink temperature.

Parametro	**valore**
γ	0.74 $\pm$0.06
$\mathbf{ln}(R_0)$	7.6$\pm$0.3
$T_0[\mathbf{K}]$	1.3$\pm$0.3
α	6.1$\pm$0.3
$\mathbf{g}_{ef}$ $[\mu\mathbf{WK}^{\alpha}]$	(15$\pm$1)

Table 5.1: The parameters estrapolated by analyzing the load curves.

to vacuum pick-up the crystals, a table movable in the directions of the three-dimensional axes and rotatable in $\theta_x - \theta_y$ and a mechanical arm where the needle is mounted. A little tip, which picks up the resin used to glue the crystals, is located to 90 degrees from the syringe needle. Also this arm is movable in 3 directions (XYZ) thanks to three different manipulators. All the system is placed in a ISO 6 area to minimize the dust contamination of the detectors.

A previous work has shown that gluing the crystals directly on the SU8 supports the detectors pulses were very slow and small due to the weak thermal link introduced by the SU8 between the crystals and the sensors. The same work has shown that the best approach for mounting the $AgReO_4$ crystals on the XRS2 array is gluing silicon chips of 300 x 300 x 10 μm^3 between the thermistors and the rather large absorbers. In this way the silicon chips act as spacers fitted between the four SU8 supports. To better understand the spacer approach a sketch of our microcalorimeter is displayed in figure 5.4.

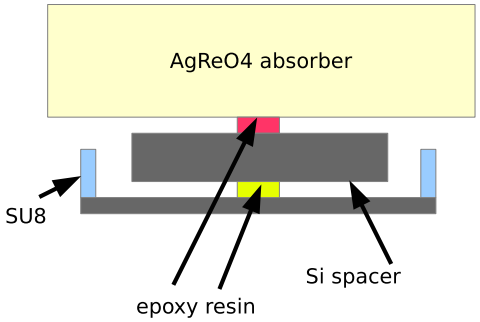

Figure 5.4: Structure of $AgReO_4$ microcalorimeter.

Concerning the best thermal coupling between the thermistor and the spacer and between the spacer and the crystal different epoxy resins have been tested during the years. The obtained results will be presented in the next chapter.

5.1.2 The Front-End system

One of the most stringent requirement of this experiment is the fast response of the detectors. The parameters that allow to achieve this goal are a large value of the electron-phonon thermal coupling G_{ep} and and a small value of the thermistor resistance. These features together tend to reduce the energy conversion gain of the detectors. The trade-off between response speed and signal amplitude depends on the thermistor parameters (i.e. R_0 and T_0) and on the detectors assembling. For MARE-1 detectors a good compromise is found at an operating temperature of about 85 mK with a thermistor static impedance of about 4 MΩ. The dynamic impedance of the detector is inductive and saturates to the value of the static impedance at large frequencies. Since the detectors are characterized by a high impedance, the parasitic capacitance must be minimized in order to avoid excessive signal

integration. We want to point out that the speed response of the detector depends on the combination of the detector impedance - that increases at low temperatures - with the parasitic shunting capacitance. The variation of this capacitance is furthermore responsible for microphonic noise generated by wire vibrations.

To match to the impedance of the thermistors and to reduce the parasitic shunting capacitance a cold buffer stage, based on JFETs working at 120 K, is installed as close as possible to the detectors. In this way, the signal present at the high impedance detector node is transmitted to the low impedance output of the JFET. In addition, the presence of a cold buffer stage reduces the JFET leak current (i.e. at low temperature this leak current is few fA) and allow to put the load resistances at the Mixing Chamber temperature, so their Johnson noise could be neglected. For the expected operating conditions, the JFETs have a white noise of 0.8 nV/Hz$^{1/2}$ with a dissipated power between 0.1 mW and 1 mW. In order to reduce this dissipated power the JFETs are in a unity gain configuration.

This first stage, placed 15 cm away from the detectors, is followed by an amplifier stage at room temperature. This amplifier stage subtracts the reference ground signal from the signal presents at the cold buffer output, rejecting the spurious disturbances from the common mode disturbances, e_M, at the output of the chain. The presence of only one reference ground signal for all the channels avoids the ground loop interference. The output signal is filtered with an active Bessel low pass antialiasing filter, placed close to the acquisition system. Then the signals are acquired by a commercial DAQ system. A sketch of the front-end scheme for the detector readout of MARE-1 bolometers is shown in figure 5.5. A detailed description of the Milan MARE-1 electronic can be found in [123, 124].

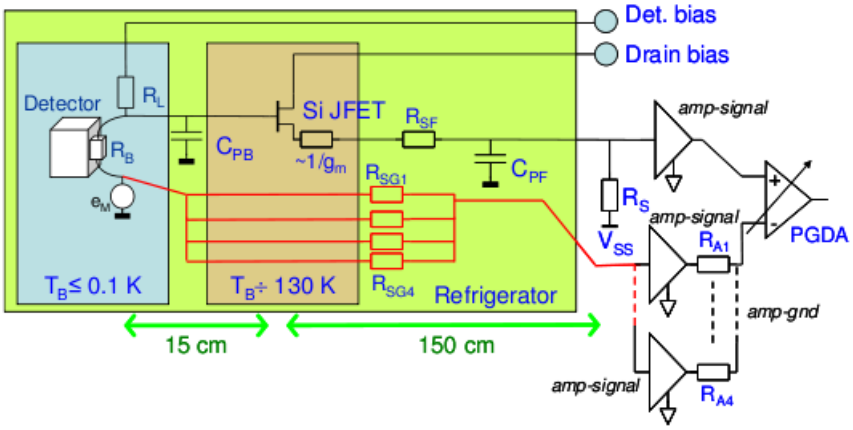

Figure 5.5: A sketch of the front-end system for the readout of MARE-1 bolometers [123]. R_b and R_L are the detector resistance and the load resistance, respectively. g_m is the transconductance of the Si-JFET and R_{SF} is the parasitic resistance of the connecting wires. e_m is the common mode disturbances and the R_{SGi} is the parasitic resistance of the connecting wires, in this case the link is implemented with more wires in parallel and results in a few tens of Ω. PGDA stands for Programmable Gain Differential Amplifier.

For a very long measurement time the stability of any part of the system is extremely important. For this reason the power for every channel is given by a set of power supplies especially designed to show a very low thermal drift, less than 5 ppm/°C, and an average noise less than 50 nV/Hz$^{1/2}$.

A Faraday cage is located on the top of the cryostat. The amplifier stage at room temperature and the detector biasing are allocated inside it. Another Faraday cage, close to the DAQ system, contains the antialising filters. All the walls of the cages are covered by SKUDOTECH, a special alloy with very high magnetic permittivity. In this way the electronics is shielded from electromagnetic interferences.

5.1.3 The Laboratory and the Cryostat

The Milan MARE-1 experiment is installed in a Kelvinox KX400 dilution unit in the Cryogenic Laboratory of the University of Milano-Bicocca. The laboratory is located in the basement of the Physics Department of the Milano-Bicocca University, about 12 m below the street level.

The refrigerator has been designed for minimum vibration sensitivity. It is hung to a 1.5 tons 1.9 x 1.9m^2 square plate made by a Stainless Steel - wood - Stainless Steel sandwich. The plate is mounted on 4 high performance laminar flow isolators which filter horizontal and vertical vibrations above 1 Hz. All pumping lines are run through a sand box to reduce the vibration transmission and further mechanical isolation is provided by soft edge-welded bellows. In particular the 50 mm large ^{3}He pumping line is mechanically decoupled by means of a double-gimbals assembly (see picture 5.6 for more details). In order to guarantee the correct electrical grounding of the instruments all pumping lines are also electrically decoupled.

The refrigerator has a cooling power of about 400(32) μW at 100(50) mK and a base temperature of about 6 mK. The avaible experimental space, located under the Mixing Chamber plate, has a diameter of about 17 cm and a height of about 30 cm and it is enough to host the detectors and the JFET boxes.

The dilution unit is customized: a copper rod (20 mm of diameter) traverses it from the 4K flange to the bottom of the still shield. This 4 K rod is used to hold the structure of the JFET electronics at 4.2 K very close to the arrays. The thermal anchorage can stand a power dissipation of about 100 mW with a temperature increase of only 1 K.

The cryostat is equipped with three different ports, two of them are used for the experimental cabling (i.e. wires for the detector bias and wires for reading the JFETs source) and the other for the calibration source system. The bias connectors box, the source connectors box and the calibration system box are mounted on these ports. Their vacuum seal is tested (i.e. helium vacuum leak rate lower than 10^{-8} mbar l/s at room temperature). Figure 5.7 shows the top of the cryostat with the three boxes mounted.

Figure 5.6: Mechanical assembly for vibration isolation (double gimbals) of the ^{3}He pumping line.

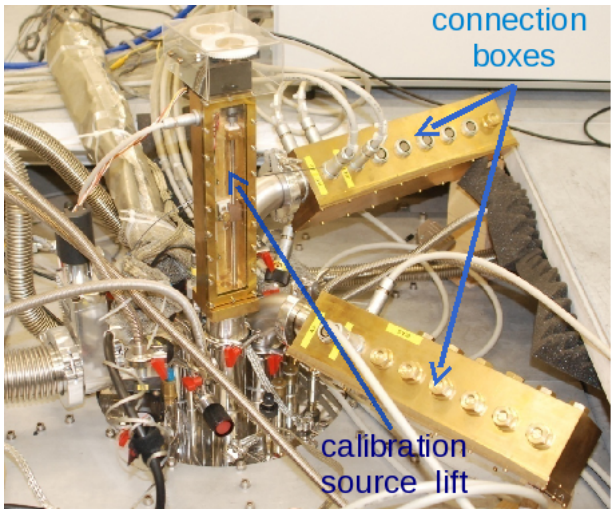

Figure 5.7: The figure shows the box for the calibration system and the two connection boxes, one for the detector bias and the other for the JFETs source.

The experimental wiring consists of woven ribbon cables produced by Tekdata [1] both for the bias signals and for the source signals. Each ribbon cable is equipped with a high quality cryogenic woven loom for all low temperature installations and it is composed by 27 manganin wires with a diameter of 0.1 mm. The total length of one bias ribbon cable is around 280 cm, while the total length of one source cable is around 250 cm. Woven ribbon cables have been chosen thanks their capabilities to make efficient use of space, whilst also to provide effective performance (low noise, crosstalk defined by repeatable wire positioning). The connectors at room temperature are 27 ways leak tight Fisher connectors, while the ones at low temperature are the Micro D connectors with 25 ways. The experimental wiring is thermalized through pieces of copper with three slits produced using an electroerosion machine. Taking a serpentine path, the manganin wires are glued with ST2850FT inside the copper pieces. For the bias ribbon cable there are five thermalization stages placed at 4 K, 1.2 K, 600 mK, 50 mK and at the mixing chamber temperatures, while for the source wires there is only one thermalization stage at 4 K. Figure 5.9 displays one bias ribbon cable. Up to now only 4 bias ribbon cables (i.e. 108 manganin wires) and 4 source ribbon cables (i.e. 108 manganin wires) are installed in the cryostat, this is the number necessary to read two arrays. Tables 5.2 and 5.3 show an approximative calculation of the total powers which flow trough the bias and source wires in the different thermalization stages. For temperatures above 1 K the powers are calculated using the value of thermal conductivity reported in [125], while for temperatures below 1 K the powers are calculated from the manganin thermal conductivity reported in [126].

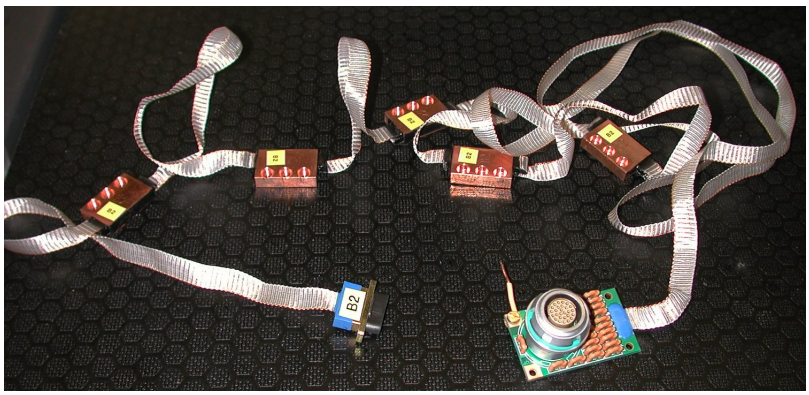

Figure 5.8: One bias manganin ribbon cable. The copper pieces glued on the wires are for thermalizing.

[1] Tekdata Interconnections Limited, Innovation House, The Glades, Festival Way, Etruria, Stoke-on-Trent, Staffordshire, ST1 5SQ, UK

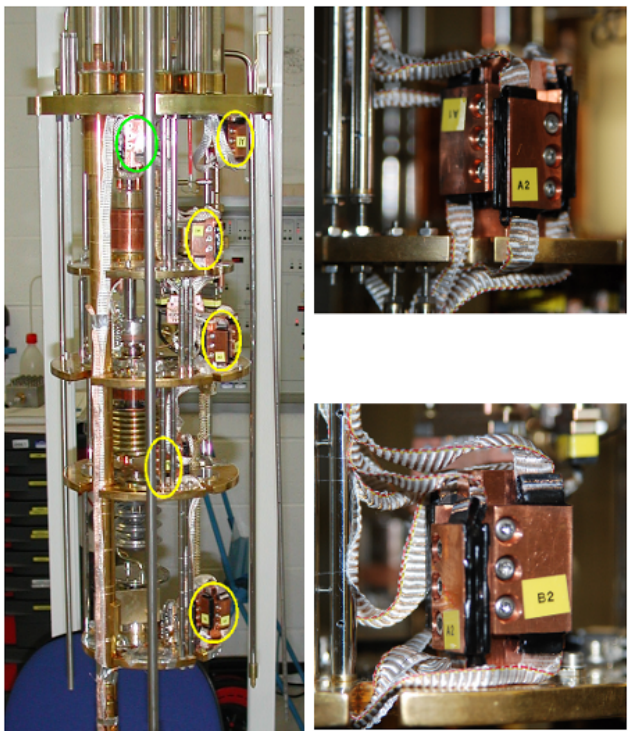

Figure 5.9: Left Panel: the entire cryostat cabling. In yellow the thermalizations for the bias wiring, while in green the thermalizations for the source wiring. One can see that the source wiring, after the thermalization at 4 K, runs along the entire lenght of the 4 K rod. Right panel: a zoom of the bias thermalization stage at 1.2 K in the figure above and a zoom of the one at 600 mK in the figure below.

lenght [cm]	T_1 **[K]**	T_2 **[K]**	P_{tot} **[μW]**
150	4	300	~ 3000
21	1.2	4	~ 2
14	0.6	1.2	~ 0.3
18	0.05	0.6	~ 0.02
28	0.035	0.05	~ 0.00008

Table 5.2: Total thermal power which flows through the bias wires. The total number of the wires is 108, which corresponds to 4 ribbon cables.

lenght [cm]	T_1 **[K]**	T_2 **[K]**	P_{tot} **[mW]**
150	4	300	~ 3
100	4	4	0

Table 5.3: Total thermal power which flows through the source wires. The total number of the wires is 108, which corresponds to 4 ribbon cables.

5.1.4 The Cryogenic set-up

In this section the baseline of the MARE-1 cryogenic set-up, shown in figure 5.10, is explained in detail. The experiment is designed to host up to eight XRS2 arrays (288 detectors), although only two of them with electronics have been installed so far. In fact, depending on the results obtained, we will decide whether or not to extend up to eight the number of arrays. For that reason, read-out cryogenic wiring, preamplifers, anti-aliasing filters, triggers and DAQ system have been only installed for 80 channels.

Detector Holder

The array is glued on a triangular ceramic board with ST2850FT. The ceramic, which has a coefficient of thermal expansion well matched to that of silicon, provides the thermalization and the electrical contacts. The output of the board is connected to the load resistor board by a commercial connector. A second connector is soldered at the back of the first one to make a connection to the lower stages. On the top of the ceramic between the output and the array there is a thickening of the ceramic. This thickening, which is gold plated, is connected to ground and it has been added to the ceramic layer both for better thermalizing the ceramic and shieldign the array from thermal radiation coming from the outside of the detector holder. The thickness of the ceramic is 1 mm and it becomes 1.5 mm close to the output. The schematic of the array ceramic board is shown in the left panel of figure 5.11, while the array ceramic board equipped with the XRS array is shown in the right panel of figure 5.11. The parasitic capacitances between two electronic tracks are no more than few pF.

Finally, two copper bars are glued on the top and on the bottom of the ceramic. One bar is visible in the right panel of figure 5.11. Fitting in the gold plated detectors holder where the ceramic is placed, these bars allow to better shield the detectors from the thermal radiation. The detectors holder, screwed to the Mixing Chamber plate, is made of copper and it is divided in eight compartments to host 8 arrays. There is a hole in the centre to allow the passage of a nylon wire (see section 5.1.5). A copper cover with squared holes aligned to the array positions is screwed on it. The holes are covered by an Al foil to let the calibration X-rays pass and to shield the thermal radiation. The Al foil stops also the Auger electrons coming from the calibration source.

On the top of the detectors box there is the bias network with load resistors glued on a printed circuit board (PCB). Each load resistor is made by a series of two 1 x 1 mm^2 silicon chips with 25 MΩ NiCr resistive film. Figure 5.13 shows the load resistance PCB.

Decoupling stages and JFET Holder

As said above, the MARE-1 front-end has a cold buffer stage followed by a room temperature operated amplifying stage. The cold buffer stage is very close to the detectors and it

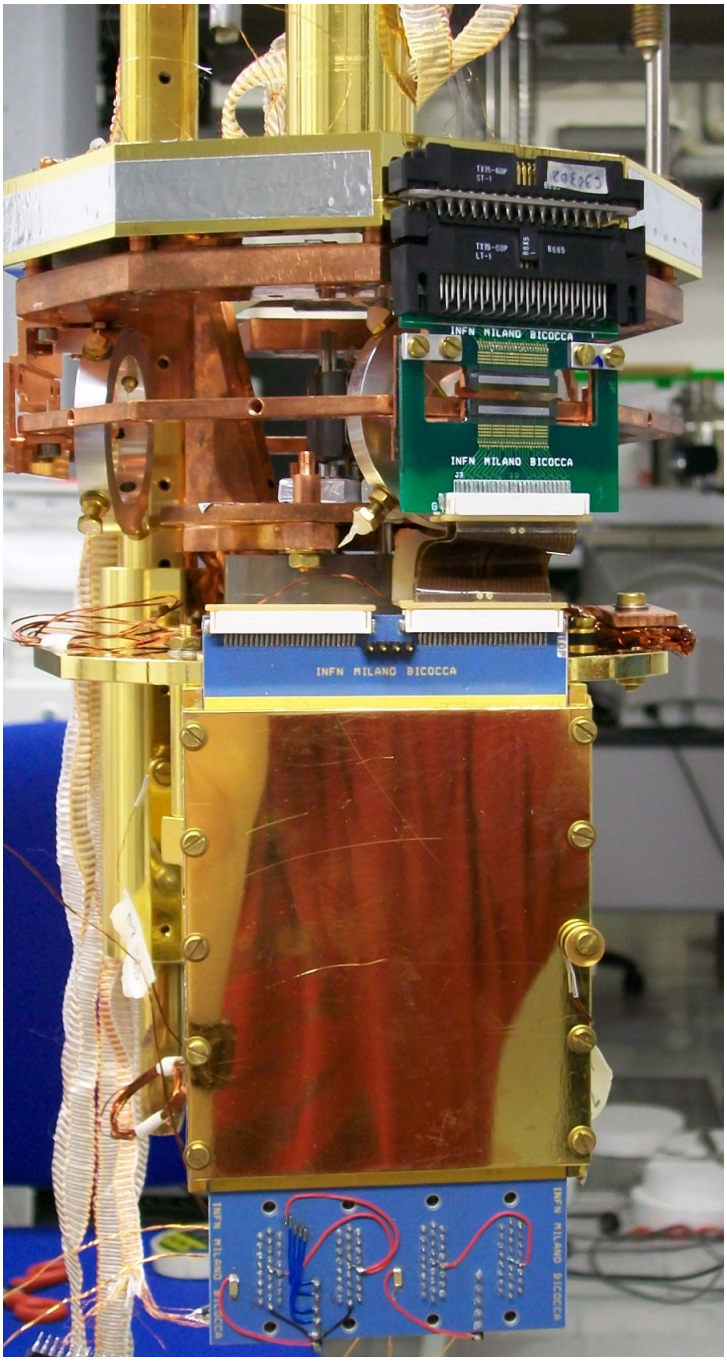

Figure 5.10: The MARE-1 cryogenic set-up. Only one array is present.

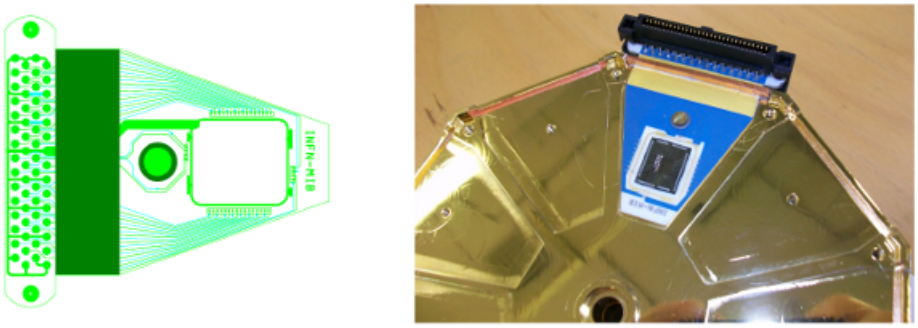

Figure 5.11: On the left panel a schematic of the ceramic board, composed of 40 independent wires (for 40 pixels) and a common ground (around the array) to simplify the wiring of the ceramic board. On the right panel the ceramic board with the XRS array. On the top of the ceramic: the gold plated thickening and the copper bar that fits with the cover of the detectors holder.

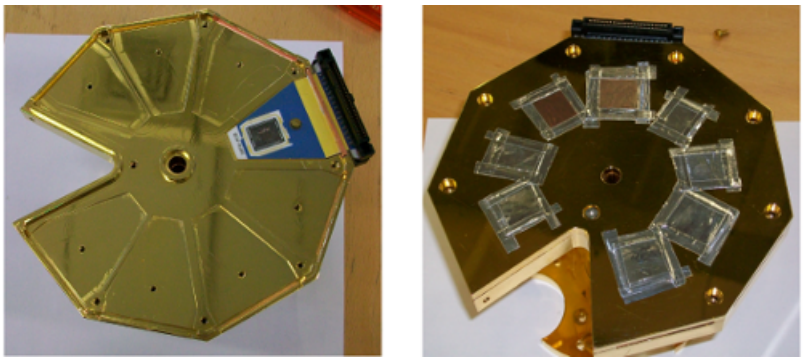

Figure 5.12: The picture on the left shows the detector holder with an arrays mounted. The array is equipped with ten $AgReO_4$ crystals. The picture on the right displays the detector holder with its cover. On can see the Al foils which cover the squared holes for the detectors calibration.

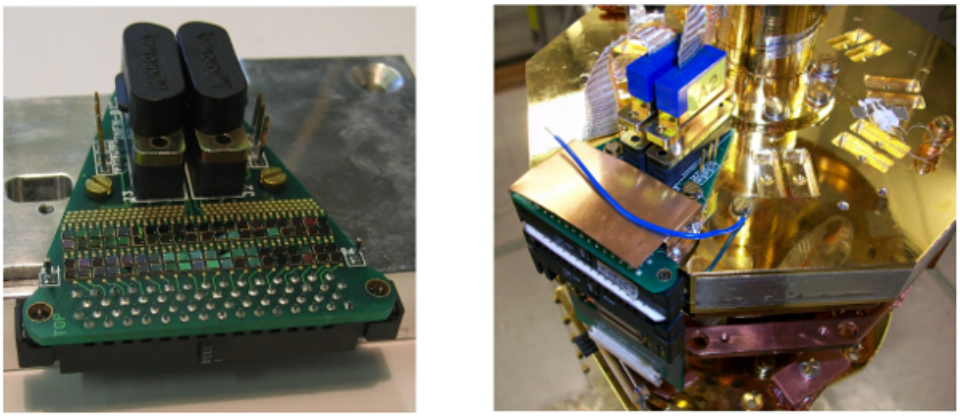

Figure 5.13: On the left panel: the PCB where the load resistances are glued with ST2850FT. On the right panel: the load resistance PCB screwed on the detectors holder and connected to the bias network.

matches to the detectors impedance. The close coupling of the detector and the amplifier requires careful thermal design. The main issues are:

- protect the detectors from the thermal radiation coming from JFETs at 120 K
- thermally isolate the JFETs PCB.
- provide low thermal conduction electrical connections between the JFET gates and the detectors

The technical challenge has been to design short wires between the detectors and the JFET electronics and, at the same time, to provide the thermal decoupling. To electrically connect the cold buffer stage (120 K) to the detectors at 85 mK two different stages of microbridges are used. Microbridges are low thermal conductance wires produced by Memsrad/FBK in Trento, Italy. They consist of silicon chips with metal traces evaporated on free-standing, serpentine polymide. The serpentine is 20 μm wide and about 5 mm long. The metal traces are made of Al or Ti. The microbridge production is based on photolitographic technique and it takes place in several steps:

- a thin layer of Al or Ti (200 nm thickness) is deposited onto a silicon wafer (300 μm) covered by protective layers made of SiO_2 and Si_3N_4 (left panel of figure 5.14)
- production of conductive serpentine wires through photlitographic technique
- deposition of a polyammide film (3 μm)
- etching of silicon wafer under the serpentine wires. In this way the wires are suspended and held only by the polyammide film.

– deposition of Al pad for bonding. (see right panel of figure 5.14)

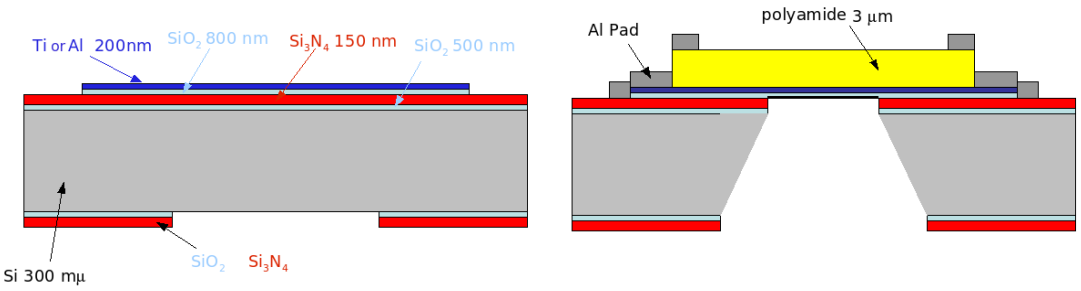

Figure 5.14: Left Panel: one of the first steps of microbridges production. Right Panel: the microbridges final structure.

The pictures of microbridges before and after the silicon wafer etching are in 5.15.

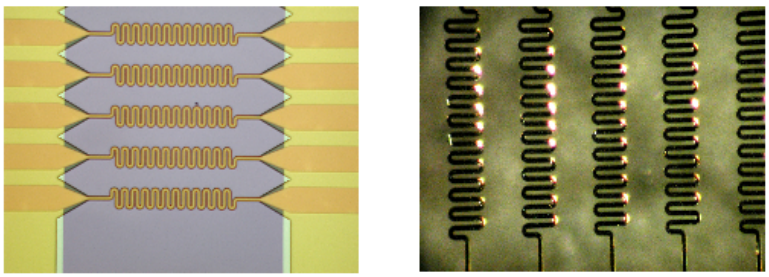

Figure 5.15: Pictures of microbridges before and after silicon wafer etching.

Microbridges do not guarantee the mechanical stability. Therefore, material with low thermal conductivity are used as mechanical support, namely Kevlar and Vespel.

The first microbridge stage provide the thermal decoupling between the detectors and the JFET holder at 4 K. These microbridges are made of Titanium. The heat flow [2] through a single wire from 4.2 K to 85 mK is as low as 10 nW, and the typical resistance of such a wire is 3 kΩ [129]. The mechanical support consists of 3 Kevlar crosses. At the

[2]The heat carried by a material of cross-section A and length l with a thermal conductivity coefficient k and with temperatures T_2 and T_1 at its ends is $P(T) = \frac{A}{l}\int_{T_1}^{T_2} k(T)dT$

ends of the arms of the crosses brass screws are glued with Araldit. By screwing these screws in the Al holder it is possible to stretch the crosses arms.

Kevlar is an aramid fiber characterized by high tensile strength, high hardness and a good thermal stability over a wide range of temperatures. It has a Strength-to-weight ratio [3] equal to 2.5 kN m/Kg, which is higher than other commercially available fibres. In addition, it is characterized by a high breaking strength to integrated thermal conductivity ratio. For example, in the range between 0 and 4 K this ratio is equal to 47244 MPa m/W for Kevlar 49 and it is equal to 1099 MPa m/W for SS 316LN [128]. It was used to suspend the cold stage of the ASTRO-E2 experiment, launched into the space in 2005. Kevlar is strong enough to withstand the stress of launching (up to 200 g's) as well as allow very little heat conduction to occur. It has been measured that the breaking force of the Kevlar used in MARE-1 is around 3.4 kg. The conductivity of our Kevlar is given [129]:

$$k(T) = (0.18 \pm 0.05)T^{0.6\pm0.1}\mu W/K^{0.6} \tag{5.2}$$

So the heat flow through a single cross from 4 K to 85 mK is around 0.7 μW. This stage is screwed on the cover of the array holder and the 4 K parts are suspended by these crosses. This structure can be seen in the left panel of figure 5.16, while a zoom of one of the three Kevlar crosses can be seen in the right panel.

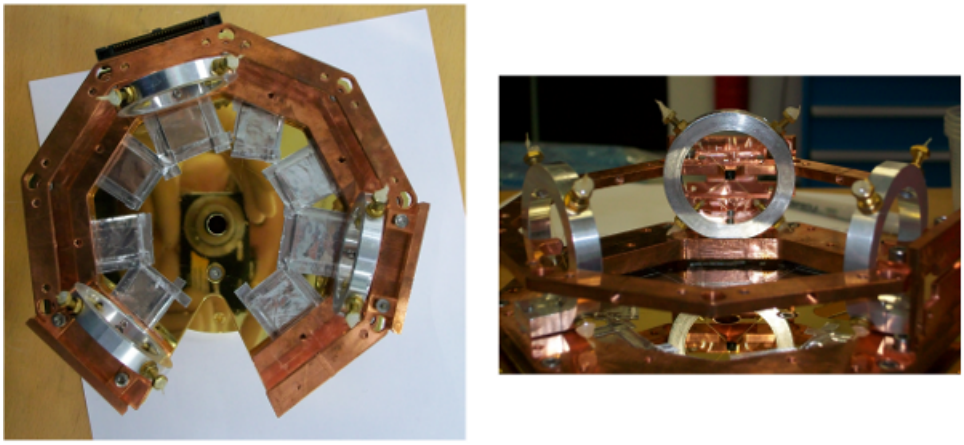

Figure 5.16: On the left panel: the assembly of the first decoupling stage. This picture shows the three Kevlar crosses connecting the detector holder to the 4 K parts. On the right panel: a zoom of one Kevlar cross. On the screw heads it is possible to see the drops of Araldit using to glue the Kevlar fibers at the screws.

The second microbridges stage is in the JFET box and the microbridges are made of Aluminium. The heat flow through a single wire between 135 K and 4.2 K is 80 μW and the resistance is 10 Ω at 77 K [129]. In this case two thin Vespel rods (150 μm thickness)

[3] strength as in tensile strength measured in MPa and weight in terms of density, i.e. g/cm^3

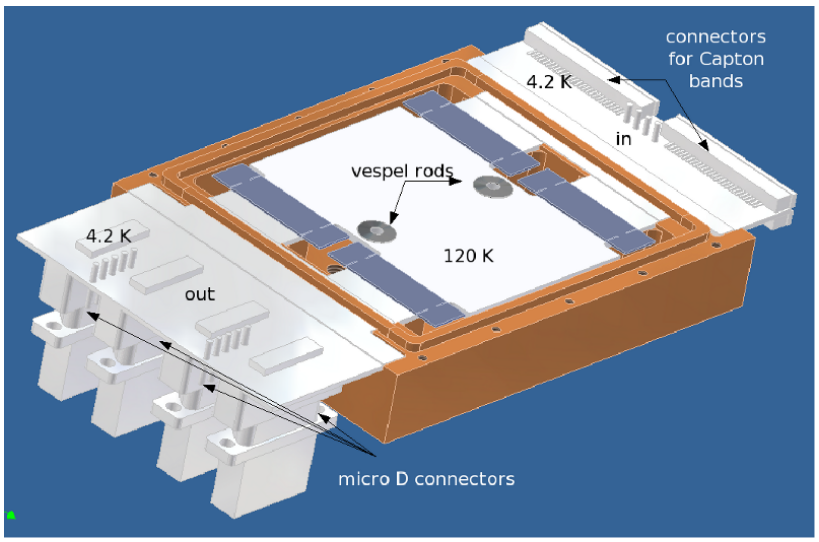

Figure 5.17: A 3D sketch of one JFET box.

are used as mechanical support - i.e. they are used in order to suspend the PCB where the JFETs are soldered . Vespel is a high performance polyamide resin characterized by low thermal and electrical conductivity, low coefficient of friction and good performance also at low temperature temperature. It combines the best properties of ceramics, plastics and metals. The thermal conductivity of our Vespel is $k(T) = 0.03 \pm 0.02T^{1.8\pm0.1}$ nW/K$^{1.8}$ [129], which means that each rod transports a heat flow of around 12.3 mW. The low conductivity of the Vespel allows to maintain the PCB temperature around 120 K without to dissipate too much power. In order to monitor the PCB temperature a Pt-100 thermometer is soldered on it. A 3D sketch of one JFET box is displayed in figure 5.17, while the assembled JFET box can be seen in figure 5.18. One box is foreseen for a readout of two arrays. The estimated heat flow from the PCB at 135 K to the structure at 4.2 K reaches 41.1 mW (i.e. 1.3 l of liquid helium evaporation per day). At the input and at the output, a ceramic board is glued with silver epoxy resin, which is used in order to better thermalize the ceramics and to better shield the outside of the JFET box from the thermal radiation coming from the 120 K parts. On the top of the both ceramics a copper bar that fits in the JFET box is glued in order to block the thermal radiation coming from the preamplifier. The JFET box is vertically screwed on a gold plated copper support fixed on the 4K rod.

5.1.5 The Calibration source

A calibration source completes the entire set-up. The energy calibration system, located between the detector holder and the JFETs boxes support, consists of fluorescence sources

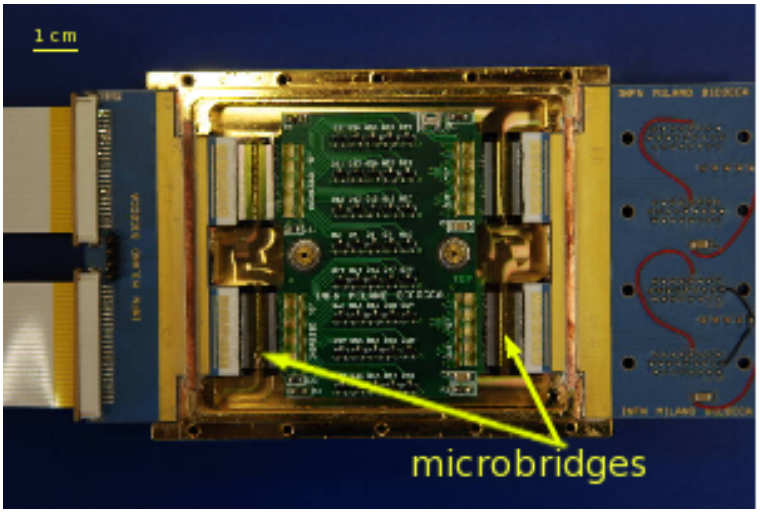

Figure 5.18: The assembled JFET box. This picture shows the four sets of Al microbridges, 40 JFETs soldered on the top of the dedicated PCB (the other 40 are soldered on the bottom) and the ceramic board. The PCB is screwed on Vespel rods. Heaters and thermometer are connected via spare lines of the microbridges of the output. For 72 detectors (2 arrays), one box is needed.

with 5 mCi of ^{55}Fe as a primary source movable in and out of a Roman lead shield [127]. The movement of the calibration source is controlled by a stepper motor placed on the top of the cryostat (see left panel of figure 5.19).

Thanks to the possibility to shield the calibration source between one calibration stint and the other, the background caused by the ^{55}Fe Internal Bremsstrahlung photons is avoided. The lead shield is screwed on the JFET box support. Within the shield, two Stainless Steel rods are fixed in order to guide the movement of the source holder. The source holder, made of lead, is hanged by a nylon wire. The ^{55}Fe source, as the shield, is at 4 K. The fluorescence targets, made of Al, Si, NaCl, and $CaCO_3$, are at 4 K as well and they allow a precise energy calibration around the end-point of ^{187}Re with the K_α and K_β X-rays. The distance between targets and detectors is around 7 cm.

The calibration source will be activated only at the beginning and at the end of an acquisition stint. One acquisition stint will extend for about 3 days between two liquid helium refillings. Assuming 3 hours per refilling and 3 hours per calibration period, the duty cycle should be about 88%. Assuming for the Al K_α line an activity of about 0.01 counts/s, at the end of one year the statistics for the single detector should be more than 25000 counts in the peak. This should be enough to obtain a precision of the order of 4% for the FWHM of the peak.

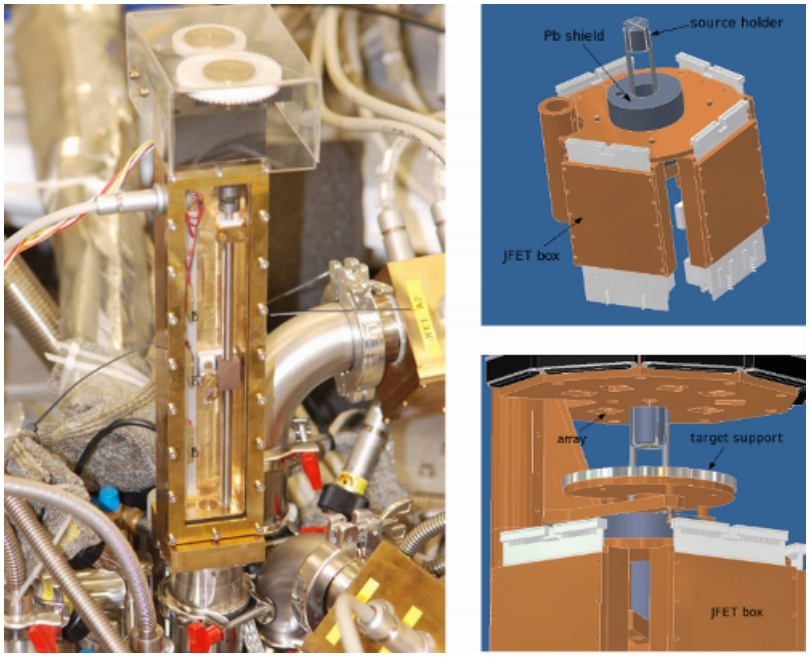

Figure 5.19: Left panel: The stepper motor of the calibration system. Right panel: in the upper picture the lead shield screwed on the JFET box support together with the source holder, while in the lower picture the position of the target is shown.

Chapter 6

Analysis and improvement of the MARE-1 set-up

In this chapter the activity concerning the assembly and the analysis of the MARE-1 cryogenic set-up are reported together with the improvements added from time to time.

6.1 Detector

First of all, the cool-downs aimed at studing the detector performance and characteristics are reported.

6.1.1 Detector performance

Different cool-downs were devoted to study different gluing methods using the spacer approach presented in section 6.1.2. The aim was to improve the detector performance, to check the crystal attaching reproducibility and to check the crystal quality. Therefore different kinds of glues were tested to attach silicon spacers on the thermistors and $AgReO_4$ crystals on the spacers, respectively. The detectors were assembled using the set-up described in 5.1.1. The optimal performance of such bolometers in terms of energy and time resolution as well as a good signal to noise ratio were obtained at a working temperature of around 85 mK where the resistance is about 4 MΩ. The masses and the resins combinations are listed in table 6.1 together with the baseline width and the energy resolution achieved near the ^{187}Re end-point [131].

The results of table 6.1 indicate that the combination Araldit R/Araldit R is favourable over the other glue combinations, but this epoxy resin deteriorates during the years and probably also due to thermal cycling. Therefore, the ST2850 has to be used to glue $AgReO_4$ absorbers on the silicon spacers. We would like to point out that MIBETA [27] also used ST2850 to directly glue the $AgReO_4$ crystals onto the thermistors; no spacers

RUN	**mass** [μ**g**]	**resin**	**baseline** [**eV**]	ΔE_{FWHM} [**eV**]	τ_{rise} [μ**s**]	**ΔV/6keV** [μ**V/(6 keV)**]
4X	402	Araldit R/Araldit R	14	28±1	308±3	155.1±0.1
4X	388	Araldit R/Araldit R	28	36±2	289±5	79.1±0.3
4X	456	Araldit R/ST2850	21	35±1	347±7	92.1±0.4
4X	470	Araldit R/ST2850	33	36±2	354±9	64.2±0.3
4X	406	ST1266/ST2850	22	36±1	314±5	95.2±0.4
4X	442	ST1266/ST2850	30	38±1	380±8	61.1±0.2
4X	506	ST2850/ST2850	113	-	507±27	21.4±0.2
4X	430	ST2850/ST2850	132	-	552±46	27.2±0.2
4X	390	SU8/ST2850	131	-	663±42	24.4±0.1
4X	386	SU8/ST2850	190	-	712±22	17.6±0.2
6X	273	Araldit R/Araldit R	18	22±1	200±3	136.3±0.3
6X	300	Araldit R/Araldit R	12	17±1	352±4	145.1±0.3
6X	427	Araldit N/Araldit N	36	44±1	240±9	64.2±0.3
6X	*402	Araldit R/Araldit R	35	36±1	273±4	94.2±0.3

Table 6.1: Listed are different absorber masses and their respective resin combinations. The first resin is between the thermistor and the silicon spacer and the second one between silicon spacer and $AgReO_4$absorber. (Araldit R= Araldit Rapid and Araldit N= Araldit Normal). * is the same detector as the first line but measured two years later. The working temperature is about 85 mK, which corresponds to a detector resistance of 4 MΩ.

were needed in that experiment.

Subsequently, a last test run with a new test array was carried out in Milan. The goal of this run was to find the best thermal coupling between the silicon spacer and the thermistor. For this purpose nine $AgReO_4$ crystals were attached to nine pixels using the spacer approach. Araldit Rapid, Araldit Normal and ST1266 were tested (see table 6.2).

RUN	**Det.**	**$AgReO_4$ mass [μg]**	**resin**
8X	1	497±2	Araldit R
8X	2	381±3	Araldit R
8X	3	421±2	Araldit R
8X	4	499±2	Araldit N
8X	5	604±1	Araldit N
8X	6	535±2	ST1266
8X	7	384±3	ST1266

Table 6.2: Listed are different absorber masses and the resins used to attach the silicon spacer on the thermistor.

Figure 6.1 displays the new test array equipped with the nine crystals of $AgReO_4$, on each crystals the energy resolution at 2.6 keV is reported. The characteristic parameters of this array (i.e. R_0, T_0 and γ) are listed in table 5.1.

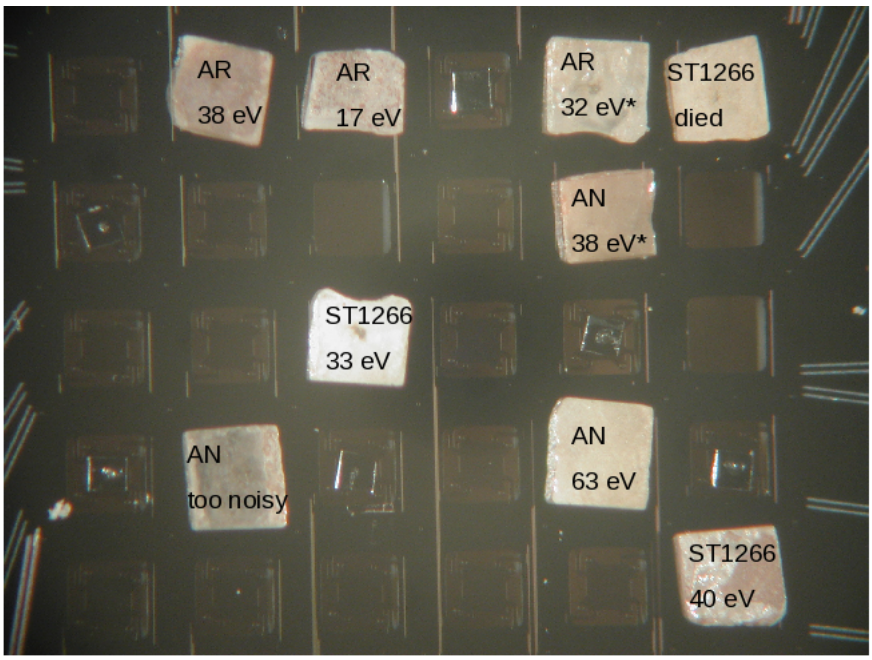

Figure 6.1: XRS2 array: view of several pixel with $AgReO_4$ absorbers for the last test. * were broken crystals. For those crystals the spectra were characterized by double peaks for each line.

During this run one pixel with ST1266 was broken and an other with Araldit Normal was too noisy to be acquired. A summary of the most interesting results is presented in table 6.3.

Det.	**baseline** [**eV**]	ΔE_{FWHM} [**eV**] **@ 1.4 keV**	ΔE_{FWHM} [**eV**] **@ 2.6 keV**	τ_{rise} [μs]	ΔV/6keV [μV/(6 keV)]
1	36	37±1	38±5	498±31	47.8±0.2
2	19	24±1	25±4	493±13	75.7±0.2
3	28	28±1	36±5	570±24	37.0±0.1
4	41	-	38±6	539±23	37.4±0.1
5	55	-	62±8	306±14	30.2±0.4
6	24	-	33±5	364±15	32.2±0.1
7	28	32±1	40±8	225±9	59.3±0.2

Table 6.3: Listed are the most interesting results obtained in the test run RUN8X.

The table 6.3 shows data collected at the temperature of around 85 mK ($R_{bol} \sim 4$ MΩ). A calibration spectrum of the detector 2 can be seen in figure 6.2. The calibration was made with the fluorescence lines (Al, Cl, Ca, Ti and Mn) of targets illuminated with ^{55}Fe source. Crystals number 3 and 4 were broken and so their spectra were characterized by double peaks for each line (figure 6.3).

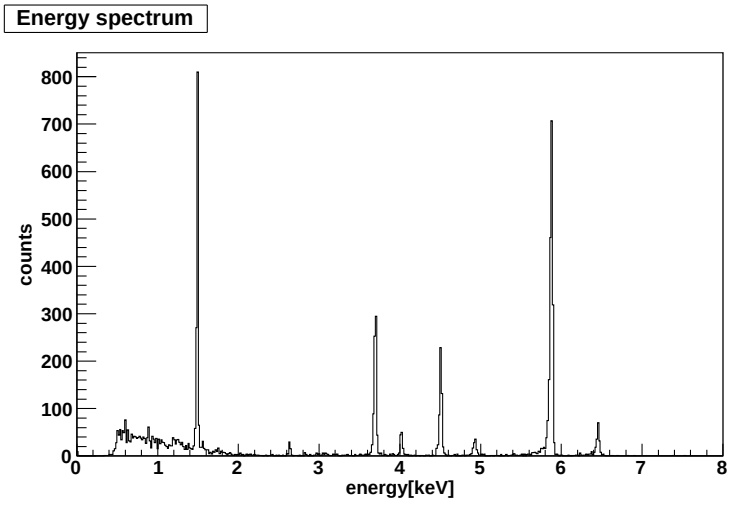

Figure 6.2: A spectrum of the test detector number 2 with an energy resolution of 36 eV at 2.6 keV in presence of a calibration source. The calibration is made with the fluorescence lines (Al, Cl, Ca, Ti and Mn) of targets illuminated with ^{55}Fe source.

A little difference between the pulse shape of detectors assembled with Araldit N and the pulse shape of the ones assembled with ST1266 was observed. Figure 6.4 shows this

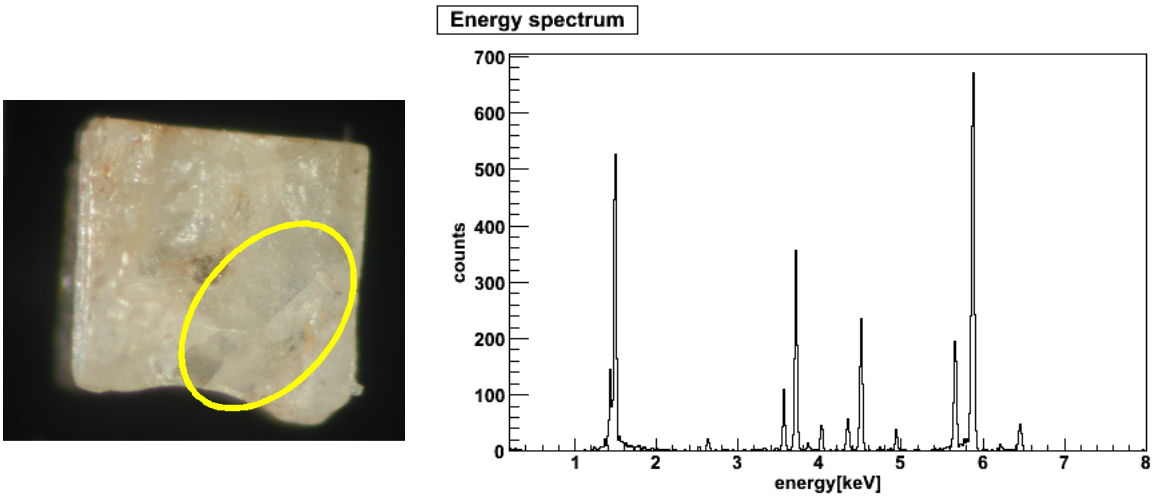

Figure 6.3: Crystal number 3 and its spectrum with double peaks for each line. It is possible to see the micro fracture in the right corner of the crystal. The black spot in the center of the crystal is the drop of ST2850FT used to glue it onto the silicon spacer.

difference. A further and deeper investigation of this behaviour will be done with the first array of MARE-1 (see section 6.1.2).

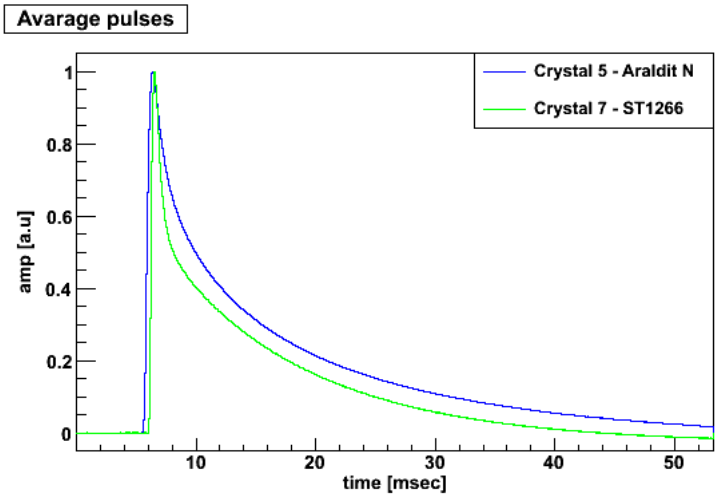

Figure 6.4: Avareged pulse of one detector assembled with Araldit N and an avareged pulse of one detector assembled with ST1266 after pulse height normalization. The time window is 50 ms wide.

These cool-downs have shown that it is possible to assembly detectors characterized by an energy and time resolution of around 30 eV and of about 300 μs, respectively. Crystals quality is in principle good, but micro fractures have to be sorted out before gluing, while crystals size is sufficiently small to fit them onto the array nicely.

This data has been acquire with the MIBETA electronics which was not matched to a

resistance of few megaohms. The new MARE-1 electronics would allow some improvements on the baseline and on rise time as well.

The MIBETA electronics and DAQ

The front-end electronics was operated a few centimetres away from the detectors, at cryogenic temperatures. The cold stage consisted of a common drain silicon JFETs. Ten of these devices were mounted on an aluminium plate, suspended by means of low conductance, tensioned Kevlar fibers inside a copper box. In these test runs the box was mechanically connected to the 4K rod. The signal wires, which connected the detectors terminal to the JFET gates (the other terminals were grounded), were manganine wires (33 μm diameter and 5 cm long) tensioned by CuBe springs. These wires provided electrical connection and negligible thermal conductance. Details regarding the description of MIBETA electronics and the operation of the whole front-end can be found in [132, 133, 134, 135].

The detector load resistence, $R_L = 750$ MΩ, was at the Mixing chamber temperature. This choice allowed to make totally negligible its parallel noise.

The trigger signal was generated at the end of the read-out link, just close to the data acquisition system (DAQ). The trigger threshold is tunable and the trigger signal is optically coupled to the DAQ. The latter was a VXI system composed by a Tektronix 16-channel 16-bit digitizer capable of 100 ks/s per channel (ADC), a Tektronix 16-channel trigger module and an embedded PC controller.

6.1.2 Assembly of MARE-1 detectors

In order to deeply study the best thermal coupling between thermistors and silicon spacers one of the two MARE-1 arrays is equipped with 11 $AgReO_4$ crystals (see figure 6.5). It is a final test before the MARE-1 start . Therefore two different kinds of epoxy resins are tested: five silicon spacers are attached with Araldite Normal and the other six with ST1266 epoxy. ST2850 epoxy is used to glue all the $AgReO_4$ absorbers on the silicon spacers. For this test it has been decided to use Araldit Normal because it is more practical than Araldit Rapid (i.e. the latter takes more time to cure the glue).

The other array is equipped with two thin Sn absorbers, which have dimensions of 500 x 500 x 25 μm^3. The two Sn absorbers, which are directly glued on the SU8 supports of two pixels outside the 6 x 6 matrix, will measure the environmental background below the Re end-point. Both of them are assembled using the set-up described in 5.1.1.

In table 6.4 the crystal masses are listed together with their respective resin.

After this test, the remaining $AgReO_4$ crystals will be attached to the thermistors and the complete measurement of 72 channels will start. Based on the results obtained from the two arrays, we will decide whether or not to extend up to eight the number of arrays.

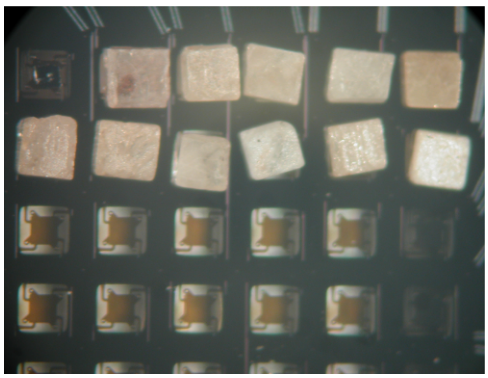

Figure 6.5: The XRS2 array with the first 11 $AgReO_4$ crystals. The crystals are cut in regular shape as precisely as possible.

ARRAY NASA C30302

pixel	absorber	mass [μg]	resine	note
2	$AgReO_4$	517 ± 2	Araldit Normal	Si spacer
3	$AgReO_4$	521 ± 2	Araldit Normal	Si spacer
4	$AgReO_4$	397 ± 1	Araldit Normal	Si spacer
5	$AgReO_4$	535 ± 2	Araldit Normal	Si spacer
6	$AgReO_4$	459 ± 2	Araldit Normal	Si spacer
7	$AgReO_4$	499 ± 1	ST1266	Si spacer
8	$AgReO_4$	457 ± 2	ST1266	Si spacer
9	$AgReO_4$	410 ± 2	ST1266	Si spacer
10	$AgReO_4$	443 ± 2	ST1266	Si spacer
11	$AgReO_4$	453 ± 3	ST1266	Si spacer
12	$AgReO_4$	428 ± 2	ST1266	Si spacer

ARRAY NASA C30204

pixel	absorber	mass [μg]	resine	note
39	Sn	67 ± 3	ST1266	SU8
40	Sn	81 ± 2	ST1266	SU8

Table 6.4: Listed are the absorbers glued onto the two MARE-1 arrays together with their respective resin. The other pixels are empty.

6.2 Test of the cold buffer stage

The cold buffer stage was tested in a dedicated cool-down. The thermal bath was at the nitrogen temperature and the JFETs temperature spamed from 90 K to 135 K. All the gates were connected to resistances with a negligible Ohmic value. All the 72 channels were good. Figure 6.6 shows the input noise of two different front-end channels. The JFETs were at 120 K.

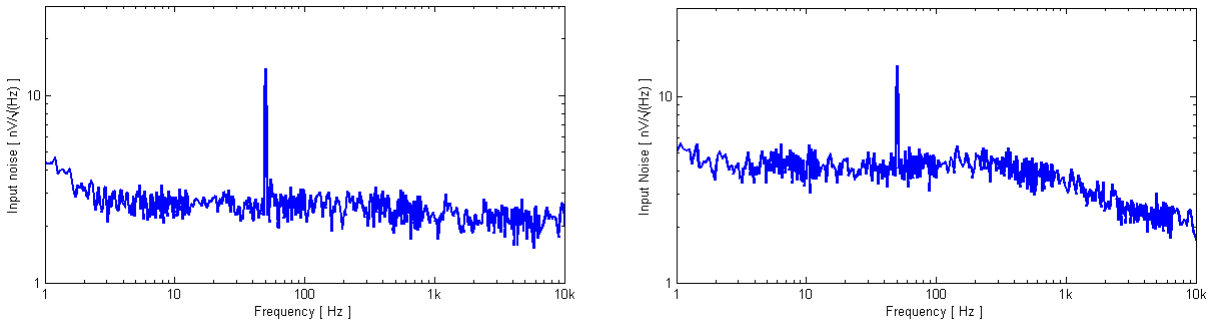

Figure 6.6: Series noise of channel 7 (right panel) and channel 8 (left panel).

In this condition the white noise measured was about 3 nV/Hz$^{1/2}$ and 5 nV/Hz$^{1/2}$ for the channel 7 and 8, respectevely . This Johnson noise has been primarily due to the wiring between the cold electronic and the amplifier stage. The worsening in the performance was mainly observable in the low frequency region of the spectrum. In fact, at 1 Hz the noise was about 4 nV/Hz$^{1/2}$ for channel 7 and 6 nV/Hz$^{1/2}$ for channel 8.

The noise performance at low frequency of JFETs is strongly dependent on temperature. This behaviour is displayed in figure 6.7. In the left panel the JFETs was at about 135 K and in the right panel they were at around 100 K. The white noise is less sensitive to temperature, unless it is below 90 K, where freeze-out from donor dopants starts to take effect. A Lorentzian is visible in the right panel of figure 6.7 that spans to large frequency. Although not at the optimum, the noise we have at 120 K is adequate for our set-up and we will run in this condition in MARE-1.

6.3 Thermal analysis of the MARE-1 cryogenic set-up

A prior work has been carried out in order to study and optimize the MARE-1 cryogenic set-up. Therefore, in this section the thermal analysis of the cryogenic set-up is reported together with the new improvements from time to time added to the original design presented in chapter 5.

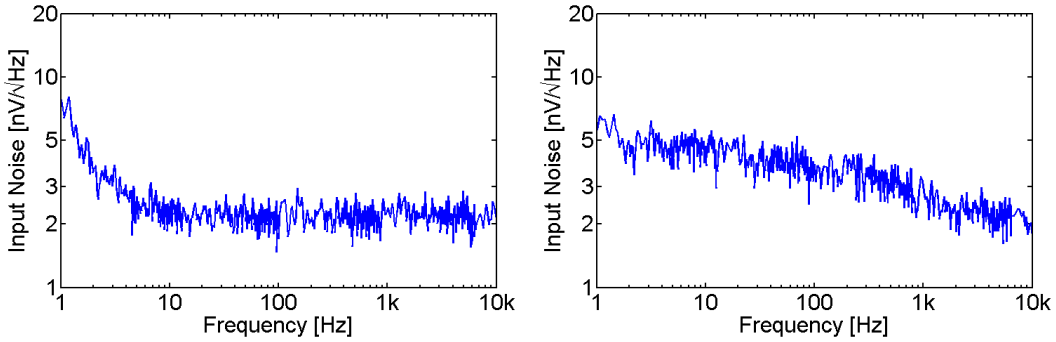

Figure 6.7: Left Panel: series noise of one channel with JFET at 130 K; the white noise measured is of 2 $nV/Hz^{1/2}$ and the noise is about 5 $nV/Hz^{1/2}$ at 1 Hz. Right Panel: series noise of one channel with JFET at 100 K.

6.3.1 Thermalization of JFET box

RUN 0

Since its first installation the cryogenic set-up of MARE-1 has presented several structural and thermal problems. One of the first technical hitch concerning the cryogenic set-up occured during the assembly of the first MARE-1 run (RUN 0). In fact, there was an unexpected failure of the Al microbridges inside the JFET box. This failure was probably due to an excessive mechanical stress of these delicate devices, despite of their mechanical stability had been tested in the past [129]. Observing them at the microscope, little micro-fractures were visible. As a consequence, the Al microbridges were replaced with Al/Si 1% bonding wires with a diameter of 25 μm and a length of 1 cm. The power flows through a single bonding wire was 0.36 mW. This power was still higher than the one trough a single Al microbridge (0.08 mW).

During the RUN 0 another big problem relating to the thermalization of the JFET box came out: when we tried to warm up the JFETs at their working temperature (120 K), the temperature of the detector holder and, as a consequence, the temperature of the Mixing Chamber increased while it was impossible to reach 120 K inside the JFET box.

Since the experiment was at a pressure less than $< 10^{-7}$ mbar, the only ways in which the heat can diffuse are trough thermal contacts and thermal radiation. Therefore, tasks designed to contain these contributions have been performed.

In order to contain the heat flow from the JFET to the parts at 4 K the Al/Si 1% bonding wires has been replaced with other thinner and longer. The length of the new Al/Si 1% bonding wires is 1.3 cm and the diameter is 17.5 μm. In this way, a factor 3

on the thermal conductivity has been gained (i.e. the new power through a single wires is now 0.13 mW). Besides, only 40 JFETs inside the box are connected with the bonding wires. Considering all these new improvements and the contribution due to the presence of the Vespel rods, there has been an halving of the power exchanged between the PCB at 120 K and the 4 K parts.

The radiative heat transfer between two objects at different temperatures T_1 and T_2 is proportional to $\epsilon(T_1^4 - T_2^4)$, where ϵ is the emissivity. This latest quantity takes into account the deviation of the behaviour of a real object from black body. Consequently, for our system composed by a PCB at 120 K inside a box at 4 K the radiation is not completely negligible, despite of the walls of the box are gold plated. Simulating an additional thermal conductance between the JFET PCB and the box, the thermal radiation causes an extra power on the wires, which connect the JFET gates at the detectors. In order to minimize this problem the walls of the JFET box are covered with several layers of Aluminium Mylar.

We have also considered the possibility that the nylon wire for the calibration source, which has one end at room temperature and the other at 4 K, may touch the Mixing Chamber plate or the detector holder. To avoid this eventuality a Teflon cone has been added in the hole trough which the nylon wire slides. In addition, to better anchor the nylon wire at 4 K two thermalization stages are placed along the wire path, one is located on the 4K plate and the other on the copper rod at height of the Mixing Chamber.

RUN 1

To test the new thermalization of the JFET box a dedicated run was carried out. Therefore five silicon diodes thermometers were placed in strategic positions separated by interfaces (see figure 6.8).

Changing the power dissipated by the heater soldered on the JFET PCB the diode temperatures together with the temperature of PCB itself were recorded. The results are shown in table 6.5.

Power [mW]	**Pt-100**	**T_1 [K]**	**T_2 [K]**	**T_3 [K]**	**T_4 [K]**	**T_5 [K]**
70	120.3 ± 0.3	6.4	6.2	6.2	5.9	5.7
80	125.9 ± 0.9	6.4	6.3	6.2	5.8	5.6
180	195.4 ± 0.5	7.6	6.8	6.6	6.4	6.2

Table 6.5: Temperatures recorded by five silicon diodes and by one Pt-100 sensor soldered on the JFET PCB. The error on the temperatures measured by the five diodes is 0.1 K.

Dissipating 70 mW the optimal working temperature is reached and the gradient temperature between JFET box and the copper rod is of the order of 0.7 K, that is a reasonable

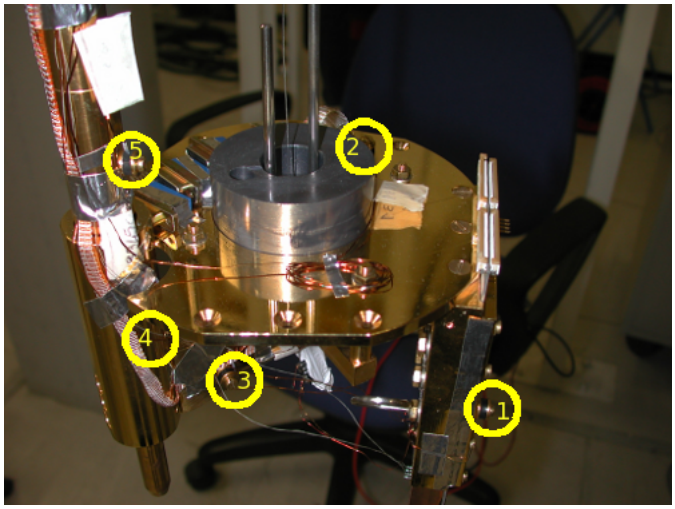

Figure 6.8: The position of the five diodes which monitor the temperature of the several interfaces.

value.

As the link between the JFET box and the cryostat copper rod consists of different interfaces with small area, it has been increased the thermal link between them using a copper braid. One end of the braid is screwed on the 4 K copper rod and the other on the holder of the JFET box. The RRR [1] of this copper is 131, while the RRR of the copper used to build the detector holder and JFET holder is about 40.

In literature one can find that the thermal conductivity of a copper characterized by an RRR equal to 100 is $k(T) = 1.32T$ between 0 K and 4 K [125], while the thermal conductivity of a copper characterized by an RRR equal to 40 is $k(T) = 0.53 \pm 0.14T$ between 30 mK and 150 mK [136].

6.3.2 RUN 2

As soon as the problems concerning the Al microbridges and the thermalization of the JFET box have been solved, the NASA array with ten crystals was reinstalled in the cryostat together with its readout electronics.

During the cool-down of the RUN 2 there was another technical hitch: the Ti microbridges were broken when the system reached the helium liquid temperature. The unexpected failure of the Ti microbridges was probably due to a thermal stress. It has been thought to use Stainless Steel wires in replacement of the broken Ti microbridges to avoid further troubles. In fact, the Stainless Steel wires, which have a diameter of 50 μm and a length of 2 cm, are more robust than Ti microbridges. These wires are soldered on

[1] *RRR* is the Residual Resistivity Ratio and it is very often given as a measure of the purity of a metal. This is the ratio of the electrical conductivity at the boiling point of liquid helium to the electrical conductivity at room temperature.

a dedicate PCB, which is specifically projected to house them. Figure 6.9 shows the new Stainless Steel wires.

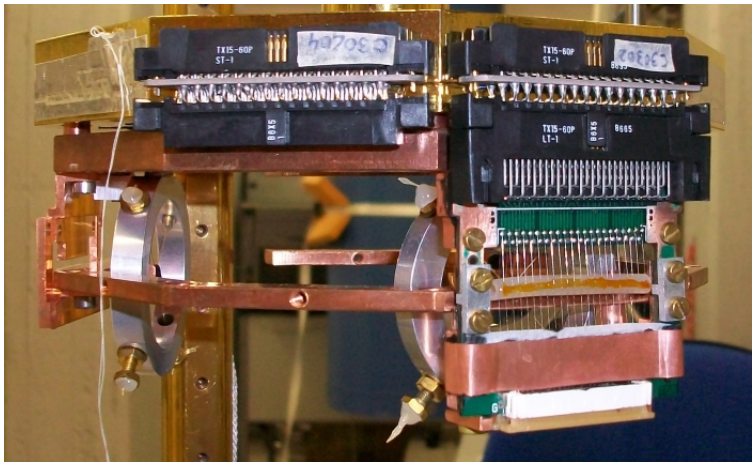

Figure 6.9: The new PCB with the Stainless Steel wires, which have replaced the Ti microbridges.

A Silicon tube, on where the Stainless Steel wires are glued with Varnish, is placed between the two lines of wires to avoid an excessive microphonic noise and short circuits.

The thermal conductivity of the Stainless Steel wires is very low below 10 K. The heat flow trough a single wire is around 10 nW. Subsequently, these wires have been tested during several cool-downs and they have shown their capability to resist at different thermal cycles without breaking.

6.3.3 Thermalization of the detector ceramic I

Different cool-downs were devoted to find the best thermalization of the detector ceramic where the arrays are glued. During this tests only the array equipped with Sn absorbers was installed in the cryostat and only a room temperature amplifier stage was used as read-out. Not installing the MARE-1 cold buffer stage meant to neglect the power contribution due to the wires which connect the output of the detectors at 35 mK to the input of the cold electronics at 4 K.

The electronics at room temperature consisted of a preamplifier stage with a gain of 196, a Bessel filter with a gain of 1.95 and an amplifier stage with adjustable gain. The gain of this last stage had been set to 10. The bias circuit was powered with a 9V battery and it was provided with two load resistances (500 MΩ each).

In order to monitor the detector holder temperature a calibrated NTD thermistor was screwed on it.

RUN 3

The first run was dedicated to determine the detector holder temperature and the array temperature using the original design of the MARE-1 experiment. The ceramic array was screwed on the detector holder and the detector holder was screwed on the Mixing Chamber plate. This run gave us the zero point. With this configuration the detector holder was at 33 mK and the array was at 150 mK, temperature measured with one of the two pixels embedded in the array silicon wafer (pixel number 38). We would like to point out that the optimal working temperature of this bolometer is 85 mK. This temperature gradient could be explained in the following way: the link between the ceramic and the holder was too weak for the incident power (i.e. radiation). In fact the ceramic was held by a single screw that could not be too tight, given the extreme fragility of the ceramic.

RUN 4

In RUN 4 a copper bridge was added to increase the thermal link between the ceramic and the detector holder. On one side it was glued on the ceramic with ST2850 and on the other side it was screwed on the detector holder. A silicon thermistor (500 x 500 μm^2) was also glued on the ceramic to monitor its temperature.

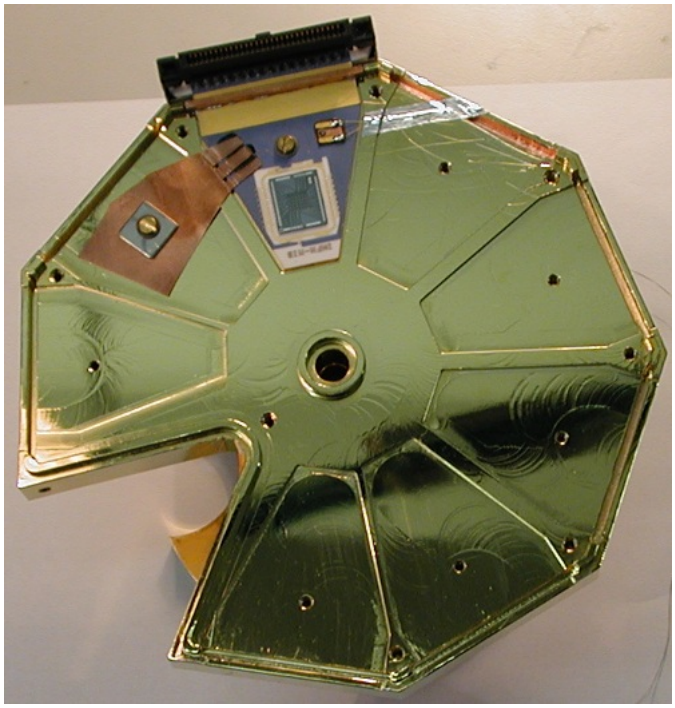

Figure 6.10: In order to increase the thermal link between the ceramic and the detector holder a copper bridge was used. On the right of the ceramic one can see the silicon thermistor used to monitor the ceramic temperature.

With this configuration the temperature of the ceramic was 70 mK, the detector holder was obviously at the same temperature as the previous run and the array was at 133 mK (temperature of the embedded pixel 38). Nevertheless, the improvement on the detector temperature was not enough and the main origin of the problem was to be looked for elsewhere.

RUN 5

It has been thought that the thermal radiation coming from the surrounding parts at 4 K could contribute to the increase of the detectors temperature. For that reason the Roman lead shield for the calibration source was temporally removed. This shielding, having a very high mass and not having a strong reference thermal constraint, could be at higher temperature and, consequently, it could heat the detectors by radiation. The black connector of the detectors ceramic was covered with three layers of Al mylar in order to protect the detectors as much as possible from the thermal radiation > 4 K.

Finally, a ^{57}Co source was added about 14 cm away from the detectors. The activity of this source is 500 kBq. ^{57}Co decays by electron capture to ^{57}Fe, emitting two gamma rays at 122 and 136 keV with a branching ratio of 86% and 11%, respectively. Taking into account the geometrical efficiency (i.e. distance detector-source and detector area=2.5x10^{-7} m^2) and the interaction efficiency of photons of energy around 100 keV, the activity of this source on a single Sn absorber is 0.005 Hz.

With this new configuration the detector holder was at 21 mK, the ceramic at 27 mK and the array at 62 mK. Setting the bias voltage at 300 mV, the pixel equipped with Sn absorber reached the working temperature of around 85 mK. In this condition the spectrum, shown in figure 6.11, was acquired with a National Instrument USB acquisition card.

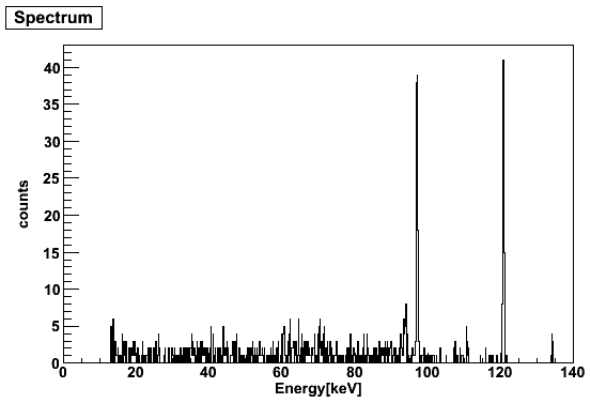

Figure 6.11: RUN 5: The spectrum of pixel 40 in the presence of ^{57}Co source ($T_{bol} \simeq 85$ mK, $R_L = 2\times100$ MΩ). This spectrum shows the ^{57}Co peaks at 122 keV and 136 keV together with the escape peak resulting from the interaction of the ^{57}Co gamma rays with Sn at 97 keV.

The spectrum presents two visible peaks: one at 122 keV and the other at 97 keV. This latest peak is an escape peak resulting from the interaction of the ^{57}Co gamma rays with Sn. The escape peak, originating from the energy difference between incoming Co rays and the escaping Sn Kα X-rays, has a FWHM resolution of 850 eV, while the FWHM resolution of the peak at 122 keV is 1.06 keV. The baseline width, obtained by studying the noise spectrum in frequency domain, is 209 eV and the ratio ΔV/122 keV is 20 ± 4 μV/keV. The rise time is 3.12 ± 0.09 ms, while the decay time is 54.0 ± 0.1 ms. The noise spectrum in frequency domain is shown in figure 6.12.

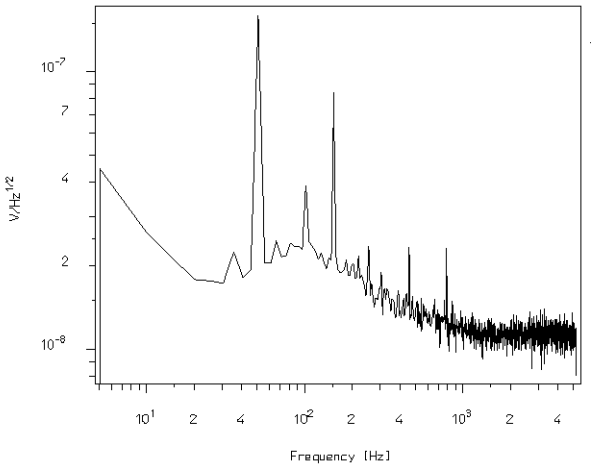

Figure 6.12: RUN 5: Noise spectrum in frequency domain of pixel 40. The Bessel cutoff frequency is 216 Hz.

Although the pixels reached the working temperature, they were at a temperature of about 30 mK higher than the ceramic temperature. Besides, we want to stress that the components of the set-up which introduce additional power on the detectors are still lacking in this run.

6.3.4 RUN with the MARE-1 cold electronics

After these improvements three different cool-downs were scheduled to monitor the array temperatures in presence of most cryogenic components. As a consequence, the cold buffer stage together its supports was reintroduced in the cryostat, but not the lead shield.

RUN 6

In RUN 6 the array with 10 crystals of $AgReO_4$ and its read-out electronics was reinstalled in the cryostat, obviously taking into account the new improvements made to the set-up (i.e. Al mylar to protect the detector from the thermal radiation and the copper bridge to increase the thermal link between the ceramic and the detector). Also for this array a copper bridge was introduced (see figure 6.13), while the Roman Lead shield and the calibration source were still missing. It was the first time that the Stainless Steel wires described in section 6.3.2 were tested during a complete cool-down.

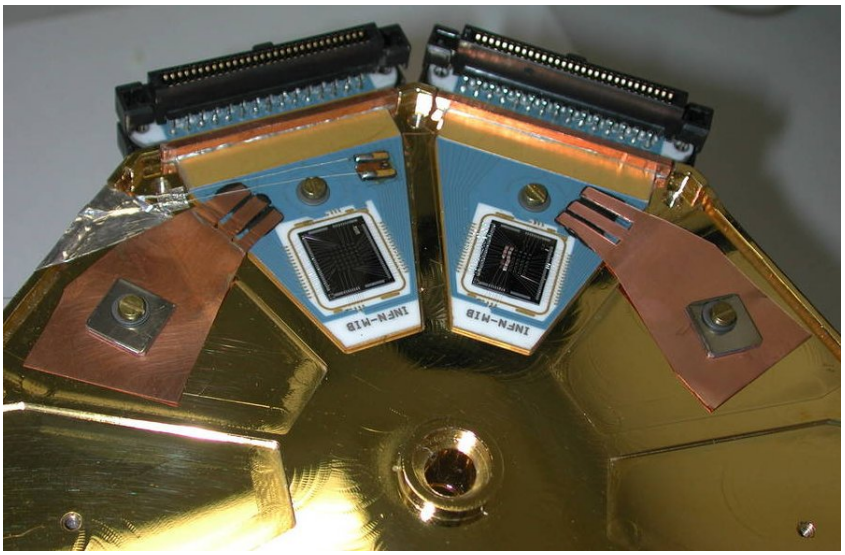

Figure 6.13: The two MARE-1 arrays with Copper bridges to increase the thermal link between the ceramic and the array.

The temperatures of the array C30204 were recorded in three different situations: JFETs cold, JFETs warmed up by the only heater, JFETs warmed up by the heater and their power (see table 6.6). These temperature were monitored using the electronics at room temperature. The temperatures of the array with $AgReO_4$ absorbers (i.e. array NASA C30302) were not recorded in this run.

Results in table 6.6 shown that the temperature difference between array and holder is about 30 mK and it increases when the JFETs were warmed up . The detector temperature is not sensitive by the way in which the PCB is warmed up. With this cool-down the

ARRAY NASA C30204 - Sn

Pixel	$\mathbf{T}_{EF}$ **[K]**	$\mathbf{T}_h$ **[mK]** ±1 mK	$\mathbf{V}_{bias}$ **[mV]** ±1 mV	$\mathbf{T}_{bol}$ **[mK]** ±1 mK	$\mathbf{T}_{cer}$ **[mK]** ±1 mK	**Note**
38	4.2	29	53	60	43	
40	4.2	29	51	63	43	
38	110	36	48	68	53	Heater
40	110	36	53	71	53	Heater
38	122	37	50	70	54	Heater + JFET
40	122	37	56	74	54	Heater + JFET

Table 6.6: RUN 6: temperatures of the C30204 array with the JFET PCB cold, warmed up trough the heater and warmed up through heater and the power dissipated by the JFET are recorded. $\mathbf{T}_{EF}$, $\mathbf{T}_h$, $\mathbf{T}_{bol}$ and $\mathbf{T}_{cer}$ are the JFET temperature, the detector holder temperature, the array temperature and the ceramic temperature respectively, while $\mathbf{V}_{bias}$ is the detector bias voltage. Pixel 38 is a pixel embedded in the silicon wafer while pixel 40 is a suspeded one. The temperature difference between array and holder is about 30 mK and it increases when the JFETs were warmed up. The detector temperature is not sensitive to the way in which the PCB is warmed up.

mechanical stability of Stainless Steel wires was tested. The Stainless Steel wires were not broken during the assembly of the entire cryogenic set-up and they have resisted to the thermal cycle. Furthermore they haven't touch each other.

RUN 7

The set-up of this run is the same as the one of RUN 6, except for the presence of two radioactive sources: ^{57}Co and ^{55}Fe. Since the Roman Lead shield was still lacking, an apposite Al holder was added to the set-up to hold the ^{55}Fe calibration source.

The temperatures of an embedded pixel (i.e. pixel 38) and of a suspended one (i.e. pixel 39) of the array equipped with Sn absorbers (array NASA C30204) were measured with cold and warm JFETs. For the array equipped with $AgReO_4$ absorbers (array NASA C30302) the temperatures of an embedded pixel (i.e. pixel 38) and of a suspended one (i.e. pixel 9) were recorded only in presence of warm JFETs. The obtained results are listened in table 6.7.

The pixels were at a temperature 30 mK higher than the holder and this difference increased of about 10 mK when the JFETs were warmed up.

During this run spectra relative of pixels with absorbers were acquired for both arrays. The bias voltage of pixel 9 equipped with $AgReO_4$ was set at 70 mV and it was read-out by the MARE-1 electronics, while the bias voltage of pixel 38 equipped with Sn was set at 16 mV and it was read-out by the electronics at room temperature.

Figure 6.14 shows the spectrum of pixel 38 at a working temperature of about 85 mK.

ARRAY NASA C30204 - Sn

Pixel	$\mathbf{T}_{JFET}$ **[K]**	$\mathbf{T}_{holder}$ **[mK]** ± 1 mK	$\mathbf{V}_{bias}$ **[mV]** ± 1 mV	$\mathbf{T}_{bol}$ **[mK]** ± 1 mK
38	4.2	32	21	61
39	4.2	32	14	63
38	119	40	33	77
39	119	40	16	80

ARRAY NASA C30302 - $AgReO_4$

Pixel	$\mathbf{T}_{JFET}$ **[K]**	$\mathbf{T}_{holder}$ **[mK]** ± 1 mK	$\mathbf{V}_{bias}$ **[mV]** ± 0.1 mV	$\mathbf{T}_{bol}$ **[mK]** ± 1 mK
38	119	40	2.0	80
9	119	40	2.0	93

Table 6.7: RUN 7: Temperatures of the two arrays at varying of the JFET temperature are listed. Obviously, the embedded pixel (pixel 38) is colder than the suspended ones. The array read-out by the cold buffer stage is slightly warmer.

At low energy ($\sim$ 5.9 keV) one can see the Mn K_α line with an energy resolution of 508±22 eV. At 122 keV and 136 keV there are the peaks due to the presence of the ^{57}Co source. In addition, the escape peaks resulting from the interaction of Co γ-rays with Sn are visible (Sn K_α = 25.3 keV, Sn K_β = 28.5 keV). The baseline value, obtained by studying the noise spectrum in frequency domain, is 182 eV. The rise time is 11.1±0.5 μs, while the decay time is 74±1 ms.

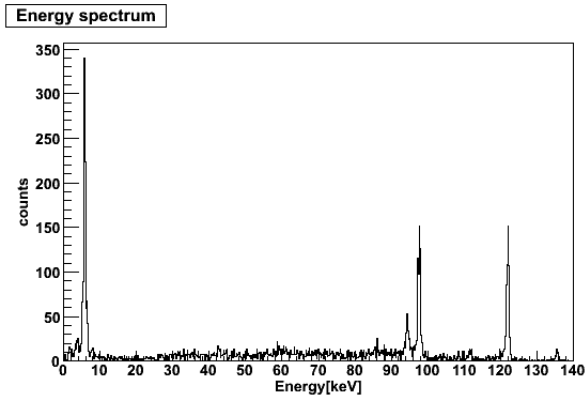

Figure 6.14: Spectrum of pixel 38 acquired during RUN 7 ($T_{bol} \simeq$ 85 mK, R_L = 2×100 MΩ). At low energy ($\sim$ 5.9 keV) there is the Mn K_α line, while at high energy (122 keV and 136 keV) there are the peaks due to the presence of the ^{57}Co source. In addition, the escape peaks resulting from the interaction of Co γ-rays with Sn are visible (Sn K_α = 25.3 keV, Sn K_β = 28.5 keV).

Figure 6.15 shows the spectrum of pixel 9 at a working temperature of about 108 mK. This spectrum is characterized by several escape peaks resulting from the interaction between Co γ-rays with Re and Ag atoms in the $AgReO_4$ absorber (the probability of a photoelectric effect on O is much lower). Obviously, the Co peaks at 122 and 136 keV are well visible. The energy resolution of the peak at 5.9 keV is 427±11 eV and the baseline value, obtained by studying the noise spectrum in frequency domain, is 370 eV. The rise time and the decay time are 543±72 μs and 20±1 ms, respectively. The ratio ΔV/(6 keV) is 17.7±0.5 μV/(6 keV). The noise spectrum in frequence domain is diplayed in figure 6.16

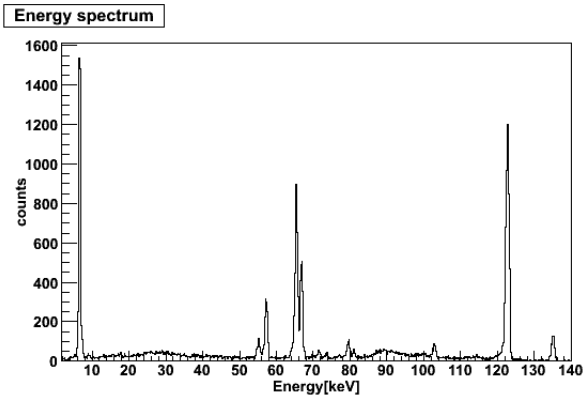

Figure 6.15: Spectrum of pixel 9 acquired during RUN 7 ($T_{bol} \simeq 108$ mK, $R_L = 50$ MΩ). The spectrum presents the peaks due to the presence of the calibrated source, ^{57}Co and ^{55}Fe, together with several escape peaks resulting from the interaction between Co γ-rays with Re and Ag atoms in the $AgReO_4$ absorber (the probability of a photoelectric effect on O is much lower).

For both spectra displayed in figures 6.14 and 6.15 the peak at lower energy is the Mn Kα peak. It was not possible to see the peaks due to the presence of the fluorescence source because the detectors were still at too high base temperature.

The large difference between the two baseline values is due to the different electronics used to read-out the detectors. In fact, the spectrum of pixel 38 was acquired with only the amplifier stage at room temperature, while the spectrum of pixel 9 was acquired with MARE-1 electronics with JFET at 120 K.

RUN 8

The results of RUN 5 have shown that working on shielding thermal radiation and on increasing the thermal link between the detector ceramic and the holder was the right direction. It has been thought to increase the thermal link between the JFETs holder and the part suspended by the three Kevlar crosses. As a consequence, a copper braid was added as a thermal link. To monitor the temperature of the suspended part a calibrated cernox thermometer was screwed on it. Also in this run the temperatures of the both arrays were monitored (see table 6.8).

ARRAY NASA C30204 - Sn

Pixel	$\mathbf{T}_{JFET}$ **[K]**	$\mathbf{T}_{holder}$ **[mK]** ± 1 mK	$\mathbf{V}_{bias}$ **[mV]** ± 0.1 mV	$\mathbf{T}_{bol}$ **[mK]** ± 1 mK	$\mathbf{T}_{cernox}$ **[K]**	**Note**
38	4.2	28	21.4	60	4.5	
39	4.2	28	11.1	68	4.5	
38	92	30	11.2	66	5	H
39	92	30	11.2	69	5	H
38	114	34	21.5	75	5.8	H
39	114	34	21.4	83	5.8	H
38	120	34	12.5	77	5.8	H + JFET
39	120	34	13.8	86	5.8	H + JFET

ARRAY NASA C30302 - $AgRe0_4$

Pixel	$\mathbf{T}_{JFET}$ **[K]**	$\mathbf{T}_{holder}$ **[mK]** ± 1 mK	$\mathbf{V}_{bias}$ **[mV]** ± 0.1 mV	$\mathbf{T}_{bol}$ **[mK]** ± 1 mK	$\mathbf{T}_{cernox}$ **[K]**	**Note**
38	120	34	4.0	75	5.8	H + JFET
9	120	34	4.0	87	5.8	H + JFET

Table 6.8: RUN 8: The temperatures of the two arrays at varying of the JFETs temperature are listed. H stands for heater. Pixel 38 is an embedded pixel, while the others (i.e. pixel 9 and pixel 39) are suspended. T_{cernox} is the temperature of the copper piece suspended by the three Kevlar crosses. This temperature is measured with a calibrated cernox thermometer.

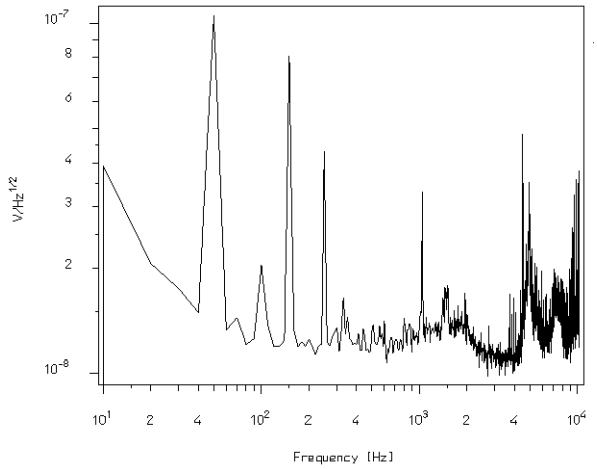

Figure 6.16: RUN 7: Noise spectrum in frequence domain of pixel 9.

During this run no spectrum was acquired. Despite the part suspended by the Kevlar crosses was at the same temperature of the JFETs holder, the difference between the holder and the detector was still 30 mK. Therefore, the main cause of this effect must be somewhere else researched.

There are different possible explanations of this temperature gradient. It could be explained hypothesising the presence of a further thermal radiation at 4 K. Another possible explanation may be that the Stainless Steel wires are too conductive. Last but not least, the gradient temperature could be connected to a still too weak thermalization of the detector ceramic.

6.3.5 Thermalization of the detector ceramic II

As a result, we decided to remove the cold buffer stage and to only mount the detector holder, as the RUN 3, RUN 4 and RUN 5. Therefore, three cool-downs were dedicated to understand the problem connected to a too high temperature of the array.

RUN 10

In RUN 10 a new solution was studied in order to increase the thermal link between the array and the ceramic. As a consequence, four ceramics without array were added in the detector holder:

– a broken ceramic without any parts outside the detector holder to monitor the ceramic temperature neglecting the radiation contribution.

– a ceramic to test Au bonding wires (50 μm of diameter and 1 cm long) as an additional thermal link between the detector holder and the ceramic itself. The number of bonding wires was around 50.

– a ceramic with a black connector like the array ceramic to test Au bonding wires (50 μm of diameter and 1 cm long) as an additional thermal link between the detector holder and the ceramic itself. The number of bonding wires was around 50.

– a ceramic with a thin layer of vacuum grease on its bottom to increase the contact surface between the detector holder and the ceramic itself.

The copper bridge, used in the previous run to increase the thermal link between the array ceramic and the holder, was removed and replaced by Au bonding wires.

Furthermore, the detector holder hosted up the C30204 NASA array, the one equipped with two Sn absorbers. Also for this array the thermal link between the ceramic and the holder was increased using Au bonding wires. All the black connectors were covered by three layers of Al mylar as a shield against the thermal radiation. The temperature of the four ceramics was measured by a silicon thermistor, whose calibration was well known ($\gamma = 0.5$, T_0=1.122 K and $R_0 = 2608.7\Omega$), while the temperature of the NASA array were monitored using the electronics at room temperature. The results obtained are listed in table 6.9 and 6.10.

broken	**bonding**	**bonding + connector**	**grease**	**holder**
29 ± 1 mK	39 ± 1 mK	43 ± 1 mK	51 ± 1 mK	28 ± 1 mK

Table 6.9: RUN 10: the base temperature of the four ceramics.

The Au bonding wires were without doubt a good choice, while the vacuum grease was not a good choice.

embedded pixel	**pixel with Sn**	**bare pixel**	**holder**
53 ± 1 mK	58 ± 1 mK	60 ± 1 mK	28 ± 1 mK

Table 6.10: RUN 10: the base temperature of an embedded pixel, a pixel equipped with Sn absorber and a bare pixel are listed together with the detector holder temperature.

Despite the presence of the Au bonding wires the pixel temperatures were still too hot. For that reason in the next cool-downs the number of the Au bonding wires will be

increased.

RUN 11

In RUN 11 we increased the number of Au bonding wires to better anchor the array itself to the ceramic and we added a copper braid, glued on the black connector and with an end screwed on the detector holder, to have a better thermalization of the connector.

The experimental set-up of this run was the same as the previous one except for the following changes: a bare ceramic to set the zero point, a Silicon thermistor, soldered on the black connector, to monitor its temperature and the number of layers of Al mylar was reduced from three to one. In fact, it has been thought that the Al mylar layers, which were quite bulky, could touch the Still shield at 600 mK. The ceramic temperatures together with the detector holder temperature are listed in table 6.11, while the array temperatures together with the detector holder temperature in table 6.12.

bare	**broken**	**bonding**	**bonding + connector + braid**	**holder**
43 ± 1 mK	31 ± 1 mK	41 ± 1 mK	46 ± 1 mK	27 ± 1 mK

Table 6.11: RUN 11: the base temperature of the four ceramics together with the detector holder temperature.

The presence of the copper braid glued on the black connector was irrelevant on the temperature of the ceramic, as a consequence it will be removed in the next cool-downs.

embedded pixel	**pixel with Sn**	**bare pixel**	**holder**
64 ± 1 mK	74 ± 1 mK	76 ± 1 mK	27 ± 1 mK

Table 6.12: RUN 11: the base temperature of an embedded pixel, a pixel equipped with Sn absorber and a bare pixel are listed together with the detector holder temperature.

In both cases the decreasing of the number of the Al mylar layers from three to one was almost compensated by the increasing of the number of Au bonding wires. These results have shown that the thermal radiation has been a big problem in our experiment.

RUN 12

In this run the number of Au bonding wires was furthermore increased and other Au bonding wires, whose diameter was 25 μm, were used to better anchor the array itself to the ceramic. In fact, more than 40 of these were added. In this run there was only one layer of Al mylar as the RUN 11.

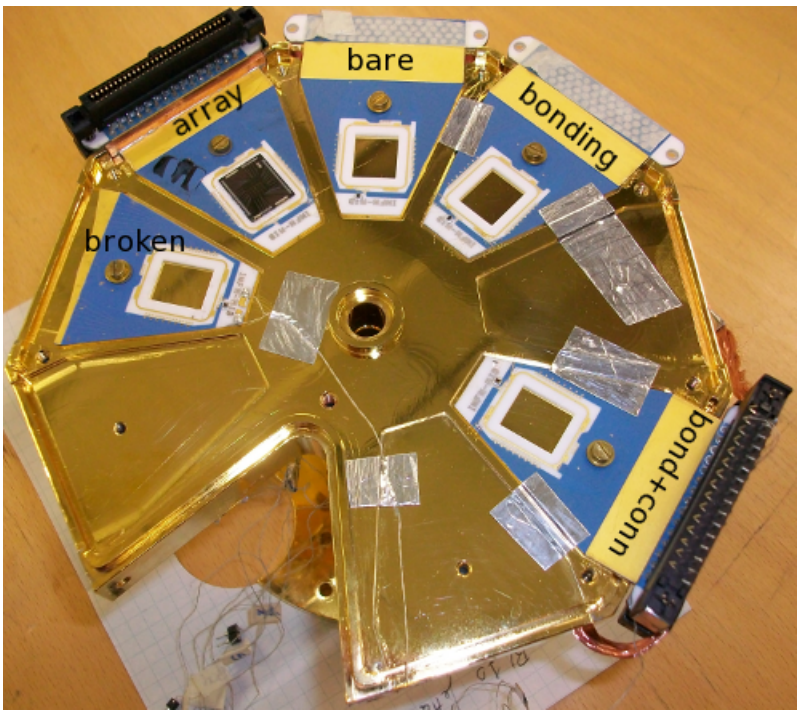

Figure 6.17: The new four ceramics screwed on the detector holder together with the array ceramic.

Figure 6.17 shows the new four ceramics together with the array.
The load curves of these thermistors are shown in figure 6.18.

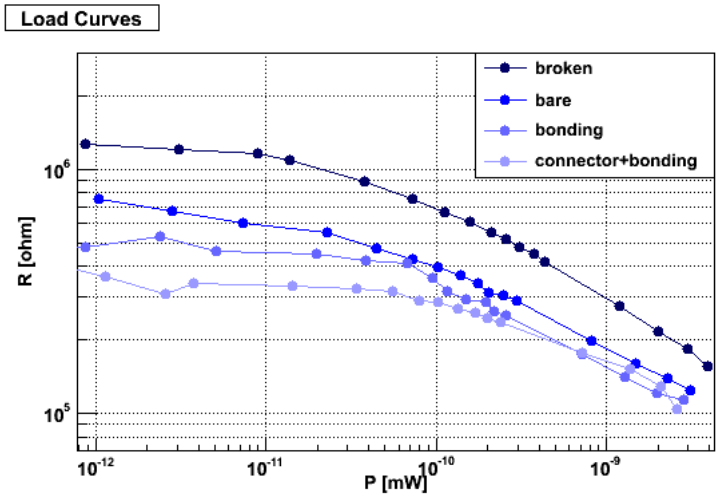

Figure 6.18: RUN 12. Load curves of the four thermistors attached on to the four ceramics recorded on 02/22/2011.

The base temperatures of the four ceramics are reported in table 6.13.
The still power was set to 5 mW and it was given by a battery. The Oxford diagnostic

date	broken	bare	bonding	bonding + connector	holder
02/22/2011	30 ± 1 mK	36 ± 1 mK	41 ± 1 mK	44 ± 2 mK	27 ± 1 mK
02/23/2011	30 ± 1 mK	35 ± 1 mK	35 ± 1 mK	38 ± 1 mK	23 ± 1 mK

Table 6.13: RUN 12: the base temperature of the four ceramics.

was disconnected in order to avoid any interference. In this configuration the temperature measured on the black connector was 100 mK.

The temperature of the array was monitored one and two days after the system had reached the base temperature. For the array the temperature of a pixel equipped with Sn, of an embedded pixel and of a pixel without any absorber were recorded (see table 6.14). The load curves of these pixels are represented in figure 6.19.

date	embedded pixel	pixel with Sn	bare pixel	holder
02/22/2011	57 ± 1 mK	71 ± 1 mK	65 ± 1 mK	27 ± 1 mK
02/23/2011	52 ± 1 mK	65 ± 1 mK	63 ± 1 mK	23 ± 1 mK

Table 6.14: RUN 12: the base temperature of an embedded pixel, a pixel equipped with Sn absorber and a bare pixel are listed together with the detector holder temperature.

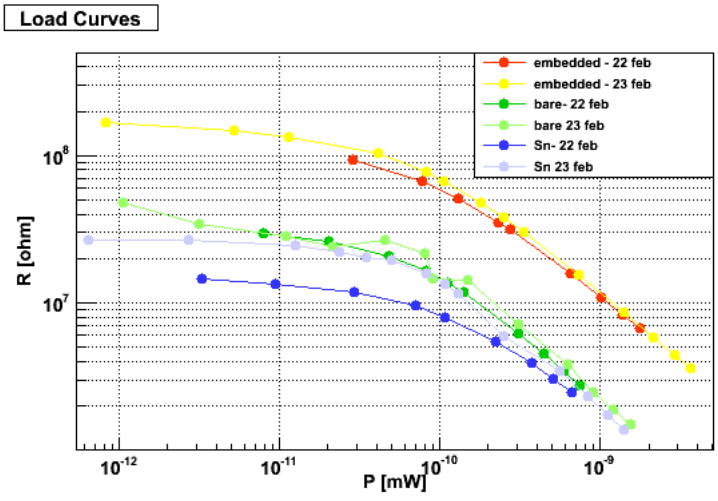

Figure 6.19: RUN 12. Load curves of the three pixels of the array recorded in two different days.

The further increase in the number of Au bonding wires between the detector holder and the array ceramic and the addition of Au bonding wires between the array and the ceramic has compensated the presence of only one Al mylar layer.

In conclusion, introducing Au bonding wires as thermal link there has been a decisive improvement respect to RUN 5. In fact, in RUN 5 the embedded pixel was at 62 mK.

The Al mylar, shielding the black connector from thermal radiation, gave a significant contribution in reaching our purpose. But it was so impractical that it was decided to project a new thermal shield. As a first test we decided to schedule a new run with a totally closed copper shield screwed on the mixing chamber plate.

RUN 13

A new cooldown was dedicated to test the new thermal shield shown in figure 6.20.

Figure 6.20: The copper shield screwed to the mixing chamber plate.

The ceramic screwed on the detector holder were the same as the previous run (i.e. RUN 12). Also in this run the temperatures of the same three pixels of the MARE-1 array were monitored. In table 6.15 the temperatures of the three pixels are listed, while in figure 6.21 their load curves are displayed.

date	**embedded pixel**	**pixel with Sn**	**bare pixel**	**holder**
04/05/2011	46 ± 1 mK	47 ± 1 mK	45 ± 1 mK	22 ± 1 mK

Table 6.15: RUN 13: the base temperature of an embedded pixel, a pixel equipped with Sn absorber and a bare pixel are listed together with the detector holder temperature.

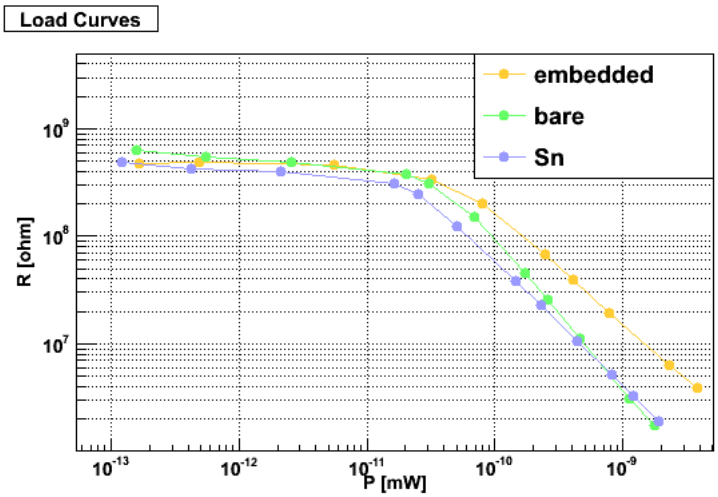

Figure 6.21: RUN 13. Load curves of the three pixels of the array.

Also in this run the still power was set to 5 mW and the Oxford diagnostic was disconnected in order to avoid any interference.

Thanks to this thermal shield the array was at 46 mK, only 24 mK higher than the holder. With it our purpose was reached. Therefore, it has been added to the experimental set-up as essential part.

RUN 14

Subsequently, the copper shield, tested earlier, was adapted to match with the original cryogenic set-up of MARE-1. In particular, two holes were made on its bottom: one for the calibration system and the other one for the JFET connections. A latest cool-down was devoted to test the adapted copper shield in the presence of the entire MARE-1 cryogenic set-up. The array equipped with $AgReO_4$ absorbers was reintroduced and also the JFET box and its holder, but the cold buffer stage was not powered. The array with Sn absorbers was read-out by the amplifier at room temperature (i.e the one used in the previous cool-downs). The thermal link between the array and the ceramic and between the ceramic and the detector holder was increased using Au bonding wires.

The results are listed in table 6.16 and figure 6.22 shows the load curves.

date	embedded pixel	pixel with Sn	bare pixel	holder
05/10/2011	50 ± 1 mK	51 ± 1 mK	48 ± 1 mK	28 ± 1 mK

Table 6.16: RUN 14: the base temperature of an embedded pixel, a pixel equipped with Sn absorber and a bare pixel of the array NASA C30204 are listed together with the detector holder temperature.

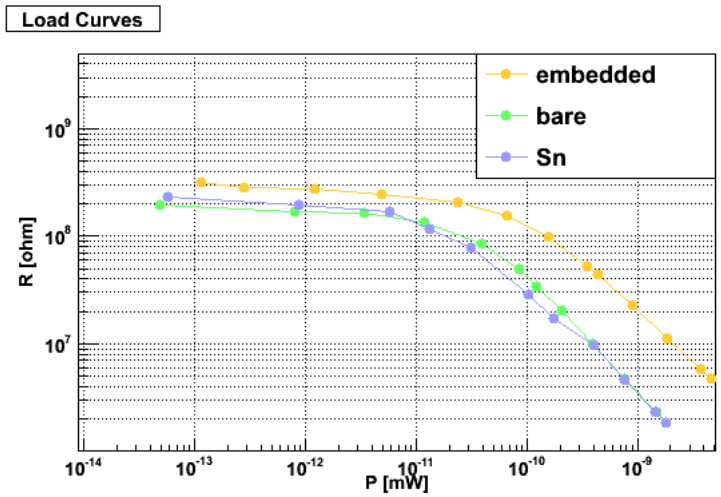

Figure 6.22: RUN 14: Load curves of the three pixels of the array with Sn.

The presence of different parts at 4 K has led to an higher temperature of the array compared to the previous run, but this increase was limited.

6.4 First MARE-1 measurements

In this section the cool-downs devoted to test the entire cryogenic set-up of MARE-1 are presented.

6.4.1 RUN 15

The cryogenic set-up of this run was the same as the RUN 14. In this cool-down the Array equipped with $AgReO_4$ (NASA C30302) was read-out by the MARE-1 electronics and the Array with Sn absorbers (NASA C30204) was read-out by the amplifier at room temperature as usual. For both arrays the thermal link between the array and the ceramic and between the ceramic and the detector holder was increased using Au bonding wires. So far only 40 JFETs are connected with Al bonding wires in the JFETs box. Two different radioactive sources were inserted: ^{57}Co source and ^{55}Fe source with its targets. Until now the targets are made of Al, Si, NaCl and $CaCO_3$. Since the Roman lead shield was still missing in this set-up, the Al holder, just used in RUN 7, kept in place the two Steel rods for the source holder. In this cool-down different measurements were carried out: to monitor the array temperatures and to study the electronic noise of the entire set-up.

Thermal analysis

For both arrays the temperature of an embedded pixel and the temperature of a pixel with absorber were monitored. The still power was set at 5 mW. Setting 70 mW on the JFETs

heater, the resistance of the Pt-100 thermometer, soldered on the JFETs PCB, was about 38 Ω (i.e. around 124 K). The temperature of the array equipped with thin Sn absorbers was measured in two different configurations: the first with the 20 channels of MARE-1 unconnected and the second with the same channels connected. The measured temperatures are listened in table 6.17. Obviously, the only way to measure the temperatures of the array with $AgReO_4$ is to power the MARE-1 electronic channels.

date	**array**	**embedded**	**absorber**	**holder**	**note**
06/10/2011	C30204 -Sn	58 ± 1 mK	58 ± 2 mK	36 ± 1 mK	-
06/13/2011	C30204 -Sn	-	85 ± 2 mK	40 ± 1 mK	20 channels
06/13/2011	C30302 -$AgReO_4$	80 ± 1 mK	90± 1 mK	40 ± 1 mK	20 channels

Table 6.17: RUN 15: the base temperature of an embedded pixel and of a pixel equipped with an absorber for both arrays are listed together with the detector holder temperature.

The direct contact between the array and the JFETs box through the Stainless Steel wires has increased the thermal load on mixing chamber and on the array itself. This increasing has led to an higher temperature of the array even when the 20 channels were still disconnected (i.e. comparison between temperatures measured on 10th of June and the ones measured on 5th of May). Besides, the temperature of the pixel with Sn increased to 40 mK when 20 channels were connected.

Noise analysis

During this run a noise analysis of the MARE-1 electronics was carried out. Firstly, we studied the series noise at varying of the bolometer base temperature. Figure 6.23 shows the spectra noise in frequency domain of pixel 9 when its impedance was 4 MΩ (nse-125), 640 kΩ (nse-126), 360 kΩ (nse-127) and 60 kΩ (nse-128), respectively.

No significant difference was observed between the four noise spectra. Besides the presence of several peaks, the noise was two order of magnitude higher than the expected one and it was characterised by a very strange behaviour.

Subsequently, a noise spectrum in frequency domain was acquired when the system was at room temperature. To eliminate the detector Johnson noise the detectors, whose impedance is 68 kΩ at 300 K, were connected to ground.

Despite the presence of several peaks at low frequencies, the white noise is less than 2 $nV/Hz^{1/2}$ for frequencies above 10 Hz.

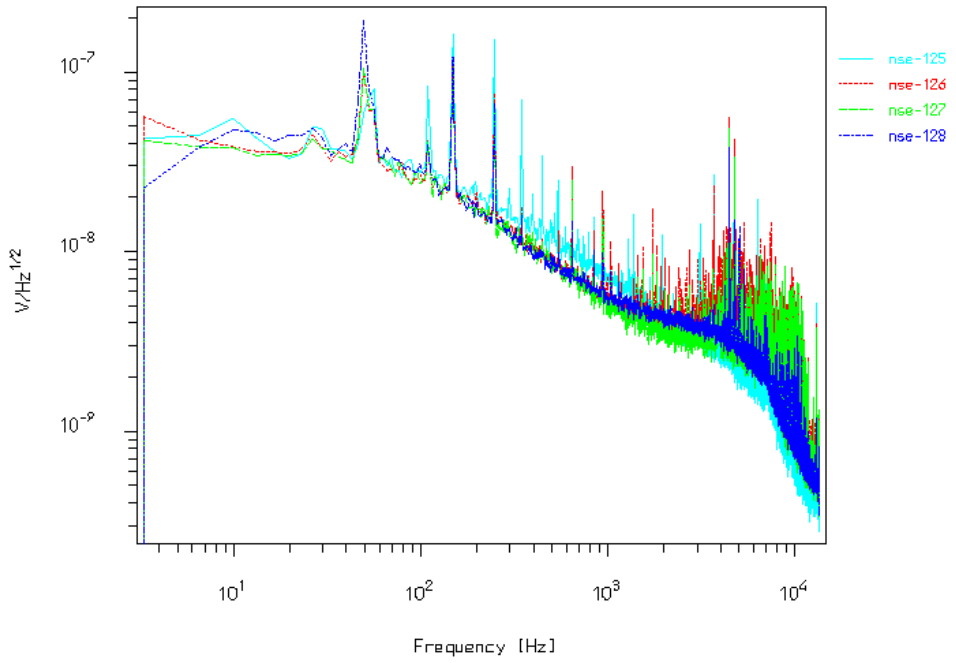

Figure 6.23: Noise spectra in frequency domain acquired when the detector where at different temperatures. The detector impedance was 4 MΩ (nse-125 in cyan), 640 kΩ (nse-126 in red), 360 kΩ (nse-127 in green) and 60 kΩ (nse-128 in blue)

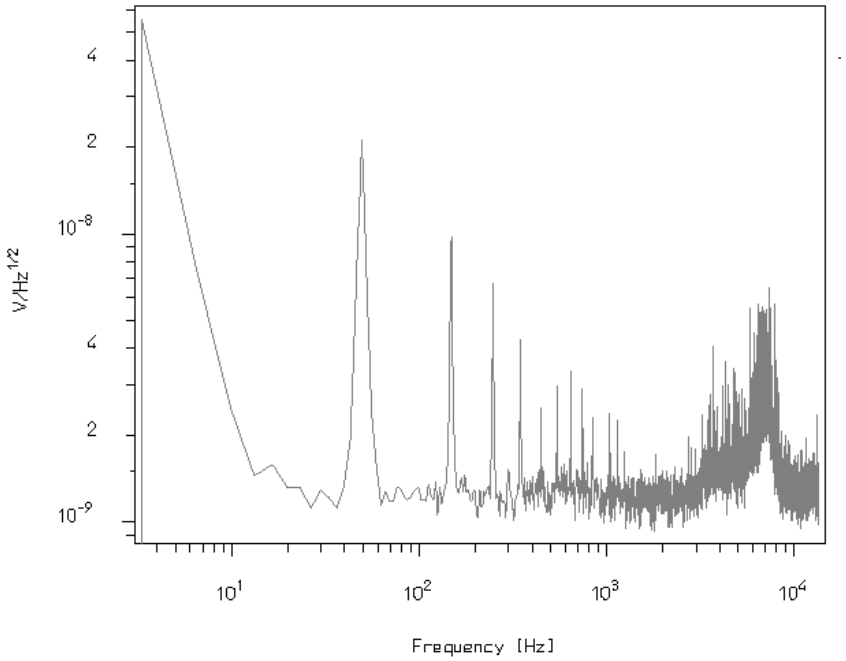

Figure 6.24: A noise spectrum acquired when the system was at room temperature. The detectors were connected to ground.

6.4.2 RUN 16

Since it has been observed an increasing of the thermal load on mixing chamber and on the array itself due to a direct contact between the array and the JFETs box through the Stainless Steel wires, we have decided to connect only few pixels. As a result, we prepared a new test run with only 8 pixels of the C30302 array and only 3 ground signals connected trough the Stainless Steel wires. Therefore only eleven Stainless Steel wires was present in this run and the total power carried by them was around 1.2 μW. Except the number of these wires the cryogenic set-up was the same as the previous run (i.e. RUN 15). The power on the still was set at 5 mW. The JFETs were working at around 135 K. So the detector holder was at 35 mK and the temperatures of the pixels equipped with $AgReO_4$ were around 76 mK.

From the load curve of the pixel 9 (fig. 6.25), one of those equipped with $AgReO_4$ absorber (see table 6.4), it has been extrapolated that the bias necessary to reach the correct working temperature of 85 mK was 12 mV.

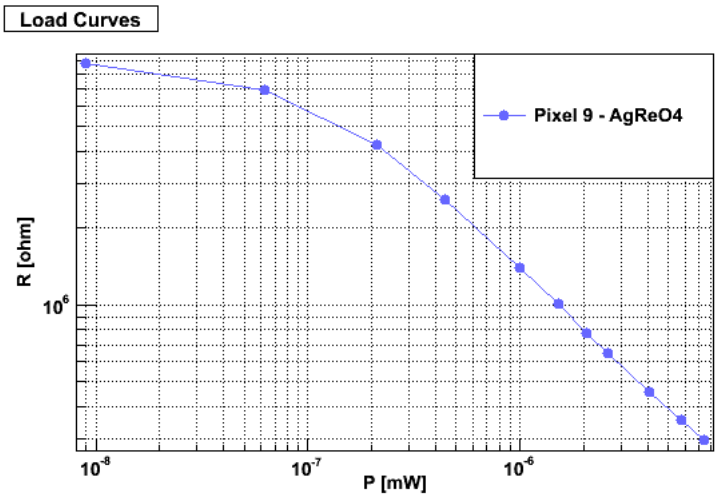

Figure 6.25: RUN 16: Load curve of the pixel 9 of the C30302 array. The pixel is at around 85 mK when the detector bias is set at 12 mV.

Figure 6.26 displays the spectrum of pixel 9 acquired with a National Instrument USB acquisition card. Since ^{57}Co emits γ rays with an energy of 122 and 136 keV, just above the Re K-edge at 71.7 keV, peaks at about 54, 61 and 62 keV due to the escape of K_{β_2}, K_{α_1} and K_{α_2} Re X-rays, respectively, can be observed in the experimental spectrum. Concerning the ^{55}Fe calibration source, the experimental spectrum shows the K_α, K_β lines of Mn and the Al K_α. Except for the Al line, no other peaks due to the presence of different targets as $CaCO_3$ and NaCl are present in the acquired spectrum (figure 6.27). The reason of this lack is under investigation. In spectrum 6.27 near the Mn Kα line it is possible to see a little peak at 5.4 keV which is the Cr Kα peak. In fact, the Chromium is usually presents

in alloy like the Stainless Steel and we would like to point out that the holders for the calibration source are made of this latter material.

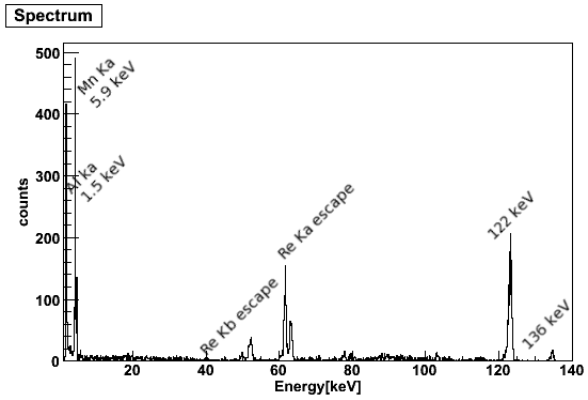

Figure 6.26: RUN 16. The entire spectrum of pixel 9 is shown. One can recognize the γ rays emitted by ^{57}Co at 122 and 136 keV toghether with Re escapes (K_{α_1} = 61.14 keV, K_{α_2} = 59.72 keV e K_{β_1} = 69.3 keV). At low energy the spectrum shows the Al and Mn peaks.

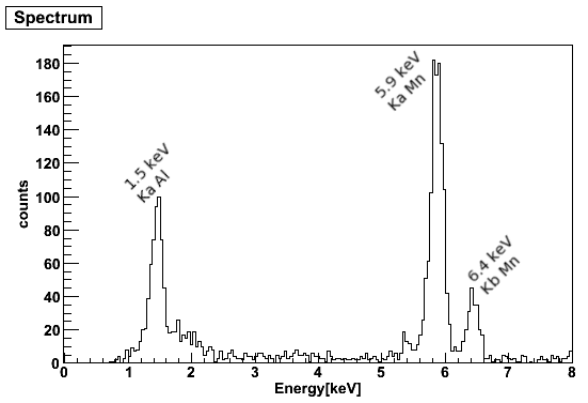

Figure 6.27: RUN 16. A zoom of the spectrum shown in figure 6.26 at low energy with a four times larger bin width. One can see the Al K_α line at 1.5 keV and the Mn K_α and K_β lines at 5.9 keV and 6.4 keV, respectively.

The energy resolution of this detector is 175 eV @ 1.5 keV and 181 eV @ 5.9 keV. The baseline value, evaluated by the noise spectrum, is about 68 eV. The rise time and decay time are 848±38 μs and 16±1 ms, respectively. The ratio ΔV/(6 keV) is 53.9±0.7 μV/(6 keV).

The performances were worse than the ones obtained during the test runs (i.e. RUN 4X, RUN 6X and RUN 8X). A possible cause could be due to an excessive microphonic noise. Therefore, a noise analysis was needed (see following section 6.4.3).

6.4.3 Noise analysis

A noise analysis was performed in all aspects in this run. In all these measurements the cut off frequency of Bessel filter was set at 5 kHz and the JFETs were working at about 135 K.

Firstly, different measurements were done in order to better investigate the noise of the electronics at low frequency. As a consequence, four spectra refer to the pixel 9 were acquired with different time windows. Figure 6.28 displays the noise spectra in frequency domain with a sampling step of 0.012 ms (nse-147 in cyan), 0.037 ms (nse-142 in red), 0.11 ms (nse-143 in green) and 0.37 ms (nse-144 in blue). The spectrum in blue shows how it is possible to solve peaks at low frequencies decreasing the sampling step.

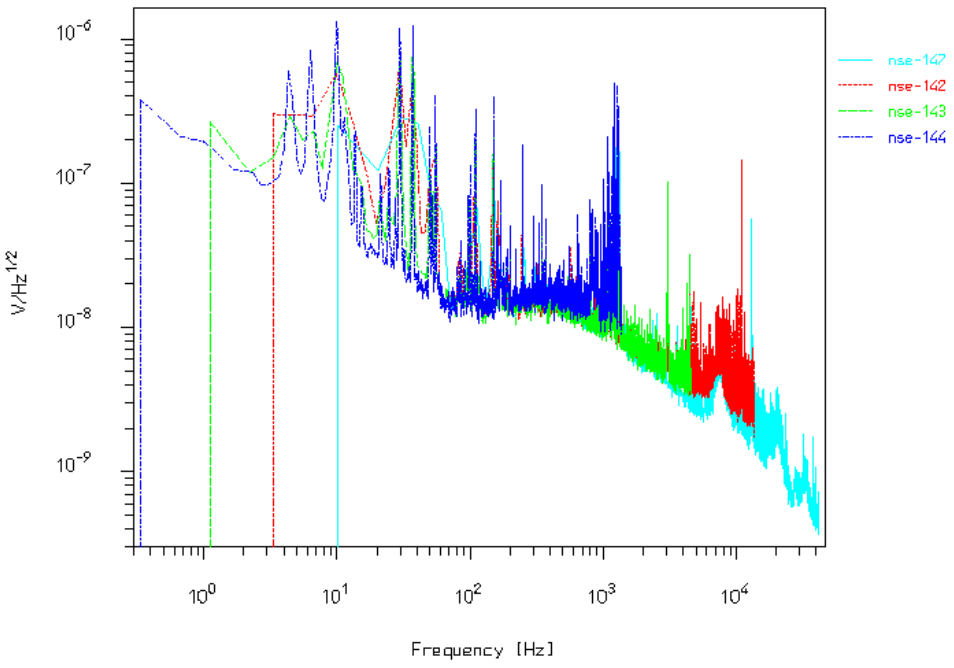

Figure 6.28: Noise spectra in frequency domain acquired with different time windows. The sampling step of nse-147 (cyan), nse-142 (red), nse-143 (green) and nse-144 (blue) are 0.012 ms, 0.037 ms, 0.11 ms and 0.37 ms, respectively.

It was also important to study the additional contribute of noise introduced by the 1 K POT, one basic component of a dilution refrigerator. That is why two noise spectra refer to the same pixel were acquired with the needle valves of 1 K POT opened and closed (see figure 6.29).

The two noise spectra of figure 6.29 do not present great differences.

In the end spectra of different pixel are compared in figure 6.30 and in figure 6.31 in two distinct situations: nse-142 and nse-155 were acquired with the needle valves of 1 K POT opened, while nse-156 and nse-157 were acquired when the needle valves of 1 K POT

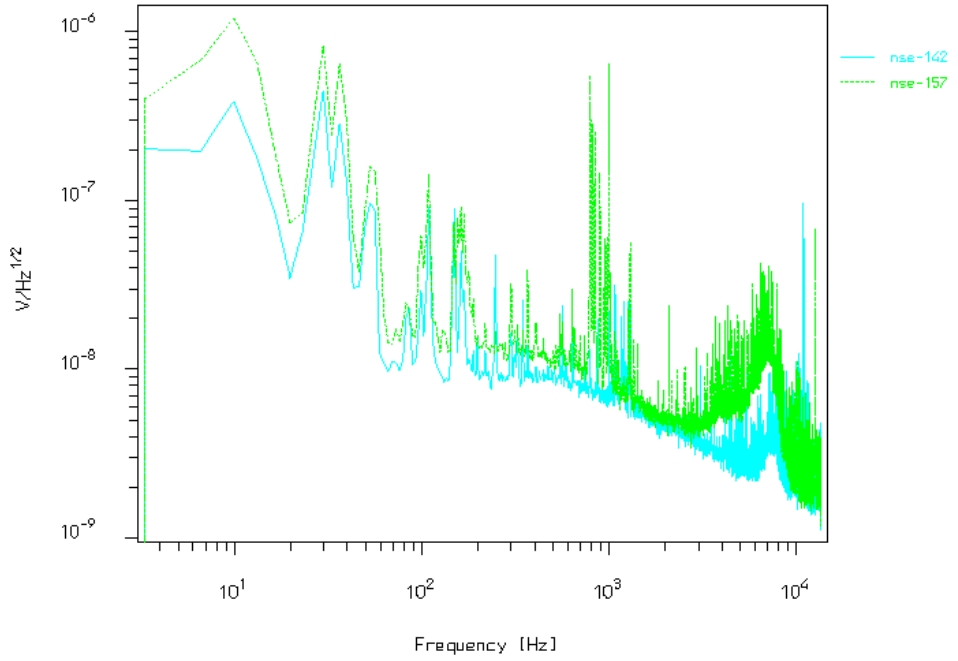

Figure 6.29: Noise spectra in frequency domain of the same pixel acquired with the needle valves of 1 K POT opened (nse-142 in cyan) and closed (nse-157 in green).

were closed.

Figure 6.31 shows how the pixel 6 is nosier than the pixel 9.

In conclusion, the worsening in noise observed in this run respect to the previous one is mainly due to the Stainless Steel wires: reducing the number of wires they were no longer supported and kept taut by the silicon tube placed between them. As a consequence, they introduce an excessive microphic noise which deteriorate the detector performances.

In any case, a noise analysis has been planned to investigate the source of this excessive noise.

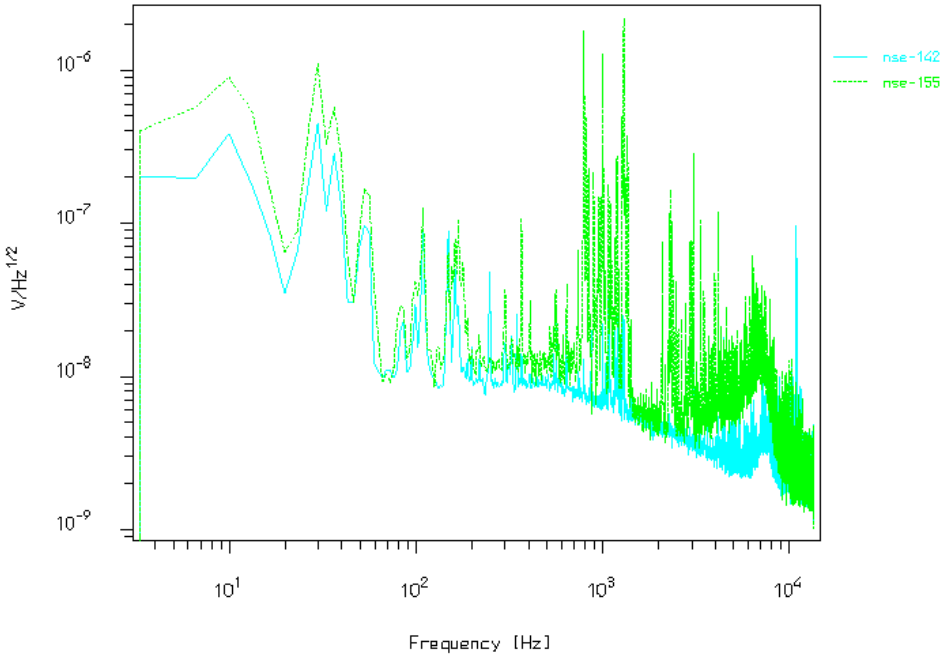

Figure 6.30: Noise spectra in frequency domain of pixel 9 (nse-142 in cyan) and of pixel 5 (nse-155 in green) acquired with the needle valves of 1 K POT opened.

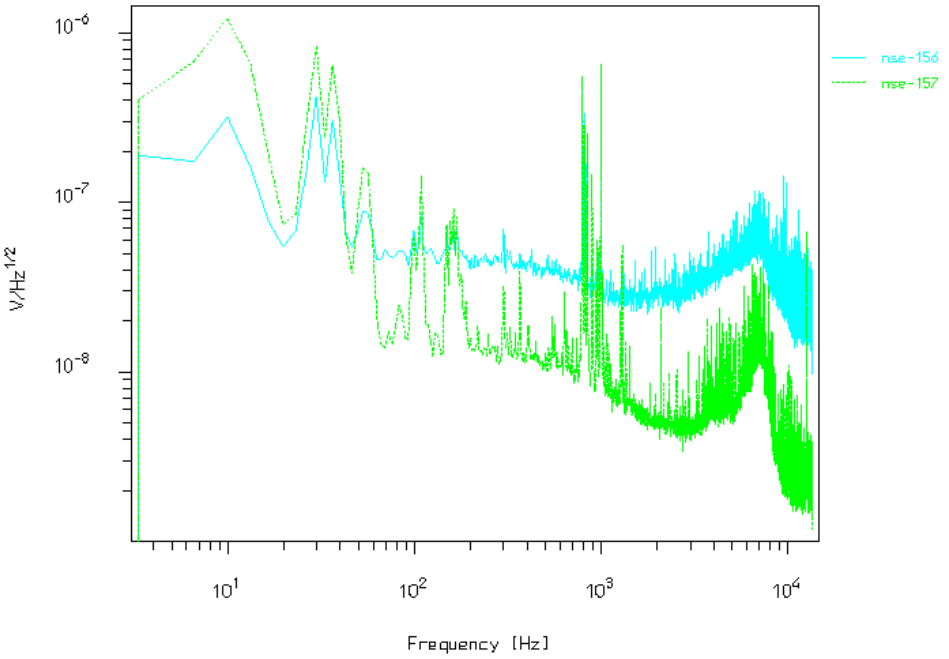

Figure 6.31: Noise spectra in frequency domain of pixel 6 (nse-156 in cyan) and of pixel 9 (nse-157 in green) acquired with the needle valves of 1 K POT closed.

6.4.4 Comparison between RUN 4X, RUN 7 and RUN 16

A comparison between the results obtained in the test run RUN 4X and in the RUN 7 and RUN 16 is presented in table 6.18.

	RUN 4X	**RUN 7**	**RUN 16**
threshold	∼300 eV	∼2 keV	∼800 eV
baseline [eV]	22	370	68
ΔE_{FWHM} [eV] @ 1.5 keV	30±1	-	175±11
ΔE_{FWHM} [eV] @ 6 keV	45±1	427±11	181±7
τ_{rise} [μs]	314±5	543±72	848±38
τ_{decay} [ms]	4.7±0.2	20±1	16±1
ΔV/6 keV [μV/(6 keV)]	95.2±0.4	17.7±0.5	53.9±0.7

Table 6.18: A comparison between the results obtained in the test run (RUN 4X) and in the RUN 7 and RUN 16. The thermal coupling between the absorber and the silicon spacer is made off ST1266, while the thermal coupling between the thermistor and the silicon spacer is made of ST2850.

Thanks to the last changes introduced in RUN 16 the detector performances are better respect to the ones obtained in the RUN 7, when the detector were characterized for the first time using the entire MARE-1 set-up (i.e. the cryogenic set-up and the read-out electronics). In any case, the performances are worse than the ones obtained during the test run 4X. A possible cause could be due to an excessive microphonic noise. Finally, the lengthening of the rise time could be explained with a possible degradation of the thermal coupling between thermistor and absorber due to too many thermal cycles to which the MARE-1 detectors have been subjected.

Chapter 7

Conclusions

My Ph.D work has been focused on the MARE project, an experiment based on rhenium thermal detectors for the direct and calorimetric measurement of the neutrino mass.

The starting point was the estimation of the statistical sensitivity of a such experiment. In section 2.1 I have derived an algorithm to assess the statistical sensitivity for a given experimental configuration and then, for the same experimental configuration, I have estimated the sensitivity on neutrino mass via a Montecarlo method. The results of the analytic approach are then validated through the comparison with the Montecarlo results over a wide range of experimental parameters. The results have shown the importance of the total statistics in order to achieve a sub-eV sensitivity on neutrino mass. Then, the two methods have been applied to estimate the sensitivity on neutrino mass of a present experiment (MARE-1 in Milan) and to investigate the optimal configuration for a future experiment based on Rhenium thermal detectors (MARE-2). For example, the Montecarlo code has shown that a sensitivity on neutrino mass of 3.4 eV at 90% CL could be achieved in 3 years using 288 detectors, each with a mass of 500 μg ($\sim$ 0.3 Hz) and with energy and time resolutions of about 30 eV and 300 μs respectively. This is the Milan MARE-1 configuration. Concerning a plausible experimental configuration capable to achieve a sensitivity of about 0.1 eV on the neutrino mass, the Montecarlo approach has proved that such sensitivity could be expected in 10 years running $3\text{x}10^5$ detectors, each with a mass of 10 mg ($\sim$ 10 Hz) and with energy and time resolutions of about 1 eV and 1 μs respectively.

Then I have extended the application of the Montecarlo approach to analyse the expected sources of systematic uncertainties peculiar to this kind of experiments. In particular, in Section 2.2 I have shown how crucial is for future experiments the understanding of the theoretical ^{187}Re beta decay spectrum and of BEFS.

Finally, in section 3.3 I have evaluated the capability of the MARE experiment to measure the mass of heavy neutrinos from some tens of eV up to 2.5 keV. In section 3.4 the beta spectrum acquired by the Mibeta experiment, the pilot experiment of MARE-1

experiment in Milan, has been analysed in order to give an upper limit at 95% CL on the mixing angle of a heavy neutrino ν_H with a mass in the range 10-1500 eV with a massless neutrino ν_L.

From an experimental standpoint, I have focused primarily on the assembly of the entire cryogenic set-up of MARE-1 in Milan and then on its analysis and improvement. In chapter 5 a detailed description of the baseline of the set-up of the MARE-1 experiment in Milan is reported, while in chapter 6 the activity concerning the assembly and the analysis of the cryogenic set-up are reported together with the improvements added from time to time.

Firstly, the results of runs devoted to test the detector performances and to determinate the best thermal coupling between Si thermistors and $AgReO_4$ absorbers are presented in section 6.1.1. With the test detectors I have obtained an energy resolution of about 30 eV at 2.6 keV and a rise time of around 300 μs. With 72 detectors and such performances, a sensitivity on neutrino mass of 4.7 eV at 90 % C.L. is expected in three years running time. During these cool-downs it was used the electronics of the MIBETA experiment.

Since its first installation the cryogenic set-up of MARE-1 has presented several structural and thermal problems. The first has concerned the electrical connections between the detectors and electronics, while the latter has been related to the insufficient thermal decoupling between the JFETs support and the cold electronic box as well as the insufficient thermalization of the array ceramic board and of the array itself. As a consequence, no signal could be acquired. The R&D work performed to solve these problems has shown that the winning solutions are:

- Al/Si 1% bonding wires to replace the Al microbridges broken during the assembly of RUN 0 (section 6.3.1).
- Stainless Steel wires to replace the Ti microbridges broken during the cool-down of RUN 2 (section 6.3.2)
- Introduction of a Copper braid to better thermalize the JFET box to the 4 K part (RUN 1 in section 6.3.1).
- Au bonding wires to better anchor the array ceramic to the detector holder and the array ceramic to the array itself (section 6.3.5).
- Introduction of a Copper shield at the Mixing Temperature in RUN 13 (section 6.3.5)

Thanks to these improvements added to the baseline MARE-1 set-up and connecting only 8 detectors, the detectors have reached a base temperature such that it was possible to acquire a first spectrum with a threshold below 800 eV. In this condition, an energy resolution of 175 eV at 1.5 keV and of 181 eV at 5.9 keV was obtained, while the rise time

was around 850 μs. It was the first time that a spectrum with this threshold was acquired with the MARE-1 set-up. The worsening observed in the detectors performances with respect to the test runs was due to an excessive microphonics noise. So a detailed noise analysis of the entire read out chain is mandatory and it has been planned to understand where is the source of this excessive noise.

If the Stainless Steel wires are replaced with thinner ones, it will be possible to connect the two arrays. For example, by using Stainless Steel wires of 15.2 μm of diameter, the power carried out by a single wire is a factor 11 lower than the one carried by the Stainless Steel used in MARE-1. In this way it can be hypothesized that a 72 channels measurement will be starting soon.

Bibliography

[1] E. Fermi, *Zeitschrift fur Physik A Hadrons and Nuclei* **88** (1935) 161.

[2] C. L. Cowan, F. Reines et al., *Science* **124** (1956) 103.

[3] F. Reines and C. L. Cowan, *Nature* **178** (1956) 446.

[4] LEP collaborations, *Phys. Lett. B* **276** (1992) 247.

[5] L. M. Lederman, M. Schwartz et al., *Phys. Rev. Let.* **9** (1962) 36.

[6] K. Kodama et al., *Phys. Let. B* **504** (2001) 218.

[7] L.-L. Chau, W.-Y. Keung, *Phys. Rev. Lett.* **53**, (1984) 1802.

[8] A. Sturmia, F. Vissani, hep-ph/0606054v3 (2010).

[9] M. Goeppert-Mayer, *Phys. Rev.* **48** (1935) 512.

[10] E. Komatsu et al. (WMAP Collaboration), *Astrophys. J. Suppl.* **192** (2011) 18. [arXiv:1001.4538 [astro-ph.CO]]

[11] F. DeBernardis et al., *Phys. Rev. D* **80** (2009) 123509.

[12] S. R. Elliott, A. A. Hahn, and M. K. Moe, *Phys. Rev. Let.* **59** (1987) 20202023.

[13] Y. G. Zdesenko, F. A. Danevich, and V. I. Tretyak, *Phys. Lett. B* **456** (2002) 206215.

[14] H. Ejiri, *Progress in Par. and Nucl. Phys.* **48** (2002) 185200.

[15] W. Furry, *Phys. Rev.* **56** (1939) 1184.

[16] H.V. Klapdor-Kleingrothaus et al., *Mod. Phys. Lett. A* **16** (2001) 2049.

[17] F. Avignone III et al., *Rev. Mod. Phys.* **80** (2008) 481.

[18] F. Simkovic et al., *Phys.Rev. C* **77** (2008) 045503.

[19] O. Civitarese et al., *J. Phys: Conference Series* **173** (2009) 012012.

[20] J. Menèndez et al., *Nucl. Phys. A* **818** (2009) 139.

[21] J. Barea et al., *Phys.Rev. C* **79** (2009) 044301.

[22] H. V. Klapdor-Kleingrothaus et al., *Eur. Phys. J. A* **12** (2001) 147.

[23] C. E. Aalseth et al, *Phys. Rev. D* **65** (2002) 092007.

[24] V.B. Brudanin and NEMO Collaboration, *Phys. At. Nucl.* **74** (2011) 312.

[25] E. Andreotti et al., *Astropart. Phys.* **34** (2011) 822.

[26] R. Bernabei et al, *Phys. Lett. B* **546** (2002) 23.

[27] M. Sisti et al, *NIM A* **520** (2004) 125.

[28] V. M. Lobashev, *Nucl. Phys. B (Proc Suppl.)* **91** (2001) 280-286.

[29] Ch. Kraus, *Eur. Phys. J. C* **40** (2005) 447-468.

[30] V. A. Lubimov et al., *Phys. Lett. B* **94** (1980) 266.

[31] H. Kawakami et al., *Phys. Lett. B* **256** (1991) 105.

[32] E. Holzschuh, *Phys. Lett. B* **287** (1992) 381.

[33] R. G. H. Robertson et al., *Phys. Rev. Lett.* **67** (1991) 957.

[34] W. Stoeffl et al., *Phys. Rev. Lett.* **75** (1995) 3237.

[35] A. Picard et al, *Nucl. Instr. Meth.B* **63** (1992) 345.

[36] C.L. Bennett et al, *Phys. Lett. B* **107** (1981) 19.

[37] A. De Rujula, *Nucl. Phys. B* **188** (1981) 414.

[38] A. De Rujula and M. Lusignoli, *Phys. Lett. B* **118** (1982) 72.

[39] G. Audi and A. H. Wapstra, *Nucl. Phys. A* **595** (1995) 409.

[40] C.W. Reich et al, *Nucl. Data Sh.* **111** (2010).

[41] M. Ribeiro-Gomes et al, *AIP Conf. Proc.* **1185** (2009)

[42] J.-P. Porst, LTD14 proceedings.

[43] M. Faverzani, LTD14 proceedings.

[44] , R. Divornicky and F. Simkovich, *AIP Conf. Proc.* **1180** (2009) 125.

[45] F. Gatti et al, *Nucl. Phys. B* **91** (2001) 293.

[46] R. Dvornickỳ et al, *Phys. Rev. C* **83**, (2011) 045502.

[47] S.E. Koonin et al,*Nature* **354** (1991).

[48] P.A. Lee et al, *Phys. Rev. B* **11** (1995)2795.

[49] F. Gatti et al, *Nature* **397** (1999) 137.

[50] C. Arnabold et al, *Phys. Rev. Lett.* **96** (2006) 042503.

[51] F. Zwicky, *Helv. Phys. Acta* **6** (1933) 124.

[52] F. Zwicky, *Phys. Rev.* **51** (1937) 290.

[53] J. H. Oort, *ApJ* **91** (1940) 273.

[54] S. Dodelson, L. M. Widrow, *Phys. Rev. Lett.* **72** (1994) 17.

[55] X. Shi, G. M. Fuller, *Phys. Rev. Lett.* **82** (1999) 2832.

[56] K. Abazajian, G. M. Fuller, M. Patel, *Phys. Rev. D64* (2001) 023501.

[57] K. Abazajian, G. M. Fuller, *Phys. Rev. D* **66** (2002)023526.

[58] G. M. Fuller et. al., *Phys.Rev. D* **68** (2003) 103002.

[59] K. Abazajian, *Phys. Rev. D* **73** (2006) 063506.

[60] M. Shaposhnikov, I. Tkachev, *Phys. Lett. B* **639** (2006) 414.

[61] A. Kusenko, arXiv:hep-ph/0703116; arXiv:astro-ph/0608096.

[62] T. Asaka, M. Shaposhnikov, A. Kusenko, *Phys.Lett. B* **638** (2006) 401.

[63] P. L. Biermann, A. Kusenko, *Phys. Rev. Lett.* **96** (2006) 091301.

[64] J. R. Bond, A. S. Szalay, *Astrophys. J.* **274** (1983) 443.

[65] J R Bond, A S Szalay, M S Turner, *Phys. Rev. Lett.* **48** (1982) 1636.

[66] C. J. Hogan, J. J. Dalcanton, *Phys. Rev. D* **62** (2000) 063511.

[67] J. J. Dalcanton, C. J. Hogan, *Astrophys. J.* **561** (2001) 35.

[68] H.J. de Vega and N. S nchez, *Mon. Not. R. Astron. Soc.* **404** (2010) 885.

[69] D. Boyanovsky, H.J. de Vega and N. Sanchez, *Phys Rev D* **77** (2008) 043518.

[70] H.J. de Vega and N. Sanchez, *Int. J. Mod. Phys. A* **26** (2011) 1057.

[71] H.J. de Vega, P. Salucci and N. Sanchez, ph/1004.1908.

[72] A. D. Dolgov, *Phys. Rept.* **370** (2002) 333.

[73] F. Munyaneza, P. L. Biermann, *Astron. and Astrophys.* **458** (2006).

[74] A. Kusenko, *Phys. Rept.* **481** (2009) 1.

[75] F. D. Steffen, *Eur. Phys. J. C* **59** (2009) 557.

[76] G. Mention et al, *Phys. Rev. D* **83** (2011) 20.

[77] P. Anselmann et al. (GALLEX Collaboration), *Phys.Lett. B* **357** (1995) 237.

[78] J. Abdurashitov et al., *Phys.Rev. C* **73** (2006) 045805.

[79] A. Aguilar-Arevalo et al. (The MiniBooNE Collaboration), *Phys.Rev.Lett.* **98** (2007) 231801.

[80] L. Oberauer, *Nucl. Phys. B* **70**, (1999) 155.

[81] D.E. Groom et al, *Eur. Phys. J.C* **15** (2000) 364.

[82] K.H. Hiddeman, H. Daniel and O. Schwentker, *J. Phys. D* **21** (1995) 639.

[83] J. J. Sympson, *Phys. Rev. D* **24** (1981) 2971.

[84] G.E. Berman, M. L. Pitt, F.P. Calaprice and M. M. Lowry, *Phys. Rev. C* **48** (1993).

[85] J.L. Mortara et al, *Phys. Rev. Lett.* **70** (1993) 394.

[86] T. Ohshime et al, *Phys. Rev. D* **47** (1993) 4840.

[87] H. Kawakami et al, *Phys. Rev. B* **287** (1992) 45.

[88] K. Schreckenbach, G. Colvin and F. von Feilitzsch, *Phys. Lett. B* **129** (1983) 45.

[89] J. Deutsch, M. Lebru, R. Priels, *Nucl. Phys A* **518** (1990) 149.

[90] M. Galeazzi et al, *Phys. Rev. Lett* **86** (2001) 1978.

[91] G.J.Feldamn and R.D. Cousins, Phys. Rev. D **57**, (1998) 3873.

[92] K. Nakamura et al. (Particle Data Group), *J. Phys. G* **37**, (2010) 075021.

[93] G. F. Knoll, *Radiation Detection and Measurment*, Whyle and Son, Third edition (2000).

[94] P.W. Anderson, *Physics Review* **109** (1958) 1492.

[95] N.F. Mott & W.D. Twose, *Advances in Physics* **10** (1961) 107.

[96] A. Alessandrello et al., *Physics Review Letters* **82** (1999) 3.

[97] R. Bernabei et al., *Physics Letters B* **424** (1998) 185.

[98] D. MacCammon, http://arxiv.org/abs/physics/0503086v1 (2005).

[99] B.I. Shklovskii and A.L. Efros, in *Electronic Properties of Doped Semiconductors*, Springer-Verlag (1984).

[100] J. Zhang et al., *Physics Review B* **48** (1993) 2312.

[101] J. Zhang et al., *Physics Review B* **57** (1998) 4950.

[102] I.S. Shlimak, in *Hopping and Related Phenomenas eds.* H. Fritzsche & M. Pollak, World Scientific, Singapore (1990) p. 49.

[103] P. Dai, Y. Zhang and M.P. Saracchik,*Physics Review Letters* **69** (1992) 1804.

[104] E.F. Haller, N.P.Palaio, M. Rodder, W.L. Hansen and E. Kreysa, in *Neutron Transmutation Doping of Semiconductors Materials*, ed. R. D. Larrabee, Plenum New York (1984), p. 21.

[105] http://crio.mib.infn.it/wig/Cuorepage/proposal-040119.pdf .

[106] P.M. Downey et al, *Nuclear Instruments and Methods* **A520** (2004) 439.

[107] S. H. Moseley, J.C. Mather and D. MacCammon,*Journal Application Physics 56* (1984) 1257.

[108] J. Zhang et al, *Physics Review B (*57) (1998) 4472.

[109] T.W. Kenny et al,*Physics Review B (*39) (1989) 8476.

[110] S.M. Grannan, A.E. Lange, E.E. Haller and J.W. Beeman,*Physics Review B (*45) (1992) 4516.

[111] G. Pignatel and S. Sanguinetti, *Journal of Physics: Condesed Matter 2* (1993) 10011.

[112] N. Whang et al, *Phys. Rev. B 41* (1990) 3761.

[113] E. Auberg et al, *J. Low. Temp. Phys.* **93** (1993) 289.

[114] D. Liu et al, *AIP Conf. Proc.* **605** (2002) 87.

[115] R.N. Bhatt, P.A. Lee, *Phys. Rev. Lett.* **48** (1982) 344.

[116] L.D. Landau and E.M. Lifshitz, *Statistical Physics*, Pergamon, 1980.

[117] C. Arnaboldi et al, *Phys. Rev. Lett.* **91** (2003).

[118] M. Galeazzi et al, *Phys. Rev. C* **63** (2001).

[119] F. Gatti et al, *J. Low Temp. Phys.* **151** (2008) 603.

[120] A. Nucciotti, arXiv:1012.2290v1

[121] F. S. Porter et al, *Nucl. Inst. and Meth. in Phys. Res. A* **559**, (2006) 436.

[122] R.P. Brekosky et al, *Nucl. Inst. and Meth. in Phys. Res. A* **520** (2004) 439.

[123] C. Gotti, LTD14 proceeding.

[124] G. Pessina et al, *AIP Conference Proceedings* **1185** (2010).

[125] F. Pobell. *Matter and methods at low temperature* Springer (1991).

[126] G. Ventura, *Nucl. Phys. B* **78**, (1999) 573.

[127] D. Schaeffer et al., *J. Low Temp. Phys.* **151**, (2008) 623.

[128] V. Martelli and G. Ventura, *AIP Conf. Proc.* **1185**, (2009) 685.

[129] E. Ferri, Graudated Thesis, *Misura diretta della massa del neutrino con una matrice di rivelatori termici*, Milano (2007).

[130] Pobell, *Matter and methods at low temperature*, 1991.

[131] E. Ferri, Rendiconti Scuola di Fisica E. Fermi. edited by F. Ferroni e F. Vissani, CLXX course , VA170-25.

[132] A.Alessandrello et al, *IEEE Transaction in Nuclear Science*, **47**, (2000) 1851.

[133] D.V.Camin e G.Pessina, *IEEE Transaction in Nuclear Science* **47**, (2000) 2039.

[134] M.Malatesta, M.Perego e G.Pessina, *Nuclear Instruments and Methods in Physics Research* **444A**, (2000) 140.

[135] C. Arnaboldi et al, *Phys. Rev. Lett* **91**, (2003) 161802.

[136] L. Risegari et al, *Cryogenics* 44 (2004) 875.